Experimental and Numerical Investigation of a Parallel Jet MILD Combustion Burner System in a Laboratory-scale Furnace

by

George Gabriel Szegö

A thesis submitted in fulfilment of
the requirements for the degree of
Doctor of Philosophy

School of Mechanical Engineering
Faculty of Engineering, Mathematical and Computer Science

THE UNIVERSITY
OF ADELAIDE
AUSTRALIA
SUB CRUCE LUMEN

March 2010 (Approved in July 2010)

Chapter 1 Introduction

1.1 Combustion and the Environment

The ability to control fire is regarded as one of mankind's greatest achievements. Since humans gained control of fire, possibly as early as 790,000 years ago [78], combustion has been part of our daily lives directly or indirectly. In today's industrialised society, a variety of applications, from food preparation to transport, manufacturing and electricity generation, rely on the energy produced by combustion.

Figure 1.1 provides historical data on the world's energy consumption sorted by source, and an outlook for the near-future. Global energy demands are projected to increase by 57% between the year 2004 and 2030 driven by population and economic growth [56]. Noteworthy that the power generation sector alone contributes to 47% of this increase [145]. Fossil fuels − mainly oil, natural gas and coal − supply about 87% of the energy used worldwide, and are expected to continue dominating over the projection period. Despite the steady annual growth of 1.9%, renewable energy sources, such as hydro, solar, wind, geothermal, waste incineration, and biomass, are only predicted to represent about 8% of the world's total energy in 2030. Nuclear energy will likely remain with the lowest share of the total marketed energy. This global scenario highlights the importance of combustion in the years to come.

Rising concentrations of atmospheric greenhouse gases, which are widely accepted to lead to global warming [93], have intensified discussions about the combustion of fossil and alternative fuels. Combustion-generated CO_2 emissions account for about 80% of anthropogenic greenhouse gases [144], so their mitigation is vital, and an aim of policies around the world. In recognition of the

1

NOTE:
This figure is included on page 2
of the print copy of the thesis held in
the University of Adelaide Library.

Figure 1.1: World commercial energy consumption by source [56].

observed climate change, the international community adopted the Kyoto protocol in 1997, which came into force in 2005. These stringent regulations together with industrial demands have motivated engineers and scientists to pursue more efficient and environmentally friendly combustion systems.

1.2 Energy Efficiency and MILD Combustion

In a world increasingly concerned with the environment, changes to the way energy is produced and used are indispensable for a sustainable future. A report compiled for the British Government, named the Stern Review [174], calculates the economic impact of climate change to be as large as 20% of the global gross domestic product (GDP) each year if no action is taken to minimise greenhouse gas emissions.

Improving energy efficiency is often the most cost-effective way to reduce CO_2 emissions [92]. The global mitigation potential associated with the adoption of more efficient practices in the industrial sector is estimated by the Australian Bureau of Agricultural and Resource Economics (ABARE) to be about 1.54 Gt CO_2-

e/yr (gigatonnes of carbon dioxide equivalent per year) over the period from 2001 to 2050 [128]. According to ABARE, energy efficiency is expected to contribute approximately 58% to the global abatement across all sectors of the economy in 2050 [82].

A wide range of low- or zero-carbon emission technologies are already available [149]. Examples include combined heat and power (CHP) plants, hybrid vehicles with regenerative breaking systems, and biofuels, just to name a few. A range of other concepts like carbon capture and storage (CCS) [14] and energy harvesting [50] are being developed as longer-term solutions. Worth mentioning that these technological advances were only possible because of the crucial input of fundamental research.

Clearly, substantial reductions in fuel consumption and associated carbon footprint are possible. However, in processes involving combustion, the abatement of pollutants often comes at the price of efficiency losses. One credible candidate to simultaneously meet thermal efficiency needs and pollutant emission restrictions is Moderate or Intense Low-oxygen Dilution (MILD) combustion.

The MILD combustion regime operates on the principles of heat and flue gas recirculation. The recirculation of hot combustion products decreases the oxygen concentration locally and increases the temperature of the reactants. This slows the reactions and leads to a distributed reaction zone. Distributing the heat release to a larger volume results in a nearly uniform temperature distribution with reduced peak temperatures. As a consequence, the net radiation flux can be enhanced by as much as 30% [182], and emissions of some pollutants are lower than from conventional flames, in which the heat release is confined to a flame front. Because of this almost homogeneous distribution of heat, "hot spots" are eliminated and product quality can be improved in some applications.

In pratice, MILD combustion should not be confused with other emission control strategies proven to work in conventional systems, such as staged combustion and flue or exhaust gas recirculation (FGR or EGR). Although there are similarities, the MILD regime operates with dilution rates well beyond the critical limits for conventional flame stabilisation. Therefore, in order to sustain the oxidation reactions in such diluted conditions, MILD burners are often coupled with air preheating. Heat exchangers are used to recover energy from the exhaust gases, before they are discharged into the atmosphere, and preheat the incoming com-

bustion air. This not only increases the temperature of the mixture of gases and helps to maintain the combustion reactions, but also improves thermal efficiency.

The unique features of MILD combustion make it an attractive technology to bridge the gap between the supposedly contradictory requirements of energy savings and low pollutant emissions. A better understanding of this innovative combustion technology will enable its implementation in a variety of combustion devices.

1.3 Thesis Outline

Most development efforts in the area of MILD combustion have primarily been driven by the industry. Despite considerable industrial success, important fundamental aspects of MILD combustion remain unknown. This project seeks to characterise the MILD combustion regime in a furnace environment burning gaseous fuels through both experiments and numerical modelling.

It is often a difficult, time-consuming and costly process to conduct detailed and accurate measurements in industrial scale furnaces. Therefore, a laboratory-scale furnace was carefully designed and built to enable a variety of parameters to be easily varied, and allow optical access for laser-based measurements. Unlike in most previous investigations in this area, a relatively simple combustion chamber and burner arrangement is used. The furnace operates with a parallel jet burner system in which the reactants and exhaust ports are all mounted on the same walls. The burner system was configured to achieve high dilution of the incoming reactants and sustain MILD combustion for a wide range of operating conditions. A variable area heat exchanger is used to control the heat load. In-furnace temperatures are measured with thermocouples and global emissions with a gas analyser, while velocities are measured using laser Doppler anemometry (LDA).

This furnace/burner configuration provides well defined boundary conditions that lends itself to mathematical modelling. A computational fluid dynamics (CFD) model is developed to assess the suitability of current combustion models to predict the distributed and diluted reactions of MILD combustion. It is also used to better understand the thermal and flow fields and the parameters that influence their structure. The experimental data set is used to validate the model.

This thesis is a contribution towards the fundamental understanding of MILD combustion. The following chapter provides a technical background relevant to this thesis. An overview of pollutant emissions with emphasis on nitrogen oxides (NO_x) is presented, followed by a review of the current knowledge of MILD combustion. The LDA used in this study to determine the velocity field is also described.

In Chapter 3 the equipment and the methodology used in all measurements carried out in this research are outlined.

In Chapter 4 the numerical modelling approach is examined. A brief description of the model parameters is presented, and the boundary and initial conditions are specified.

In Chapter 5 the operating conditions for this study is summarised and the results of global temperature and emission measurements is presented. Here the effects of various parameters on performance and stability are examined and discussed.

In Chapter 6 the extensive experimental data set is used to investigate the scaling of NO_x emissions with global parameters.

In Chapter 7 the numerical modelling results are examined. The predictions are compared to thermal and flow field measurements for a nonreacting isothermal case and a reference case with and without air preheat.

In Chapter 8 the joint experimental and modelling results presented earlier in Chapters 5 to 7 are used to discuss the importance of air preheating on the establishment of the MILD regime as well as the effects of complex recirculating flow patterns on the stability characteristics of the burner system. The implications of the findings on pollutant formation and/or destruction and on the mathematical modelling of MILD combustion are also considered. The major findings are related to full-scale industrial applications.

Finally, in Chapter 9 conclusions are drawn and recommendations for future work in this field are made.

Chapter 2 Background

2.1 Pollutant Emissions

The downside of any process that involves combustion is atmospheric pollution. Because of the adverse effects of atmospheric pollution on human health and the environment, most industrialised countries have developed strict standards that regulate emissions from combustion sources. Hence the control of pollutant emissions is a major factor in the design of modern combustion systems. The primary pollutants produced by combustion are nitrogen oxides, carbon monoxide, unburned hydrocarbons, sulphur oxides and particulate matter [184]. Of these five pollutants, only the first three are discussed in this section due to their relevance to MILD combustion systems operating in enclosed systems with gaseous fuels. To better understand the mitigation strategies for these pollutants, the basic formation and/or destruction mechanisms are briefly described.

2.1.1 Nitrogen oxides (NO$_x$)

The main nitrogen oxides found in the atmosphere are nitric oxide (NO), nitrogen dioxide (NO$_2$), commonly grouped together as NO$_x$, and nitrous oxide (N$_2$O). Since the major direct sources of N$_2$O are natural rather than combustion [20], it is not grouped in the NO$_x$ definition. In general, fractions higher than 90% of the NO$_x$ present in the exhaust of a combustion system are in the form of NO [20]. Most of the NO is produced around the reaction zone, with oxidation to NO$_2$ eventually occurring away from the combustion region in a post-flame process [164].

Due to their role in combustion and their impact on the environment, the

chemical kinetics of NO has been the subject of several studies [33, 47, 135]. Since the fuels used in this project do not contain bound nitrogen in their molecular structure, NO is formed via three main pathways or mechanisms: the thermal-NO or Zel'dovich mechanism, the prompt-NO or Fenimore mechanism and the N_2O-intermediate mechanism.

Thermal-NO or Zel'dovich mechanism

The thermal-NO or extended Zel'dovich mechanism [206] consists of three reactions;

$$O + N_2 \rightleftharpoons NO + N \tag{2.1}$$

$$N + O_2 \rightleftharpoons NO + O \tag{2.2}$$

$$N + OH \rightleftharpoons NO + H \tag{2.3}$$

The first two reactions are chain propagating steps. As a result even small concentrations of O atoms can produce significant amounts of NO. The rate-limiting reaction of the NO formation process is equation 2.1 because of its high activation energy, about $E_a \approx 319 \, kJ/mol$. The thermal-NO route has thus a strong temperature dependence. The Zel'dovich mechanism generally dominates at temperatures above 1500°C independent of fuel type [19].

Prompt-NO or Fenimore mechanism

During the combustion of hydrocarbon fuels, NO formation rates can exceed those attributable to the oxidation of nitrogen molecules by the thermal-NO mechanism (equation 2.1), especially in fuel rich-conditions [135]. Fenimore [58] found that NO was rapidly produced in the reaction zone of laminar premixed ethylene-air flames, and termed this apparently instantaneous formation as prompt-NO.

The actual prompt-NO mechanism involves a complex sequence of reactions that are coupled to the fuel chemistry. A number of hydrocarbon radicals resulting from the fragmentation of the fuel, for example CH, CH_2, C, C_2, and C_2H, have been suggested as the sources of prompt-NO [135]. In the overall scheme, these intermediate species react with molecular nitrogen to form amines or cyano compounds that subsequently react to form NO. Nonetheless, the major
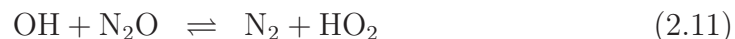
contribution occurs via the following key reaction steps;

$$\mathrm{CH + N_2} \;\rightleftharpoons\; \mathrm{HCN + N} \tag{2.4}$$

$$\mathrm{CH_2 + N_2} \;\rightleftharpoons\; \mathrm{HCN + NH} \tag{2.5}$$
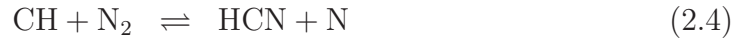
The relatively low activation energy of equation 2.4, about $E_a \approx 57 \, \mathrm{kJ/mol}$, indicates a weaker dependence on temperature [33]. Some prompt-NO formation also occurs due to superequilibrium O and OH concentrations that can accelerate equations 2.1 to 2.3 [20].

N_2O-intermediate mechanism

The N_2O-intermediate mechanism involves the production of N_2O as an intermediate and the subsequent conversion to NO as follows [116, 121, 173];

$$\mathrm{N_2 + O + M} \;\rightleftharpoons\; \mathrm{N_2O + M} \tag{2.6}$$

$$\mathrm{O + N_2O} \;\rightleftharpoons\; \mathrm{NO + NO} \tag{2.7}$$

$$\mathrm{O + N_2O} \;\rightleftharpoons\; \mathrm{N_2 + O_2} \tag{2.8}$$

$$\mathrm{H + N_2O} \;\rightleftharpoons\; \mathrm{NO + NH} \tag{2.9}$$

$$\mathrm{H + N_2O} \;\rightleftharpoons\; \mathrm{N_2 + OH} \tag{2.10}$$

$$\mathrm{OH + N_2O} \;\rightleftharpoons\; \mathrm{N_2 + HO_2} \tag{2.11}$$

Since equation 2.6 is a third-body recombination reaction, it is favoured at elevated pressures. Equations 2.6 to 2.8 include oxygen atoms, which favours the mechanism in fuel-lean conditions. The relative importance of the nitrous oxide intermediate pathway increases in conditions where the total NO formation rate is relatively low [20]. For this reason, the N_2O-intermediate mechanism is particularly important in combustion devices that operate at low temperatures to prevent thermal-NO formation, such as gas turbines [33] and fluidised bed combustors [116].

Control strategies

Nitrogen oxides are one of the most regulated air pollutants due to their contribution to photochemical smog formation, acid rain, and ozone depletion in the stratosphere. Figure 2.1 shows various strategies employed to reduce NO_x emissions from gas-fired industrial equipment. These devices include boilers, process heaters, furnaces, and ovens usually operating with natural gas. NO_x emission levels associated with such equipment predominantly result from thermal-NO formation. Hence most NO_x abatement techniques aim to lower peak temperatures and keep the residence time and oxygen concentrations low in high temperature zones [199]. It is worth mentioning that the strategies to limit prompt-NO and N_2O-intermediate formation tend to be different. This makes the task of reducing NO formation very difficult and sensitive to the characteristics of a specific application.

NOTE:
This figure is included on page 9
of the print copy of the thesis held in
the University of Adelaide Library.

Figure 2.1: NO_x control technologies for gas-fired industrial combustion equipment (adapted from Ref. [17]).

The NO_x control technologies are divided in Figure 2.1 into combustion modifications and post-combustion techniques. Within the broad classification of combustion modifications there are several abatement approaches. Although MILD combustion resembles some of these methods, it would lie in its own separate subcategory under the combustion modifications branch. The difference arises from the operating principles of MILD combustion, as will be discussed in §2.2.

Whether directly or indirectly, the different methods shown in Figure 2.1 ulti-

mately reduce peak temperatures. Injecting water or steam into the combustion chamber increases the heat capacity of the gas mixture, thereby lowering peak temperatures. Recirculating flue gases (FGR), which can be achieved internally or externally, has the same dilution effect on temperature as water injection. Reducing the levels of air preheat lowers combustion temperatures, but has the undesirable outcome of reducing thermal efficiencies.

Another way of controlling NO_x emissions is to operate close to stoichiometric conditions by reducing the overall excess air. However, only modest reductions are possible without increasing the levels of carbon monoxide and unburned hydrocarbon emissions [184]. In the staged combustion approach the oxygen availability is controlled locally by dividing the combustion process into sequential stages. Air staging creates a fuel-rich condition in the primary combustion zone, with staged introduction of additional air. Fuel staging, on the other hand, operates in a fuel-lean condition upstream, while the remaining fuel is injected downstream. In the case of combustion devices operating with multiple burners, for example tangentially-fired boilers [48], staging is established by modifying the operation of each burner. One common burner management pratice is called overfire air, which involves adjusting all upstream burners to operate rich and supply secondary air through downstream ports.

A variation of the staging concept is reburning. The reburning technique consists of three stages: a fuel-lean primary combustion zone followed by a fuel-rich reburning zone, where additional fuel is injected, and a final stage to provide air for complete fuel burnout [132]. The reburning mechanism is based on reactions of NO with hydrocarbon radicals, leading to the formation of hydrogen cyanide much like in the prompt-NO mechanism, $CH_i + NO \rightarrow HCN +$ products. Eventually, a subsequent conversion to molecular nitrogen is accomplished ($NO \rightarrow HCN \rightarrow N_2$) [135].

Burners based on premixed combustion, which include lean premixed gas turbine combustors [33], porous radiant burners [3] and fibre-matrix burners [17], can also decrease NO_x emissions significantly through reduction in temperature. Another burner technology that provides reduced NO_x emissions is the precessing jet (PJ) burner [138]. An alternative method for reducing NO formation that is becoming more common is oxygen-enhanced combustion [12]. This technique relies on reducing the nitrogen concentrations in the combustion system by adding

oxygen to the combustion air. Theoretically, operating with pure O_2 eliminates all nitrogen from the process, and thus NO formation. However, in practice, some nitrogen is present in the fuel and it is hard to prevent air infiltration into the combustion chamber [155].

When combustion modifications alone do not meet the strict NO_x emission restrictions, after-treatment of the exhaust products of a combustor is required. The most common post-combustion processes for NO removal are selective non-catalytic reduction (SNCR) and selective catalytic reduction (SCR). Essentially, SNCR involves injection of a nitrogen-containing compound, such as ammonia (NH_3), urea ($CO(NH_2)_2$) or cyanuric acid ($(HCNO)_3$) into the exhaust stream to chemically reduce NO to N_2 [184]. To achieve a similar kind of conversion, the SCR method uses a catalyst in combination with ammonia injection. The NO removal efficiency for both SNCR and SCR mainly depends on the temperature range of operation [135].

Most of the control strategies mentioned above have been successfully implemented in industrial-scale devices to comply with NO_x emission regulations [20]. Low-NO_x burners are most effective when a combination of techniques is employed, for example burners designed for furnaces and boilers typically combine FGR and staging methods [90], while automotive engines use FGR together with SCR [89].

Scaling of NO_x emissions

The development of scaling laws for NO_x emissions is useful, not only for understanding which geometrical or operational parameters control pollutants formation, but also for assessing the relative importance of the alternative NO_x formation mechanisms. The scaling of NO_x has been comprehensively investigated in unconfined nonpremixed turbulent jet flames [183], and also given considerable attention in enclosed furnace environments with conventional combustion systems [6, 90, 165, 191]. These studies have found a strong correlation of normalised NO_x emission indices with fuel jet exit Froude number, and of NO_x formation rates with global temperatures and residence times.
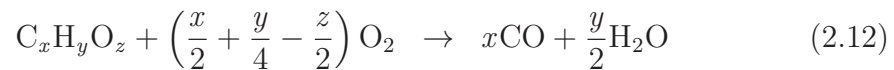
Little is known about the scaling relations of NO_x emissions in complex recirculating flows with local oxygen concentrations as low as 3% at moderate

temperature ranges ($800°\text{C} < T < 1400°\text{C}$), typically found in the MILD regime. Sobiesiak et al. [171] reported an empirical correlation for NO_x emissions as a function of excess air, air preheat temperature, burner turndown ratio and exhaust gas temperature from the exhaust gas analysis of a semi-industrial research furnace. Although relatively few experimental data points were available, a power-law type expression was used to show that the exhaust temperature term had the strongest effect on NO_x emissions. Other researchers [140, 142] attempted to relate NO_x emission trends to burner parameters, such as fuel injection angle and fuel to air velocity ratios.

To date, the results of NO_x scaling relations have not been previously reported for MILD combustion conditions, neither in enclosed nor in open flame systems. To bridge this gap, the current work aims to build an experimental data base to examine the scaling of NO_x emissions from a laboratory-scale MILD combustion furnace.

2.1.2 Carbon monoxide (CO)

The complete combustion of hydrocarbon fuels produces carbon dioxide and water. Carbon monoxide emissions are a result of incomplete combustion. Despite the complexity of hydrocarbon combustion chemistry, the oxidation process can be simplistically described by a two-step global mechanism [196];

$$\text{C}_x\text{H}_y\text{O}_z + \left(\frac{x}{2} + \frac{y}{4} - \frac{z}{2}\right)\text{O}_2 \quad \rightarrow \quad x\text{CO} + \frac{y}{2}\text{H}_2\text{O} \tag{2.12}$$

$$\text{CO} + \frac{1}{2}\text{O}_2 \quad \rightarrow \quad \text{CO}_2 \tag{2.13}$$

In equation 2.12 fuel is partially oxidised to carbon monoxide, and then in equation 2.13 the final conversion of carbon monoxide to carbon dioxide occurs.

Although this global reaction approach may yield sufficient information in some problems, it does not provide any insight into the intermediate steps that affect CO formation. It is well known that small amounts of hydrogen-containing species will substantially increase the oxidation rates of CO [72]. Under the "wet" conditions found in most practical systems, i.e., water is the predominant hydrogen-containing compound, the following four elementary reactions describe the CO oxidation process [184];

$$
\begin{aligned}
\text{CO} + \text{O}_2 &\rightarrow \text{CO}_2 + \text{O} & (2.14) \\
\text{O} + \text{H}_2\text{O} &\rightarrow \text{OH} + \text{OH} & (2.15) \\
\text{CO} + \text{OH} &\rightarrow \text{CO}_2 + \text{H} & (2.16) \\
\text{H} + \text{O}_2 &\rightarrow \text{OH} + \text{O} & (2.17)
\end{aligned}
$$

The chain initiating step (equation 2.14) is slow at typical combustion temperatures. The actual rate-controlling reaction is equation 2.16, which is also a chain propagating step. The hydrogen atom produced in equation 2.16 react with oxygen in equation 2.17. In turn, the products of equation 2.17 serve as reactants in equations 2.15 and 2.16. A more comprehensive CO oxidation mechanism that include other hydrogen-containing species can be found in Yetter et al. [204]. However, equation 2.16 still remains the most important reaction step.

The overall scheme shows that CO is produced whenever there is insufficient oxygen or insufficient time at high temperatures to complete the reactions. For this reason, NO_x control strategies that lower peak flame temperatures can increase CO emission. Generally, fuel-rich conditions need to be avoided to maintain low levels of CO in the exhaust [19].

Other mechanisms that may form CO in substantial quantities at temperatures above $1800°C$ include the dissociation of molecular CO_2 [184], which is basically the reverse of equation 2.13. The diluted conditions of MILD combustion, in which high levels of CO_2 exist, has the potential to reduce the rate of conversion of CO into CO_2. In nonpremixed combustion systems, CO emissions are also strongly related to soot formation [185].

Carbon monoxide is a toxic gas that can have severe health effects on individuals exposed to high concentrations. The health hazards are associated with the formation of carboxyhemoglobin in the blood, which inhibits cell and tissue oxygenation [158]. To avoid accidental poisoning in the presence of indoor combustion sources, a recommended safety procedure is to install CO detectors.

2.1.3 Unburned hydrocarbon (UHC)

Much like CO emissions, unburned hydrocarbons are a product of incomplete combustion. As such, excessively lean (air-to-fuel ratio higher than 20:1 [80]), or excessively rich regions are potential sources of UHC emissions. In conditions with high levels of excess air or in pockets of gas with low oxygen concentrations, partial oxidation and fuel pyrolysis are favoured.

Unburned hydrocarbons may also result from quenching processes, such as cold streams and the presence of cold surfaces [184]. Quenching does not necessarily contribute to UHC emissions, because the oxidation process depends on subsequent diffusion and convection of the unburned gas mixture. Burner configuration and mixing patterns inside the combustion chamber are therefore crucial parameters to ensure the completion of the oxidation process. The temperature range, uniform heat flux and excess air levels encountered in MILD combustion ensures very low, or even not detectable, levels of UHC at the exhaust[26, 194]

The formation mechanisms of unburned hydrocarbons are intrinsically coupled to the detailed chemical kinetics of a particular type of fuel [196]. Despite the complex chemistry, emissions of UHC generally follow those of CO in many practical combustion devices [89]. In reality, only a small fraction of UHC emissions are residual fuel molecules [184]. Other undesirable partially burned compounds, such as aldehydes and ketones, are found in the exhaust gases. These oxygen-containing intermediate species contribute to photochemical smog and cause respiratory and eye irritations.

2.2 MILD Combustion

2.2.1 Definition / Terminology

One of the major challenges of combustion science and technology is to develop combustion systems that lead to reduced pollutant emissions and increase thermal efficiency. An effective method to enhance efficiency and diminish fuel consumption is to preheat the reactants, or combustion air alone, using heat recovery methods [98]. Preheating using heat recycled from the exhaust gases without mixing the reactants and product streams has been initially called excess enthalpy

combustion [84], and later more generically, heat-recirculating combustion [195]. The amount of recycled heat controls the temperature rise throughout the combustion process. This concept was mainly developed to allow the combustion of low calorific value fuels. The major drawback of heat-recirculating combustion is the increased NO_x emissions due to the increase in temperatures.

It is now well-established that significant reductions in NO_x are possible, even with high levels of air preheat, when the reactants are diluted with products in a high temperature environment [199]. Over the years, several terms have been used to describe combustion systems that operate under these principles. Some names focused on the burner design, i.e. Fuel Direct Injection (FDI) [127, 137] or Low-NO_x Injection (LNI) [140], while others described the combustion process, i.e. flameless oxidation (FLOX® burners) [199], High Temperature Air Combustion (HiTAC) [182], or highly preheated lean combustion [24]. For simplicity, the term adopted in this thesis is Moderate or Intense Low-oxygen Dilution (MILD) combustion [43]. The various terminology found in the literature demonstrates that there is no rigorous definition for this combustion technology.

One attempt to rigorously define MILD combustion has been made by Cavaliere and de Joannon [23, 24]. They classified the combustion process according to the operating temperature of a well-stirred reactor (WSR) at atmospheric pressure for a stoichiometric mixture of methane, oxygen, and nitrogen with a residence time of one second (Figure 2.2). The selfignition or autoignition temperature (T_{si} or T_{ai}) is the lowest temperature at which the mixture spontaneously ignites and burns. Processes that involve high temperature reactants were grouped under the term High temperature Combustion Technology (HiCOT). MILD combustion was defined as a particular case of HiCOT, in which the inlet temperature of the reactants is higher than the selfignition temperature of the mixture ($T_{in} > T_{si}$), while the maximum temperature increase during combustion in relation to the inlet temperature is lower than the selfignition temperature ($\Delta T < T_{si}$). This qualitative definition relies on the assumption that MILD combustion is solely controlled by chemical kinetics and cannot be sustained without external preheating of the reactants.

A quantitative definition for MILD combustion based on temperature fluctuations in the flow field was suggested by Kumar et al. [105]. They found that the normalised temperature variation is around 50% for a conventional propane
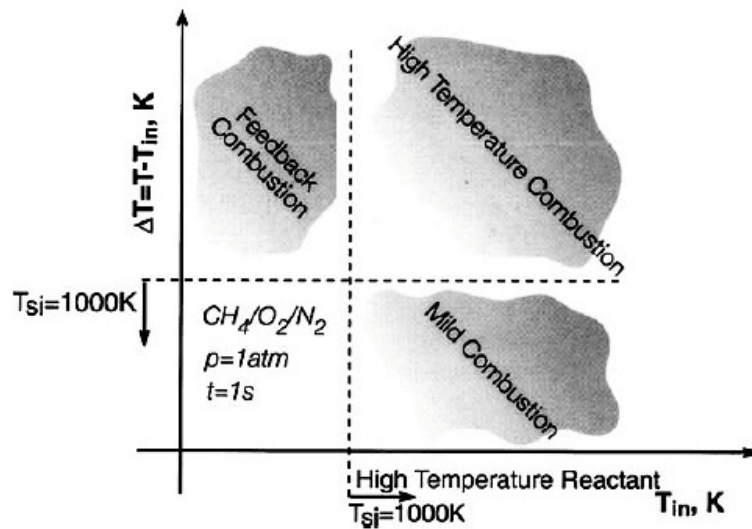
Figure 2.2: Definition of MILD combustion based on the theory of well-stirred reactor (WSR) [23].

jet diffusion flame, compared to only 15% for MILD conditions. Although this alternative criterion showed that the temperature fluctuations for MILD conditions are notably lower than for the conventional flame, a general definition was not established.

2.2.2 Fundamentals and characteristics

The principle of operation for MILD combustion is based on the combination of heat and flue gas recirculation [98, 182]. The two fundamental conditions that must be satisfied to establish the MILD regime are schematically shown in Figure 2.3. The recirculation of hot combustion products need to ensure high dilution levels, while increasing the temperature of the reactants. The temperature prior to combustion must exceed the autoignition temperature of the mixture. For this reason, air preheating is commonly applied with the desirable consequence of increasing the thermal efficiency. The highly diluted environment, with local oxygen concentrations typically between $2-5\%$ [193], compensates for the increase in flame temperature and subsequent NO_x production introduced by preheating.

The low oxygen concentration results in a distributed reaction zone. By ex-

NOTE:
This figure is included on page 17
of the print copy of the thesis held in
the University of Adelaide Library.
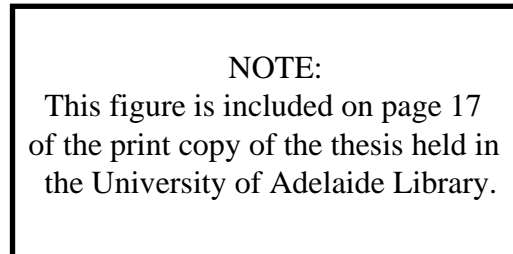
Figure 2.3: MILD combustion operating principles (adapted from Ref. [198]).

panding the heat release to a larger volume, a nearly uniform temperature distribution with reduced peak temperatures is produced, thereby largely suppressing thermal-NO formation [199]. The distributed thermal field associated with MILD combustion is also characterised by minor temperature fluctuations [26]. Hence the combustion noise due to pressure fluctuations is greatly reduced [105, 199]. Because the extent of the reaction zone increases, the heat transfer exchange area is larger and hence the radiative heat transfer is improved. This implies that the heat release rate per unit volume tends to be lower in MILD conditions than in conventional flames [85].

Perhaps the most remarkable characteristic of MILD combustion is the visual appearance. In contrast to conventional flames, the oxidation proceeds with no visible flame when the furnace operates under ideal MILD conditions. The luminosity in typical methane flames depends on the electronic excitation of radicals such as CH and C_2, both of which are formed at relatively high temperatures, and are avoided in the MILD regime [45]. Barely visible nonsooting bluish coloured flames are typically reported for these reduced oxygen conditions for methane [136], and faint bluish-green coloured flames for propane or LPG [66, 81]. The colour of the flame not only depends on fuel type, but also on the diluent and intermediate species [167]. Because of the low emission in the visible spectrum, furnaces have been described as operating in flameless [199] or colourless [94] mode.

2.2.3 Regimes of operation

One aspect that is particularly important in combustion studies is flame stabilisation. In contrast to conventional flame systems, which are commonly fitted with flameholders to avoid liftoff and blowout, MILD burners promote flame extinction close to the fuel jet exit by delaying the mixing between the reactants or increasing the strain rate [194]. Although flame anchoring is not required, temperatures above autoignition and high dilution rates are necessary conditions for stable operation (see Figure 2.3). The mechanism to satisfy these conditions and control the oxidation process is mainly associated with effective mixing. However, this mechanism is not trivial and little published information is available on the stability of the MILD regime.

Earlier studies focused fundamentally on the flammability limits of combustible gases [205] and the effects of vitiation on flame extinction [126]. Mastorakos et al. [126] studied the extinction limits of turbulent counterflow diffusion flames with the unburned reactants diluted with hot combustion products. They found that an increase in the dilution of the oxidant stream required an increase in temperature to maintain stability. In fact, they reported that for a 2% decrease in the oxygen mole fraction, a 100 K increase in temperature was required to avoid extinction. Nevertheless, when the vitiated air temperature reached levels above 1700 K autoignition was observed, and the flame did not extinguish with high strain rates. Although this study was not meant to emulate MILD combustion, the findings demonstrate an improvement in flame stability under similar conditions.

More recently, Riechelmann et al. [160] studied the effect of air preheating on the extinction limits of methane-air diffusion flames with either the fuel or the air streams diluted with Ar, N_2 or CO_2. They measured the critical strain rate for air temperatures up to 1500 K, and found a significant influence of the diluent type and degree of dilution on extinction through an activation energy asymptotic analysis. Their results complement the work of Mastorakos et al. [126] in that the effects of temperature and dilution were isolated.

Figure 2.4 shows the stability limits for different combustion regimes as a function of exhaust gas recirculation and characteristic furnace temperatures. Wünning and Wünning [199] defined exhaust gas recirculation as the ratio between
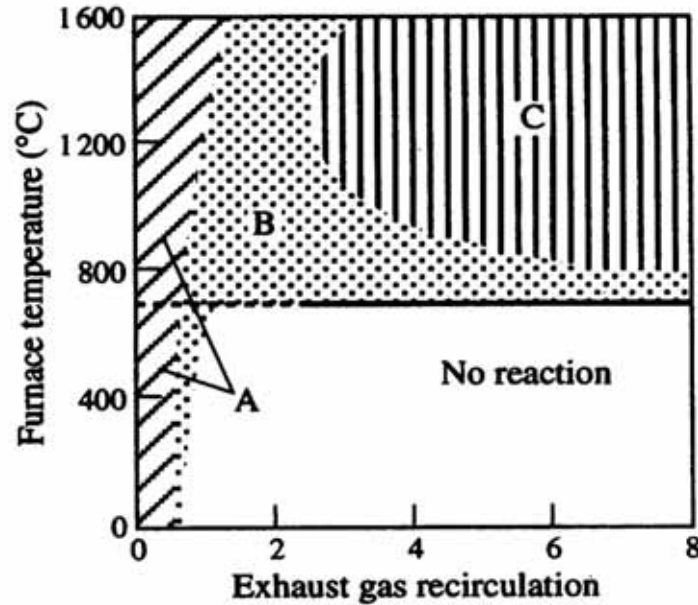
Figure 2.4: Stability diagram for conventional and MILD combustion [199].

the mass flow rate of exhaust gases internally recirculated into the air and fuel streams before reaction and the total mass flow rate injected into the furnace. Mathematically, the recirculation rate parameter, K_V, shown in the abscissa of Figure 2.4 is expressed as

$$K_V = \frac{\dot{m}_e}{\dot{m}_f + \dot{m}_a} \,, \tag{2.18}$$

where $\dot{m}$ represents mass flow rate, and the subscripts refer to recirculated exhaust gases (e), fuel (f), and air (a). This definition is equivalent to the one used for conventional burners operating with external flue gas recirculation (FGR) [11]. The horizontal line at $\approx 700°C$ represents the autoignition limit for methane.

By relating furnace temperature to K_V, three combustion regimes are identified in Figure 2.4. Region A is characterized by stable conventional flames with $K_V \leq 0.3$ over the entire temperature range, region B by an unstable transitional regime either independent of K_V for temperatures close to autoignition, or with approximately $0.5 \leq K_V \leq 3$ for temperatures above $\approx 800°C$, and region C by the MILD or flameless oxidation regime with $K_V > 3$ for temperatures higher than $\approx 800°C$. The diagram highlights the fact that the MILD regime operates

with dilution rates well beyond the critical limits for conventional flame stabili-sation due to the widening of the flammability limits. No further description of the instabilities present in Region B has been provided.

In an attempt to characterize the transition from unstable (Region B) to stable (Region C) MILD regime, Cavigiolo et al. [25] conducted experiments on a small-scale enclosed cylindrical burner for methane and ethane. A numerical model was used to estimate the flow field for a nonreacting isothermal condition, and adapt the definition of K_V to include both internal and external recirculation, as well as secondary streams. Experimentally, K_V was varied either by changing the air preheat level or by diluting the primary air jet with nitrogen. Based on an average chamber temperature and emission measurements, they found that the transition occurred for methane at $K_V \approx 4$ around 800°C and for ethane at $K_V \approx 3.5$ around 600°C. The same burner configuration and methodology has been used by Effuggi et al. [55] to extend the measurements to other fuel mixtures. They found that the transitional value for natural gas (90% CH_4 + 10% C_2H_6 by volume) was slightly shifted towards $K_V \approx 3.5$ in comparison to pure methane, and for biogas (50% CH_4 + 50% N_2 by volume) decreased to $K_V \approx 3.2$, both of which at around the same 800°C. The critical value was identified at the peak of CO emission that corresponded to a decrease in the temperature gradient between the top and the bottom of the chamber. However, the visual appearance of the flame during the unstable regime was not discussed and no explanation for the sudden increase in CO emissions was given in either study.

Another way of classifying the regime of operation of a combustion system is to examine the interaction of combustion and turbulence. A key dimensionless parameter in turbulent nonpremixed combustion is the Damköhler number, Da, which represents the ratio of a characteristic mixing time to a characteristic chemical time ($Da = \tau_{mix}/\tau_{chem}$). When $Da \gg 1$, the chemical reaction rate is much faster than the mixing rate, thus describing a fast-chemistry regime. If the turbulence field is fast enough not to be influenced by the chemistry, then $Da \ll 1$, and conditions approach that of a well-stirred, or perfectly stirred, reactor. This kind of classification is sometimes called *scale separation* and greatly simplifies the modelling of turbulent combustion [152]. On the other hand, the characteristic time scales depend on the application and can be difficult to quantify, because of the multiple reaction steps involved in the combustion of hydrocarbons, and the

variation of the levels of turbulence in space.

Most practical combustion devices operate at variable heat loads and therefore a wide range of Damköhler numbers is found in the flow domain, leading to extinction and ignition events [18]. Oberlack et al. [143] analytically studied the stochastic Damköhler number fluctuations for well-stirred reactor conditions. Their steady-state temperature solution showed a monotonic function of the Damköhler number and a monomodal probability density function (PDF) behaviour for the MILD regime. It means that the ignition and extinction branches seen on the well-known S-shaped curve coincide in MILD conditions [143, 152]. Theoretically, this implies that the instabilities related to the transition from unburned to burned states are completely suppressed. In practice, despite the fact that the temperature increase in the reaction zone are small in MILD combustion [154], the assumption of WSR conditions is unlikely to always hold. It is particularly important to note that a bimodal distribution of the PDF of temperature has been observed in a recuperative furnace [37] and in a lean quasi-premixed heated and diluted impinging jet configuration [4].

Awosope et al. [9, 10] classified three MILD combustion applications in a Borghi diagram [18]: a laboratory-scale furnace operating with a FLOX® burner [199], a prototype gas turbine afterburner [111], and a semi-industrial-scale Hi-TAC furnace [194]. The Borghi diagram defines combustion regimes in terms of velocity and length scale ratios [152]. The main nonpremixed turbulent combustion regimes are the thickened flame (or well-stirred regime), the perturbed flamelet and the flamelet regimes [109]. In their modelling study, Awosope et al. [9, 10] found that combustion started at the thickened flame regime for all three cases at the burner exit, but then developed into the perturbed flamelet regime in the FLOX® furnace and afterburner, and the flamelet regime in the HiTAC furnace. This implies that turbulence disturbed the flamelet structures as the reaction zone propagated for the first two cases, and had a much smaller influence in the third case. Together with an analysis of the scalar dissipation rate, which is an indicator of the influence of mixing on the chemistry, they concluded that local extinction was important when high momentum jets are used to induce internal flue gas recirculation for strong dilution.

In summary, stability in the MILD combustion context depends on the mixing of fresh reactants and burned gases, and is not attributed to liftoff and blowout.

However, the question of which parameter controls the stability of MILD combustion still remains under intense debate and is one of the key issues driving the current research.

2.2.4 Burner and furnace technology

The advantages offered by MILD combustion made this newly developed technology very attractive to the industry. MILD combustion burners have been successfully implemented in industrial processes including steel, ceramic and glass furnaces [59, 108, 133]. The benefits in relation to conventional flames include enhanced thermal efficiency, a homogeneous thermal field and reduced NO_x emissions. Fuel savings of up to 60% can be achieved by combining combustion air temperatures of around 1300°C with $2-3\%$ O_2 levels at the exhaust, while maintaining both CO and NO_x emissions very low [194].

In practical applications, waste heat recovery systems are used to preheat the combustion air. Recuperative and regenerative heat exchangers transfer the sensible heat from the exhaust gases to the combustion air, thereby improving energy utilisation [26]. The difference between these two devices is that recuperators transfer energy from a steady flow of flue gas, while regenerators store the energy from the flue gas into a medium, which is later used to heat the air [184].

An example of a MILD combustion furnace equipped with a regenerative system is shown in Figure 2.5. The system consists of two regenerative burners with ceramic honeycomb-type heat exchangers. During one cycle, air flows through the hot ceramic honeycomb, which preheats the incoming air, while the flue gases heat the other regenerator in the stand-by burner at the opposite side. In the next cycle, after the temperature of the honeycomb in the working burner decreases, the flow direction is reversed. This alternating flow process is controlled by a 4-way switch valve. The high-frequency operation, typically $30-60$s, ensures highly preheated air temperatures (>1000°C) with variations less than 50K during each cycle [98]. Due to the high temperatures, autoignition conditions are achieved and hence the combustion reactions will always be sustained inside the furnace. The preheating of combustible mixtures has been proposed as an effective method for burning low calorific value fuels [98, 136].

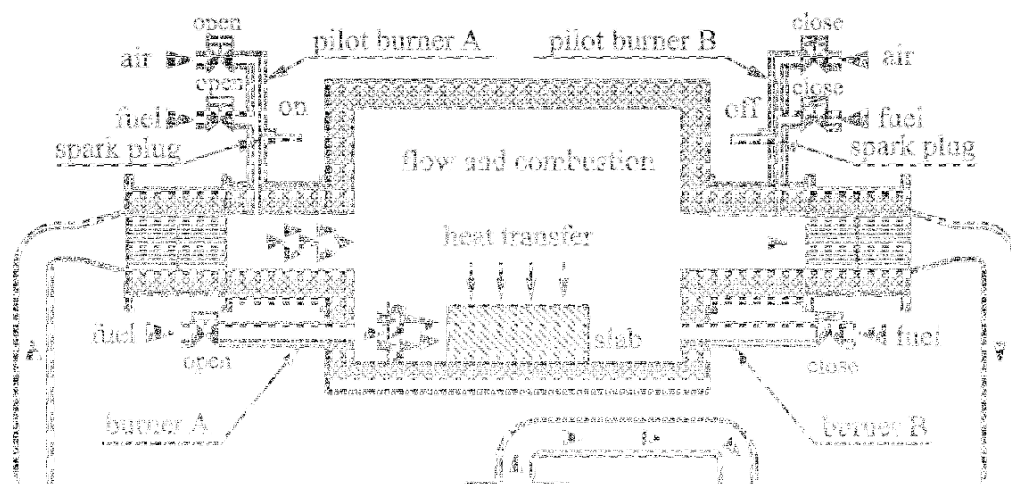A review of the latest advances in MILD combustion technology identifies sev-

Figure 2.5: Schematic layout of an industrial MILD combustion furnace operated with alternating flow regenerators [98].

eral different burner configurations (see Figure 2.6). Essentially, MILD burners can be separated into two groups with distinct design concepts, according to the nozzle arrangement. The first group comprises burners with a central fuel jet surrounded by a number of air jets. The most prominent in this category is the FLOX® burner developed by WS Wärmeprozesstechnik GmbH in Germany [198, 199]. This burner is fitted with either a built-in regenerator (REGEMAT®) or recuperator (REKUMAT®) that uses about 80% of the flow of exhaust gas for air preheating. The operation of the FLOX® burner is based on high momentum jets that induce internal recirculation of flue gases. Such internal recirculation allows adequate heating and dilution of the air and fuel streams, which leads to a uniform temperature distribution. Also relying on high momentum jets, Linde AG developed the flameless oxy-fuel REBOX®-W burner. It has characteristics similar to the FLOX® burner, except that pure oxygen is used instead of air to produce a higher heat flux throughout the furnace with even lower NO_x emissions [104].

The second group consists of burners with several fuel jets arranged around a central air jet. The FDI concept [127, 137] introduced by Tokyo Gas Company is central to the burners in this category. The idea is to delay the mixing between the reactants by positioning the fuel and air nozzles apart from each other. As a result, the air and/or fuel streams are diluted by hot combustion products before they mix and react. Following this concept, Nippon Furnace Kogyo (NFK) investigated the number of fuel nozzles and the separation distance between the fuel and air inlets to develop the NFK-HRS burner series. It is worth mentioning that the Scaling 400 project [191, 192, 194] performed in the International Flame Research Foundation (IFRF) in the early nineties featured a burner configuration that resembled a FDI system.

An equivalent strategy to prevent the mixing of fuel and air close to the burner exit is to inject the fuel at an angle [142, 178]. This method was exploited by the North American Manufacturing Company to develop the Low NO_x Injection (LNI) burners in the United States [140]. Similarly, the Canadian Gas Research Institute (CGRI) introduced a multiple jet burner in which alternated fuel and air ports are uniformly arranged in a ring pattern at an angle in relation to the burner axis [171]. Since both fuel and oxidant are discretely injected into the furnace, the concept behind the CGRI burner was renamed Fuel/Oxidant Direct

Injection (FODI) [171]. The aforementioned burner developments focused on minimising NO_x emissions of a particular burner design, and led to the patenting [15, 22, 198] and commercialisation of the technology.

These studies highlight the importance of the mixing characteristics in achieving MILD combustion. In general, high momentum jets and a relatively large distance between the air and fuel nozzles are used to enhance the entrainment of combustion products into the fuel and air streams before the mixture reacts. Fuel dilution can also help establish MILD combustion with a shift in stoichiometry in the vicinity of the fuel jet exit [37]. This alternative approach may be less practical, but has the potential to eliminate the need for high momentum jets.

One of the effects of dilution under MILD combustion conditions is that the extent of the reaction zone increases considerably. In fact, simple flame length calculations predict a flame two and a half times longer for a 5% O_2 concentrations in the oxidant stream [182]. This in turn leads to a more uniform heat flux with lower peak temperatures, potentially eliminating "hot spots" and improving product quality. Despite the lower temperatures, the total heat transfer rate is 30% higher than in conventional flames because of the larger reaction volume [182]. The more effective heat dissipation allowed a desirable 25% decrease in equipment size for a number of industrial applications [182].

The lack of an actual flame in MILD combustion is another indication that the heat transfer characteristics are different from conventional systems. While the luminosity is low, radiation is still emitted from major species such as CO_2 and H_2O. The gaseous radiation, together with convection, transfer energy to the adjoining wall surfaces, which in turn has the effect of significantly increasing radiant heat flux from the walls. For this reason, furnaces operating in the MILD regime have been described as "glowing" [193]. From a safety perspective, the absence of a flame front restricts the use of ionisation current or UV detectors, and requires flame supervision systems that rely on temperature monitoring [199].

As previously shown in this section, most of the work in this area has been driven by industrial requirements. Although a range of burner configurations has been developed, each employs the principle of heat and flue gas recirculation. While successful, existing MILD burners typically have a narrow operating range [23] and are heavily dependent on heat recovery systems for air preheat [98]. The relatively low modulation ratio and dependence on high levels of air preheating
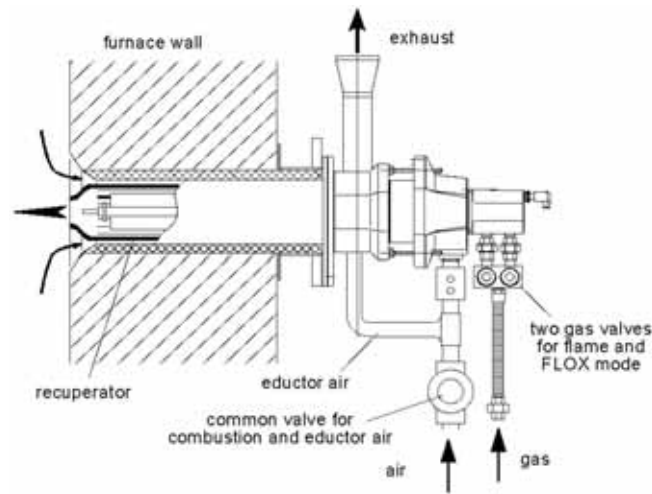
(a) FLOX® burner [199]

NOTE:
This figure is included on page 26
of the print copy of the thesis held in
the University of Adelaide Library.

(b) LNI burner [140]
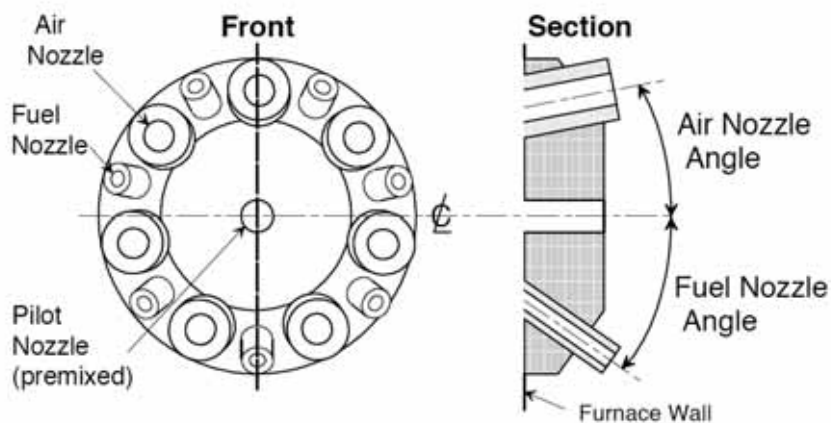
(c) CGRI burner [61]

Figure 2.6: Different burner configurations used in MILD combustion.

has thus far restricted the application of MILD burners to heat treatment processes. Despite considerable efforts to extend the MILD combustion technology to other heat and power systems, such as boilers [103, 207], radiant tubes [134], and gas turbines [110, 111], critical operational parameters still require further investigation.

The laboratory-scale furnace carefully designed and built for this project will enable a variety of parameters to be easily and independently varied in a well controlled environment. This will then avoid much of the limitations of existing research and permit a detailed analysis of fundamental aspects for a wide range of operating conditions.

2.2.5 Mathematical modelling

Although the concepts of MILD combustion have been studied extensively, mathematical modelling of this regime has received relatively little attention. A comprehensive chronological summary of MILD combustion modelling studies is presented in Appendix A. The review shows that several burner configurations with a wide range of nominal capacities for different gaseous fuels were numerically investigated, mainly in complex furnace (e.g. [32, 61, 107, 146]) or gas turbine [10, 54] environments, and to a lesser extent in simple enclosed [202] and open [28] jet flames. It is seen that only a few experimental data sets with in-furnace or in-flame measurements are available for validation. One of the purposes of the current research is to generate valuable data for model validation.

At first glance the MILD regime seems relatively straightforward to model as it does not feature the high-density gradients, typically present in conventional flames. However, the low oxygen concentration slows the chemical reactions and increases the influence of the turbulence-chemistry interaction. For this reason some combustion models developed for conventional nonpremixed reactive flow systems might not be applicable to MILD conditions.

Several combustion models have been proposed to predict the distributed and diluted reactions of MILD combustion. Among the conserved scalar approach are the mixture fraction (ξ) with an assumed β-shape PDF (e.g. [28, 146]), laminar flamelet (e.g. [32, 37]) and conditional moment closure [100] (CMC) models. The volumetric reaction methods include the eddy dissipation (ED) (e.g. [117]) model

and the eddy dissipation concept (EDC) (e.g. [28]). The more sophisticated transport probability density function (TPDF) approach has also been used (e.g. [31]). The numerical simulations have been primarily performed with commercial CFD packages within the Reynolds averaged Navier-Stokes (RANS) context, with the exception of the recent work by Duwig et al. [54], which involved the large-eddy simulation (LES) method.

It is difficult to identify the most suitable approach for modelling MILD combustion. However, several important observations arise from the full panorama shown in Appendix A. The results from several studies [28, 88, 117, 146, 180] suggest that combustion models that assume infinitely fast chemistry (mixed-is-burnt) are not adequate for MILD conditions. This means that the inherently large ignition delays caused by the dilution of the reactants with hot products cannot be accurately predicted with the equilibrium or quasi-equilibrium assumptions.

In order to capture the autoignition phenomenon and flame propagation characteristics in the MILD regime, the chemistry representation requires careful consideration. From the earliest [61] to the most recent [99] investigations, the use of global reaction schemes prevail due to its computational efficiency. Although global reactions provide reasonably good agreement for some major species, large discrepancies are seen between measured and predicted temperature distributions, particularly in the near burner region (e.g. [107, 146]). Neither the inclusion of extra steps to better represent the oxidation of CO in the rich side [99], nor modifications to the empirical coefficients of the ED model [88, 117, 202] has shown significant improvements on the predictions with simplified chemistry.

The failure of global reaction schemes to describe the slower reactions of MILD combustion demonstrates the need for including the intermediate reactions that take place. In general, combustion models that can incorporate multistep finite-rate kinetic mechanisms provided the most accurate predictions. For example, Christo and Dally [28] used the EDC model with skeletal and detailed chemical kinetics to model a jet in hot coflow (JHC), which was designed to emulate MILD conditions. They found that not only detailed chemical kinetics, but also the effects of differential diffusion were critical for the accuracy of the predictions. It is worth mentioning that the fuel mixture used in the JHC burner had a significant hydrogen content (20% by mass). While their analysis showed reasonably good

agreement with the experimental results, the model did not capture the liftoff height for the 3% O_2 flames, and showed large discrepancies downstream where the air from the surrounds mixes with the jet and coflow causing localised extinction. The more sophisticated TPDF approach, which predicts extinction and ignition events, has the potential to address these limitations.

The TPDF model has been used to model the vitiated coflow burner (VCB) [75], which was characterised by Cabra et al. [21]. The VCB burner was intended to investigate lifted jet flames in a vitiated coflow, and hence does not operate in the MILD regime. However, the work of Gkagkas et al. [68] is a first step in understanding the reaction zone characteristics for diluted conditions similar to those of MILD combustion. Their modelling results showed that the TPDF approach with detailed chemistry was capable of predicting the ignition phenomena. In the JHC burner case, the TPDF method was found to be more accurate than the EDC model at downstream locations, but the results from both models were still comparable at upstream locations [31]. The increased computational cost of the TPDF model may not yet be justifiable for industrial design processes.

It has been suggested that the MILD regime can be considered a perfectly stirred reactor (PSR) [154, 194]. This concept have motivated several researchers (e.g. [27, 30, 45, 163]) to investigate the performance of existing detailed kinetic mechanisms for steady and transient MILD conditions. These studies examined the effects of dilution with different diluent compositions, the effects of residence time, and NO_x formation. However, the calculated compositions were rarely compared to any experimental data and the effects of heat losses were usually not included in the kinetic modelling analysis. Although the PSR approximation have provided important insight into the oxidation of hydrocarbon fuels in low O_2 processes in an intermediate temperature range for combustion ($1000-1600$ K), the influence of the flow structure on the chemical reactions cannot be neglected in a practical combustor [122].

The formation and/or destruction of NO_x has been one of the major themes in the numerical modelling of MILD combustion. Generally, the models provided qualitative predictions of NO_x emissions, when validated against exhaust gas measurements. This is not an issue related to the NO_x chemistry per se, but mostly a consequence of inaccuracies in the predictions of temperature and species concentrations from the combustion model. It has been found that the

effect of turbulence-chemistry interactions and superequilibrium O atoms must be taken into account for accurate NO_x predictions [95, 180]. Because of the reduced peak temperatures, the thermal-NO mechanism is largely suppressed, thereby favouring alternative NO_x formation pathways, which are usually insignificant in conventional combustion systems. While there is evidence that the N_2O-intermediate route significantly contributes to NO_x formation in MILD conditions [141, 180, 201], the relative importance of the prompt-NO mechanism has been reported to be minimal [10, 57, 123]. Although the conditions of intense mixing of reactants with flue gases enables the occurrence of NO-reburning [27, 141], it appears to be negligible [95, 123].

Thus far, much progress have been made on the mathematical modelling of MILD combustion this decade. However, establishing a modelling approach that provides quantitative predictions of MILD combustion across the entire combustion domain still remains a challenge. This thesis is a contribution towards that end. The furnace/burner configuration used in this project will provide well defined boundary conditions for a CFD model, and will enable the assessment of the critical modelling parameters for this unique combustion regime.

2.3 Laser Doppler Anemometry

Described in this section is the laser diagnostic technique used in this study to measure the flow field. The fundamental theories and basic equations shown below were taken from Refs. [7, 53].

Laser Doppler anemometry (LDA), also known as laser Doppler velocimetry (LDV), is a well-established laser diagnostic technique used to measure instantaneous velocity components at a single point in space . This technique requires that the examined flow be seeded with particles that accurately follow the flow. The actual flow velocity is indirectly determined from the velocity of the tracer particles, assuming that the relative velocity between the particles and the flow is negligible.

The various components of a typical modern LDA system are illustrated in Figure 2.7. Although there are other possible configurations, most features of commercial systems can be described by this schematic diagram. A continuous
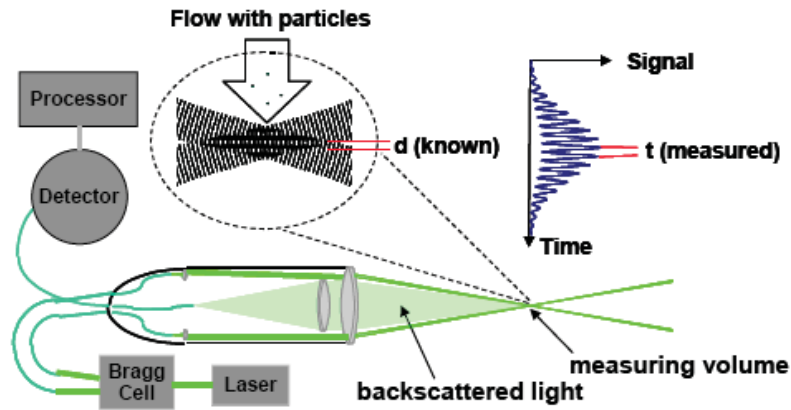
Figure 2.7: Typical optical arrangement for dual-beam LDA operating in backscatter (adapted from Refs. [7, 40]).

wave, monochromatic, coherent laser is used as the light source. The laser beam is split into two beams of equal intensity by a beam splitter in the transmitter box. The most common beam splitter is the Bragg cell, which also forces a frequency shift on one of the beams to allow directional sensitivity. The split laser beams are transmitted through optical fibre cables, and then collimated, before reaching the front lens of the transmitter probe. The incident beams intersect at the focal point creating wave interference patterns. This interference pattern represents the measurement volume, which is sometimes referred to as probe volume.

The series of light and dark bands in the intersection volume are known as fringes. The interference fringe model shown in Figure 2.8 was proposed by Rudd [162]. Although other models exist, the fringe model provides a simple and intuitive description of the principles of LDA. The distance between the fringes, δ_f, is a function of the wavelength of light, λ, and the half-angle between the two incident beams, $\theta/2$ such that;

$$\delta_f = \frac{\lambda}{2\sin(\theta/2)} \tag{2.19}$$

Since the laser beam intensity has a Gaussian distribution, the dimensions of the measurement volume depend on the beam waist diameter, d_w, at the intersection region. Therefore, the probe volume is described as an ellipsoid with axes given by

Figure 2.8: LDA measurement volume and fringe model parameters [40].

$$d_x = \frac{d_w}{\cos{(\theta/2)}}, \quad d_y = d_w, \quad d_z = \frac{d_w}{\sin{(\theta/2)}}. \tag{2.20}$$

Usually the half-angle is quite small ($\theta/2 < 6°$), and thus $\cos{(\theta/2)}$ is approximately unity, leading to $d_x = d_y = d_w$. Because the two axes have approximately equal length, d_w is commonly referred to as the nominal diameter. The beam waist or nominal diameter can be determined from

$$d_w = \frac{4\,f\,\lambda}{\pi E D_L}, \tag{2.21}$$

where f is the focal length of the front lens, E is a beam expansion factor, and D_L is the beam waist diameter of the collimated laser beam before being focused by the front lens. Another important parameter of the fringe model that affects the quality of the measurement signal is the number of fringes, N_f. The number of fringes in the probe volume is expressed as

$$N_f = \frac{d_x}{\delta_f} = \frac{2\,d_w \tan{(\theta/2)}}{\lambda}. \tag{2.22}$$

As the tracer particles introduced to the flow move through the measurement volume light is scattered. These particles act as moving receivers and transmitters of light waves, and their motion causes a change in frequency corresponding to the Doppler shift. By introducing a fixed frequency shift on at least one of the beams, a moving fringe pattern is generated in the measurement volume. This allows the "sign" of the local velocity to be determined, since particles moving in one

direction produce a higher frequency signal than the ones moving in the opposite direction. The total frequency signal, f_r, is readily captured on a photodetector and is given by the following relationship,

$$f_r = f_{sh} + f_D = f_{sh} + \frac{u_\perp}{\delta_f} = f_{sh} + \frac{2\sin(\theta/2)}{\lambda}u_\perp, \qquad (2.23)$$

where f_D is the frequency difference due to the Doppler effect, f_{sh} is the frequency shift used to eliminate direction ambiguity, and $u_\perp$ is the fluid velocity component perpendicular to the interference fringes. The f_r signal varies according to discrete oscillations in the intensity of scattered light from the particles. These so-called burst signals, which are sinusoidal waves within a Gaussian envelope, are usually detected by photomultipliers. The recorded current pulses are processed and translated into the local velocity as described in equation 2.23.

One strength of the LDA technique is the ability to simultaneously measure more than one velocity component. For a two-velocity component system, another measurement volume with a different color is required in a plane orthogonal to the first probe volume. Interference color filters are used to eliminate any cross-sensitivity between the two wavelength signals at the photodetectors. To ensure spatial coincidence and thus high data rates, the alignment of the transmitting and receiving optics is critical. As such, the receiving optics are conveniently integrated into the transmitting probe in backscatter arrangements (see Figure 2.7). Although easier to traverse with almost no need for alignment, back scatter probes typically receive lower intensity signals compared to forward scatter configurations.

An important issue in the LDA technique is the selection of seeding particles. The tracer particles must be small enough to accurately track the flow, and yet sufficiently large to scatter light and improve the signal quality. While the scattering behaviour depends on the particle material, the incident laser power, and the detection system, the tracking characteristics are influenced by the particle shape, size, concentration, and density relative to the fluid. Under the conditions of homogeneous and time-independent turbulence, the motion of very small spherical particles in a fluid with constant composition is defined by the Basset-Boussinesq-Oseen equation

$$\frac{\pi}{6} d_p^2 \rho_p \frac{\mathrm{d}V_p}{\mathrm{d}t} = -3\pi\mu d_p (V_p - U_f) + \frac{\pi}{6} d_p^3 \rho_f \frac{\mathrm{d}U_f}{\mathrm{d}t} - \frac{\pi}{12} d_p^3 \rho_f \frac{\mathrm{d}(V_p - U_f)}{\mathrm{d}t}$$
$$- \frac{3}{2} d_p^2 \sqrt{\pi\mu\rho_f} \int_{t_0}^{t} \frac{\mathrm{d}(V_p - U_f)}{\mathrm{d}t'} \frac{\mathrm{d}t'}{\sqrt{t - t'}} , \qquad (2.24)$$

where d_p is particle diameter, ρ_p is particle density, V_p is particle velocity, μ is fluid dynamic viscosity, U_f is fluid velocity, ρ_f is fluid density, and t refers to time. The term on the left hand side (l.h.s.) in this equation represents the acceleration forces acting on the particle. The first term on the right hand side (r.h.s.) describes the Stoke's drag due to viscous forces. The second and third terms on the r.h.s. describe respectively the pressure gradient forces arising from the fluid and the resistance of an inviscid fluid to the acceleration of the particle. The last term on the r.h.s. is called the *Basset history integral*, which expresses the viscous drag forces arising from unsteadiness in the flow. Lift and external body forces have been neglected. It is assumed that there is no interaction between particles.

Solutions for equation 2.24 can determine whether or not the particle motion is representative of the fluid velocity in turbulent flows. The particle size and density limit the frequency range of turbulent scales that are resolved. For a given turbulence frequency, f_{turb}, the particles follow the flow when

$$d_p < \sqrt{\frac{18\mu}{2\pi\rho_p f_{turb}} \sqrt{\frac{1}{(1-s)^2} - 1}} ; \qquad s = \frac{U_f - V_p}{U_f} . \qquad (2.25)$$

Here, s is the relative slip velocity. Essentially, this relationship specifies the maximum acceptable particle diameter for a cutoff frequency at which the particles respond to velocity fluctuations with an amplitude of $(1 - s)$.

In reacting flows, additional selection criteria for particles must be considered. The seeded particles must withstand the temperatures across the reaction zone, and still be able to effectively scatter the incident laser light. Another consideration is that higher particle concentrations may be needed to allow statistically significant turbulence information in the burnt gases due to density gradients. The elevated temperatures may also restrict optical access for measurements to avoid heat losses by radiation.

The LDA technique has been widely used to measure velocity in premixed and nonpremixed combustion systems (e.g. [5, 52]). It has also been previously employed in MILD combustion furnaces [61, 64, 147, 189]. The more obvious advantage over mechanical probes is that LDA is essentially nonintrusive, and hence does not disturb the combusting flow. LDA has the advantage of having directional sensitivity, high spatial resolution, and high temporal resolution with sampling frequencies in the order of kHz. Since the produced LDA signal is linear with fluid velocity, no calibration is required. The disadvantage of LDA, compared to planar techniques such as Particle Image Velocimetry (PIV), is that simultaneous velocity measurements over large regions of the flow cannot be obtained.

The LDA measurements will provide detailed information on the flow field for a nonreacting isothermal case and a reference case operating in MILD mode with and without air preheat. The velocity data will not only be used to assess the mixing patterns inside the furnace, but also to validate a CFD model. Together they will provide original insight into the contribution of flue gas recirculation to flame stability under MILD conditions.

Chapter 3 Experimental Setup and Methodology

This chapter discusses the measurement techniques and equipment used in this research. These experimental facilities are operated by the Centre for Energy Technology at the Thebarton precinct of the University of Adelaide.

3.1 MILD Combustion Furnace and Burner

A laboratory-scale furnace was carefully designed and built for this project to investigate reacting flows operating in the MILD combustion regime. Its modular design enables a variety of parameters to be easily varied amd controlled. Figure 3.1 shows a schematic diagram of the MILD combustion furnace (MCF) and the parallel jet burner configuration. The combustion chamber has a square cross-section of 280×280 mm^2 and a height of 585 mm. It is well insulated with four layers of 38 mm thick high-temperature ceramic fibre-boards that allow only about $15-25\%$ of thermal heat to be lost through the walls for the cases of interest, as will be discussed in §7.2.3. By minimising heat losses to the surroundings, more energy is available to maintain temperatures above that required for autoignition. This provides a more stable MILD regime and avoids some limitations of previous investigations (e.g. [37]) by broadening the operating range. The insulation layers were joined using a high temperature adhesive, and high temperature gaskets were used to seal all surface joints for safety. The inner surfaces of the combustion chamber were coated with a commercial product, "Kaowool$^{\text{TM}}$ J-Coat" rigidiser, to improve the resistance to erosion caused by high gas velocities. The chamber is slightly pressurised to prevent air ingress.
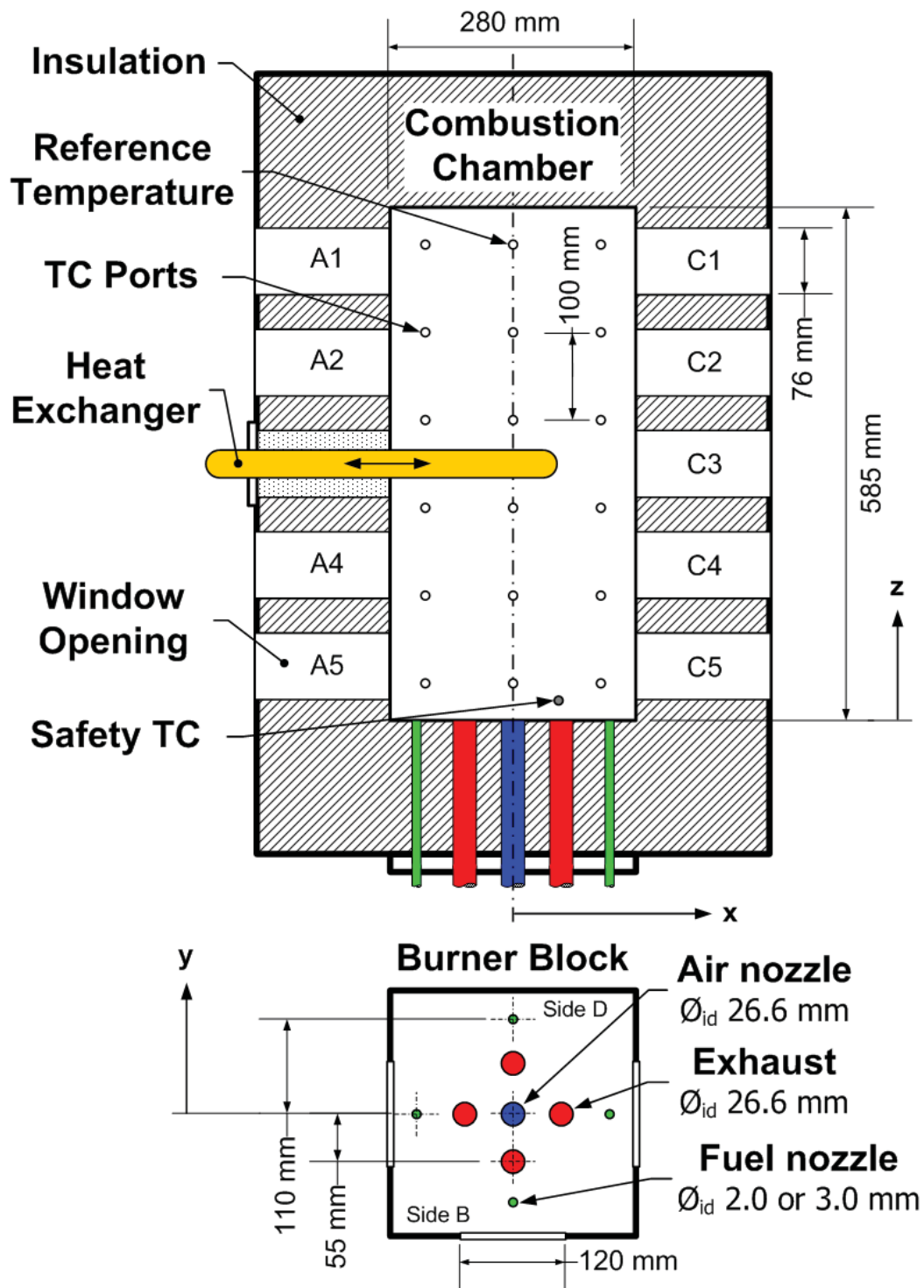
Figure 3.1: Schematic diagram of MILD combustion furnace and parallel jet burner system.

The MCF has full optical access through five openings ($120{\times}76$ mm^2) equally spaced along the vertical direction on three sides of the furnace. These openings can accommodate interchangeable insulating window plugs or UV-grade fused silica windows. A U-shaped cooling loop with variable heat exchange area is used to control the heat load (Figure 3.2). The heat exchanger can be inserted through any of the five window openings (positions A1−A5) in a cross flow relative to the incoming air and fuel streams. The cooling loop is made of a 33.4 mm outer diameter 253MA stainless steel pipe. Tap water is used as the coolant.

The configuration of reactants and exhaust ports was optimised using a Computational Fluid Dynamics (CFD) modelling study [179]. The furnace was designed for a maximum capacity of 20 kW from the fuel and 3.3 kW from air preheat. The air is preheated with a Leister LE 3000 electrical air heater that has a built-in potentiometer for air temperature control. The burner consists of a single air nozzle on the axis of the furnace, and four exhaust ports and four fuel ports arranged symmetrically in a ring pattern on the same wall (see Figure 3.1). The distance between the centre of the air nozzle and the centres of the exhaust ports and fuel nozzles are 55 mm and 110 mm, respectively.

In this arrangement the incoming air stream is separated from the fuel streams by outgoing exhaust gases, much as in the fuel direct injection (FDI) concept introduced by Nakamachi et al. [127, 137] and in the IFRF burner design [194]. This ensures that the reactants are diluted with products before any combustion reaction can occur.

## 3.2 Instrumentation and Control

3.2.1 Input-output measurements

The energy balance of a thermal system plays an important role, not only in the optimisation of thermal efficiency, but also in the mathematical modelling of the combustion process. Information on the energy balance in furnaces operating under MILD conditions is either scarce or unavailable. Therefore, an attempt to quantify the losses involved in the furnace operation is made. From the First Law of Thermodynamics for constant pressure and steady-state conditions, the following conservation equation must be satisfied;
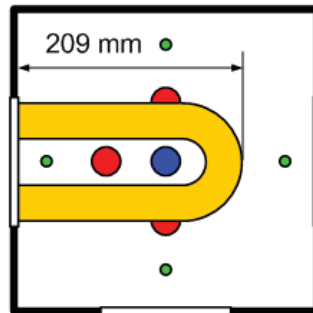
25% insertion = 0.015 m^2
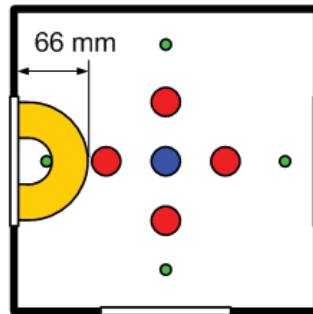
50% insertion = 0.030 m^2
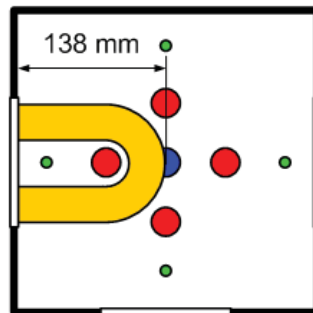
75% insertion = 0.045 m^2
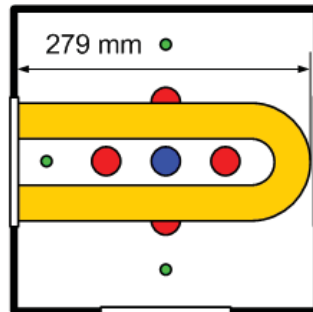
100% insertion = 0.060 m^2

Figure 3.2: Schematic diagram of heat exchanger insertion length at one of the five possible window openings (positions A1−A5).

$$\dot{Q}_{fuel} + \dot{Q}_{air} = \dot{Q}_{hx} + \dot{Q}_{exh} + \dot{Q}_{wall} + \dot{Q}_{window} + \dot{Q}_{losses} \qquad (3.1)$$

The total heat input is represented in the l.h.s. by the thermal input from the fuel and the heat content of the combustion air. The heat output consists of the heat extracted through the heat exchanger ($\dot{Q}_{hx}$) and all losses; the exhaust gas heat losses ($\dot{Q}_{exh}$), conduction heat losses through the walls ($\dot{Q}_{wall}$), radiation heat losses through the window opening ($\dot{Q}_{window}$), and all other energy losses ($\dot{Q}_{losses}$).

The diagram shown in Figure 3.3 identifies the main components and instrumentation used in this research as well as the flow paths. The energy fluxes are determined from the knowledge of flow rates and temperature measurements. The gas and water flow rates were measured with variable area flowmeters (tube and float type). The exhaust and air preheat temperatures were measured with type K thermocouples, and the inlet and outlet water temperatures with type J thermocouples, all of which with a stainless steel sheath. The temperatures of the outside walls, including the top and bottom sections, were measured with a type K surface probe. The heat loss through the walls was estimated using an average outer wall temperature and assuming one dimensional steady-state conduction. The heat loss through the window was measured with a MEDTHERM 64P-1-24-T narrow angle heat flux transducer. The other losses term closes the balance.

3.2.2 In-furnace temperature measurements

Time-averaged temperatures were measured with bare, fine-wire type R (Pt-Pt-13% Rh) thermocouples of 254 μm diameter wires and 1.2 mm bead diameter at steady-state conditions. This is sufficient for reliable measurements of the mean temperature after correction for radiation, given the low temperature fluctuations in the MILD regime, and provides satisfactory spatial resolution whilst being sufficiently robust to avoid probe breakage. For accurate positioning, the thermocouple wires were supported by a 6 mm diameter rigid ceramic sheath, with the final 5 mm left exposed. The positioning error is estimated to be ± 2.5 mm in all three directions.

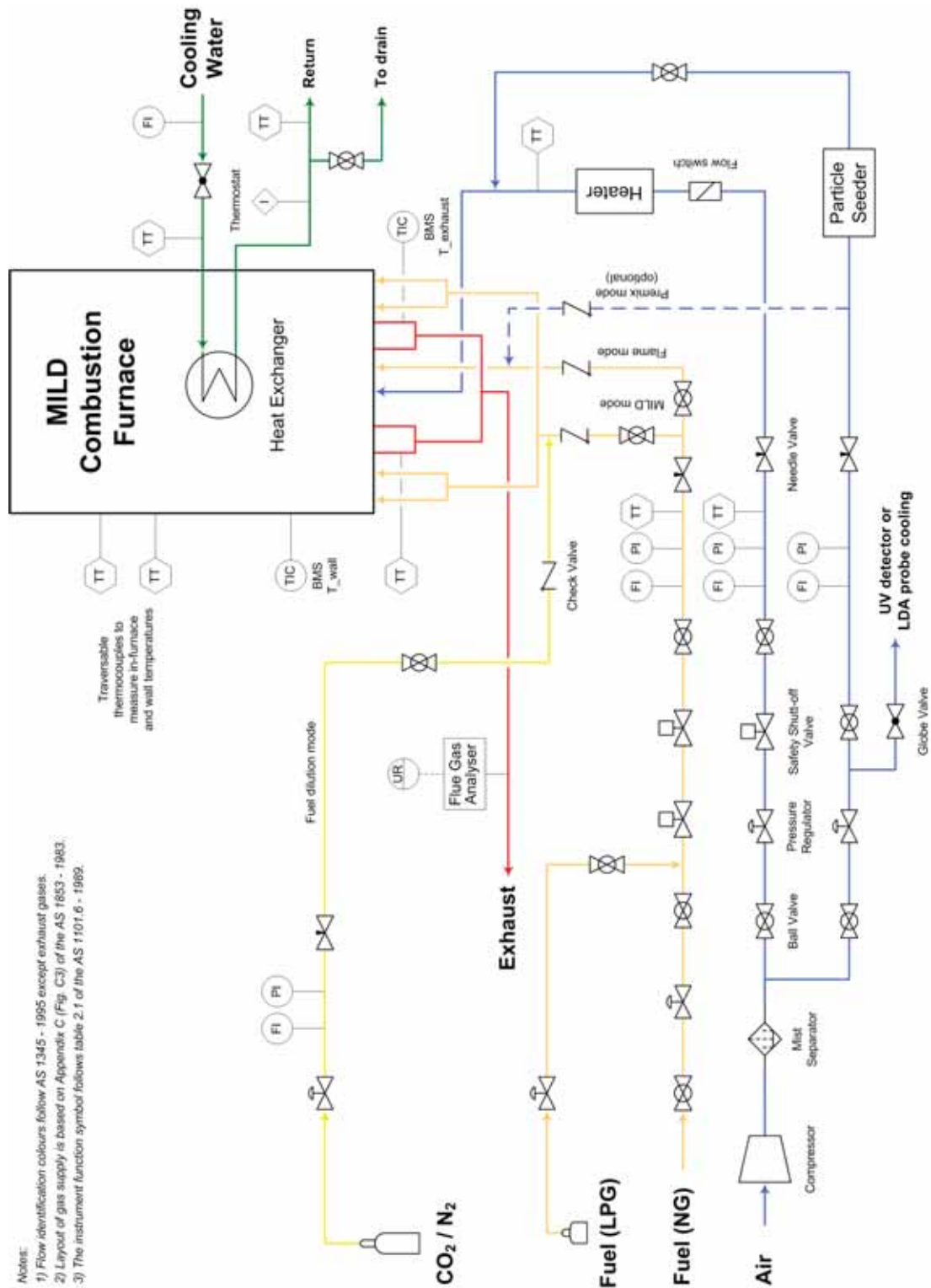Eighteen thermocouple ports were equally spaced in the vertical direction

Figure 3.3: Flow and instrumentation diagram of the MCF system.

through which a thermocouple could be traversed (Figure 3.1). Typically, temperatures were monitored simultaneously by fixed thermocouples at two regions of interest, one at the top section and one at the bottom section of the combustion chamber. The centre of the air nozzle exit plane is defined to be the origin of a Cartesian coordinate system (x, y, z). The top temperature was measured on the furnace centreline ($x = 0$, $y = 0$, $z = 542.5$ mm) and was denoted as the furnace reference temperature. The bottom temperature was measured flush with the inner surface ($x = 0$, $y = 140$, $z = 42.5$ mm) and was denoted as the reference wall temperature. Temperature profiles were also measured for selected cases. The thermocouple probes were traversed in the horizontal direction (y-axis) across different planes at each hole to provide a total of 72 points.

The differential voltage signal was continuously sampled at 1 Hz and automatically converted to temperature units with a USB-TC data logger. The mean temperatures were generally taken as the average of at least 5 minutes of steady-state operation with variations less than 1.5°C per minute. Measured temperatures were corrected for radiation losses for each probe position. A complete description of the temperature correction procedure is presented in Appendix B.

3.2.3 Exhaust gas measurements

Exhaust gas composition was measured inside the exhaust pipe with a TESTO 350XL portable gas analyser. The gas analyser was equipped with electrochemical sensors for O_2, CO, NO, NO_2 and UHC, and with a nondispersive infrared (NDIR) sensor for CO_2. The combustion products were cooled and filtered to remove moisture and particles before reaching the sensing cells.

Emission indices are expressed as the ratio of pollutant formed to the mass of fuel input [184]. The emission indices were determined solely from measured species concentrations in the exhaust pipe as

$$\text{EINO}_x \ [\text{g/kg fuel}] = \frac{X_{\text{NO}} \text{MW}_{\text{NO}} + X_{\text{NO}_2} \text{MW}_{\text{NO}_2}}{(X_{\text{CO}} + X_{\text{CO}_2}) \, \text{MW}_{\text{C}_x \text{H}_y}} \cdot 1000 \, , \qquad (3.2)$$

$$\text{EICO} \ [\text{g/kg fuel}] = \frac{X_{\text{CO}} \text{MW}_{\text{CO}}}{(X_{\text{CO}} + X_{\text{CO}_2}) \, \text{MW}_{\text{C}_x \text{H}_y}} \cdot 1000 \, , \qquad (3.3)$$

where X_i is the mole fraction of species i, and MW is the molecular weight of

species i or of the hydrocarbon fuel ($C_x H_y$). For most operating conditions, unburned hydrocarbons (UHC) were either below the detection limit of 100 ppm or below the minimum O_2 concentration ($\approx 2\%$) required for a reliable measurement. Therefore, for consistency, UHC was neglected as a possible source of carbon in the formulation. Due to the short length of the flue gas sampling probe and hose (≈ 2.5 m), the manufacturer reports that the amount of NO_2 absorbed in the condensate trap is insignificant. Consequently, both measured components of NO_x can be considered to be reliable.

To facilitate the comparison of emission levels, NO_x and CO mole fractions are reported by volume on a dry basis corrected to 3% O_2 concentration according to

$$X_i \text{ @ } O_2 \text{ reference} = \left(\frac{21 - O_2 \text{ reference}}{21 - O_2 \text{ measured}} \right) X_i \text{ measured} . \qquad (3.4)$$

3.2.4 Control system

As previously noted in §2.2.4, MILD combustion inherently requires that the furnace be preheated prior to MILD operation. A nonpremixed flame stabilised by a bluff-body was used to start the furnace from a cold state. Figure 3.4 shows details of the bluff-body configuration. In this auxiliary burner, the fuel was injected concentrically to the central air stream in flame mode. The bluff-body burner is traversable, and it was positioned according to the operating mode. During flame mode at the heat up stage, the bluff-body top surface protruded about 40 mm from the air exit plane, and during MILD combustion operation the bluff-body was retracted inside the air pipe until it reached the tube support limit stopper, which is at 70 mm upstream the exit plane. The final straight sections of the air and flame mode fuel supply lines have length-to-diameter ratios of $L/D \approx 10$ and $L/d \approx 76$ for $\varnothing_{id} = 4.6$ mm, respectively.

The flammable mixture was ignited with a 300 mm long spark plug inserted at $11°$ relative to the burner block that was connected to a 9 kV transformer. A UV sensor was mounted at the centre of a window opening for flame detection. In case of flame blowout during the heat up procedure, the fuel shutoff valve was activated. As an additional safety precaution, the signal from a thermostat was also used to activate the fuel shutoff valve in case the cooling water temperature
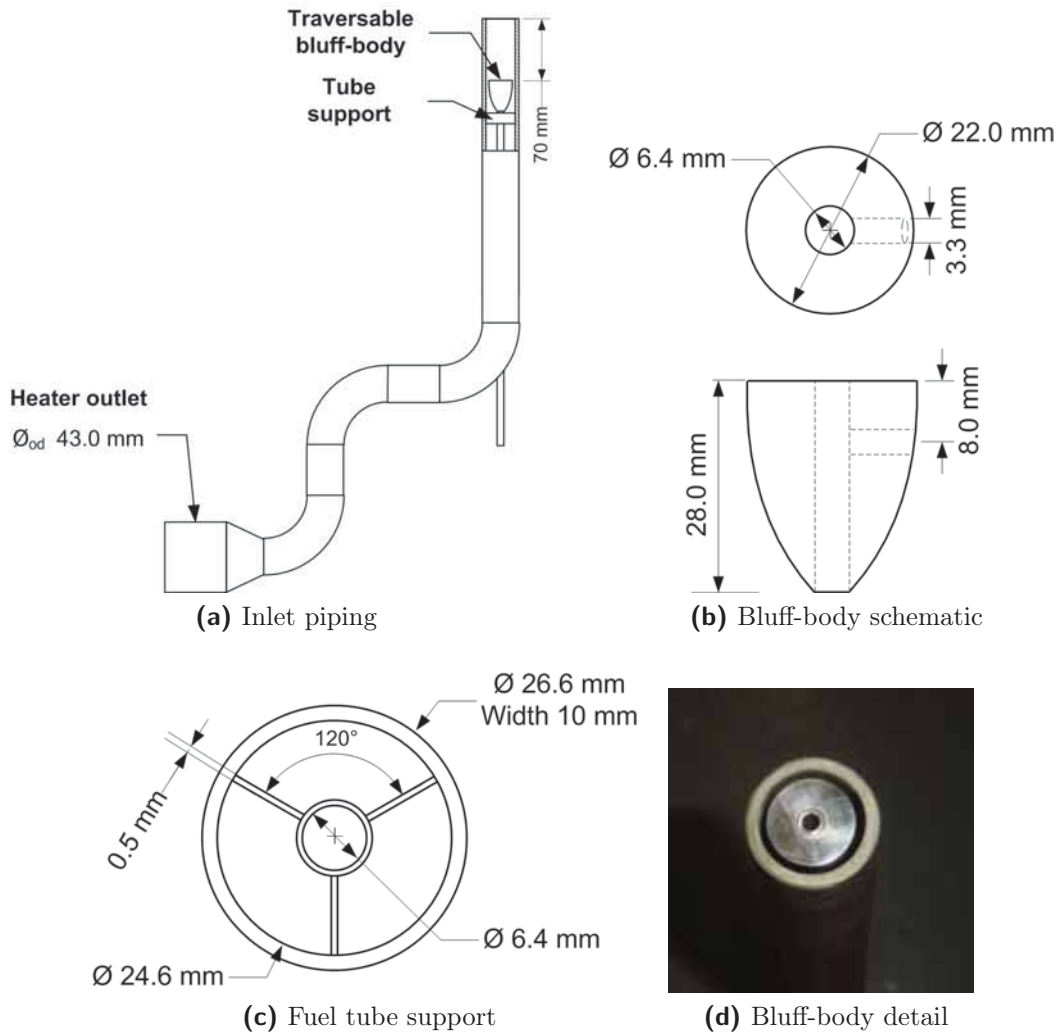
(a) Inlet piping

(b) Bluff-body schematic

(c) Fuel tube support

(d) Bluff-body detail

Figure 3.4: Bluff-body burner arrangement.

reached 70°C.

For improved safety, a surveillance-type video camera was mounted on a tripod and positioned to monitor the flame inside the furnace. The images were displayed on a conventional TV set, but not recorded.

Due to the lack of a visible flame in the MILD regime, the UV detector was not functional, and thus the fuel shutoff valve trigger was based on temperature. When the temperature at the lower corner of the furnace, which was identified as safety TC in Figure 3.1, exceeded autoignition ($\approx 800°C$) and the exhaust temperature exceeded a set threshold ($\approx 600°C$), the furnace was switched to the MILD combustion mode by injecting fuel through the four outer nozzles on the primary burner ($L/d \approx 18$ for $\varnothing_{id} = 2\,\text{mm}$). The warm up time until steady-state MILD operation was around 3 hours.

This operational procedure was integrated into a Landis & Gyr LFL 1.638 burner management system (BMS) to guarantee a safe operation during the tests (Figure 3.5). The BMS automatically controlled valve checks, purge times, ignition, and shutdown. More details of the control logic, which complied with the Australian standards, are shown in Appendix C.
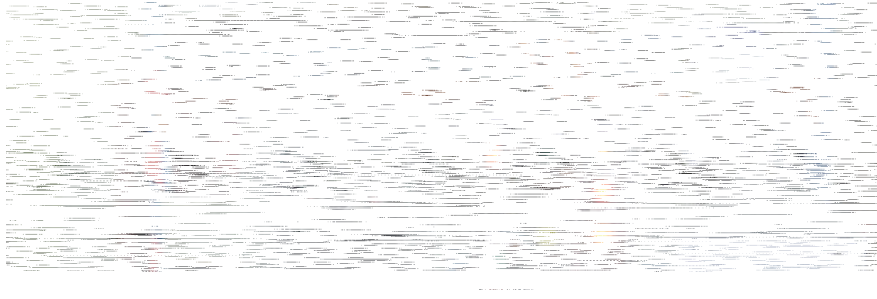

Figure 3.5: Photograph of the burner management system (BMS).

3.3 LDA System

3.3.1 Laser and optical arrangement

A two-channel commercial LDA system (DANTEC Dynamics) with a 5 W Argon-ion continuous wave laser (Coherent Innova 90) is used to measure velocity. The laser operates in TEM_{00} mode at around 2.7 W emitting light at $\lambda = 488.0$ nm (blue) and $\lambda = 514.5$ nm (green). The mean and fluctuating (rms) components of the radial (V_x) and axial (V_z) velocities were measured for selected cases operating under MILD conditions as well as for a nonreacting isothermal case with similar flow rate conditions.

The transmitting optics consisted of a beam splitter that transmitted the two pairs of beams through optical fibre cables into the transmitter probe. A fixed frequency shift of 40 MHz is introduced to one beam of each channel via a Bragg cell to eliminate directional ambiguity. The LDA probe was equipped with 400 mm focal length lens and the beam separation before the front lens was 40 mm. A beam expander was not used. The resulting individual measuring volume dimensions are 0.19×0.19×3.89 mm for the green line and 0.18×0.18×3.69 mm for the blue line. More details concerning the optical arrangement and measurement volume characteristics can be found in Tables 3.1 and 3.2.

Table 3.1: Specifications of the laser and LDA system

Laser source	Coherent Innova 90, 5 W Ar^+ (continuous wave)
LDA Manufacturer	DANTEC Dynamics
Transmitter	FibreFlow 60×41 with 60×24 fibre optic manipulators
Optical probe	2D FiberFlow with 60×71 lens, 60 mm diameter
Signal processor	BSA F80, 62N50 series
Frequency shift	40 MHz
Software	BSA Flow Software v2.12
Particle generator	swirl-type
Seeding particles	1 μm Al_2O_3 powder
Traverse	3-axis manual

Table 3.2: Characteristics of the LDA measurement volume and optics

	Channel 1	Channel 2
Velocity component	V_z (axial)	V_x (radial)
Wavelength, λ	514.5 nm (green)	488.0 nm (blue)
Beam waist diameter, d_w	0.194 mm	0.184 mm
Number of fringes, N_f	37.7	37.7
Fringe spacing, δ_f	5.15 mm	4.89 mm
Probe volume, $d_x \times d_y \times d_z$	0.19×0.19×3.89 mm	0.18×0.18×3.69 mm
Beam diameter before lens, D_L	1.35 mm	
Beam spacing before lens	40 mm	
Lens focal length, f	400 mm	
Expander ratio, E	1	
Beam half-angle, $\theta/2$	2.86°	

Optical access was provided through 5 mm thick UV-grade fused silica windows. This material was chosen because it can survive the elevated temperatures, and has a low thermal expansion and a high thermal shock resistance. The manufacturer estimates light transmittance to be higher than 93% in the visible spectrum. To ensure parallelism and avoid deflection of the incident light, high standards of surface quality (20−10 scratch-dig) and flatness ($\lambda/4$ over any 25 mm diameter) were specified. The windows were regularly cleaned to prevent transmission degradation due to dust and seeding particle deposits.

Although large window openings increase the region for measurements, they introduce heat losses and can potentially interfere with the flow of interest. To minimise radiant heat losses, the windows are built with a relatively small viewing area of 120×50 mm^2, and the opening is well insulated. The window frame arrangement is shown in Figure 3.6.

In order to protect the LDA probe from the radiated heat, a customised cooling system has been built based on a design by the IFRF [64, 189], and is illustrated in Figure 3.7. A cooling water jacket made of copper was fitted around the extremity of the LDA probe. Small air jets were used to keep the front lens below 40°C in close proximity to the window, avoiding optical distortions and breakage due to differential temperatures. A conventional fan provided further cooling for the equipment.
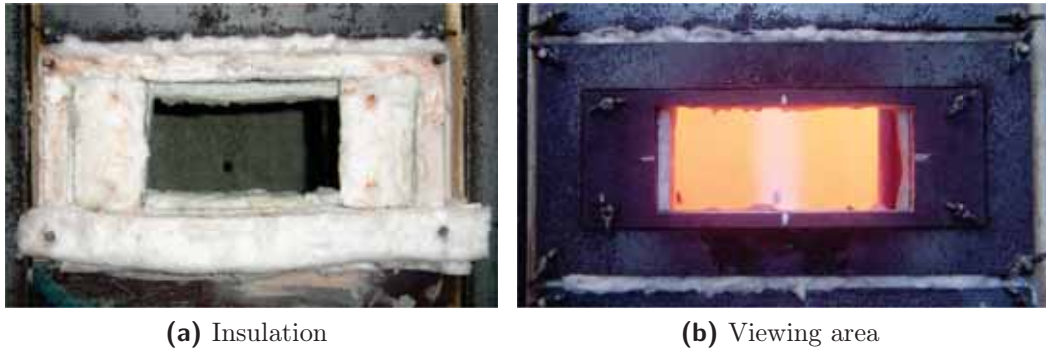
(a) Insulation   **(b)** Viewing area

Figure 3.6: Photographs of the window frame arrangement.
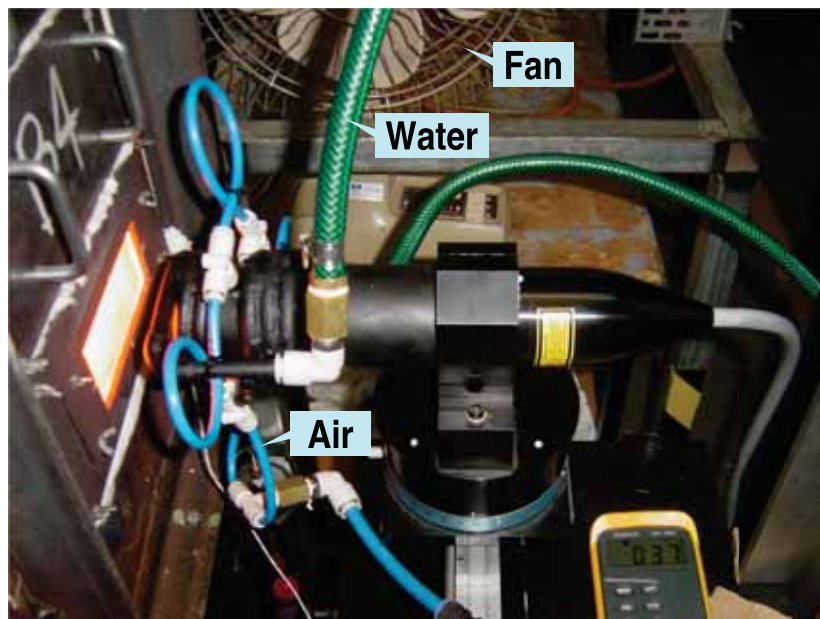

Figure 3.7: Photograph of the LDA probe cooling apparatus.

3.3.2 Particle seeding

The quality of LDA measurements greatly depends on how accurately the particle can track the fluid motion. In this study, alumina (Al_2O_3) particles with an average diameter of 1 μm and a maximum of 4 μm were used to seed the central air jet. Refer to Appendix D for more information on the particle size distribution. The high refractive index and melting point of Al_2O_3 makes it suitable for furnace environments, satisfying the selection criteria outlined in §2.3. In addition, Al_2O_3 particles have been successfully employed in previous LDA measurements in other combustion systems (e.g. [5, 115, 176]).

Large agglomerated particles that do not follow the flow tend to bias the results. To ensure a uniform delivery rate of seeding without causing agglomerations, a swirl-type seeder with a vibration mechanism has been developed. The device is similar to the cyclone aerosol generator design proposed by Glass and Kennedy [71], and is illustrated in Figure 3.8. The particle generator uses dry air from a secondary supply line, which has a separate flowmeter to control the concentration of tracer particles. The dispersed particles were introduced to the central air stream downstream of the heater (see Figure 3.3). Only $5-8\%$ of the total volume of combustion air was needed to deliver high levels of seeding, while maintaining the correct equivalence ratio at the burner exit.

The fuel stream was not seeded due to the small dimension of the fuel nozzle, $\varnothing_{id} = 2.0$ or 3.0 mm. The recirculating nature of the flow inside the furnace ensured the presence of seeding particles in all sections of the MCF. Furthermore, the first measurement location is sufficiently downstream from the burner exit, $20-30$ fuel jet diameters, to allow the presence of particles in the measurement volume.

3.3.3 Measurement locations

The LDA probe was mounted on a 3-axis manual traverse system as shown in Figure 3.9. A rail mounted on the ground ensured consistent positioning along the y-axis. A target was used to align the LDA probe along the x and z axes, so that the incident laser beams were perpendicular to the window over the measurement range (Figure 3.10). This arrangement led to estimated errors of ± 0.25 mm in the x direction and ± 0.5 mm in the y and z directions.
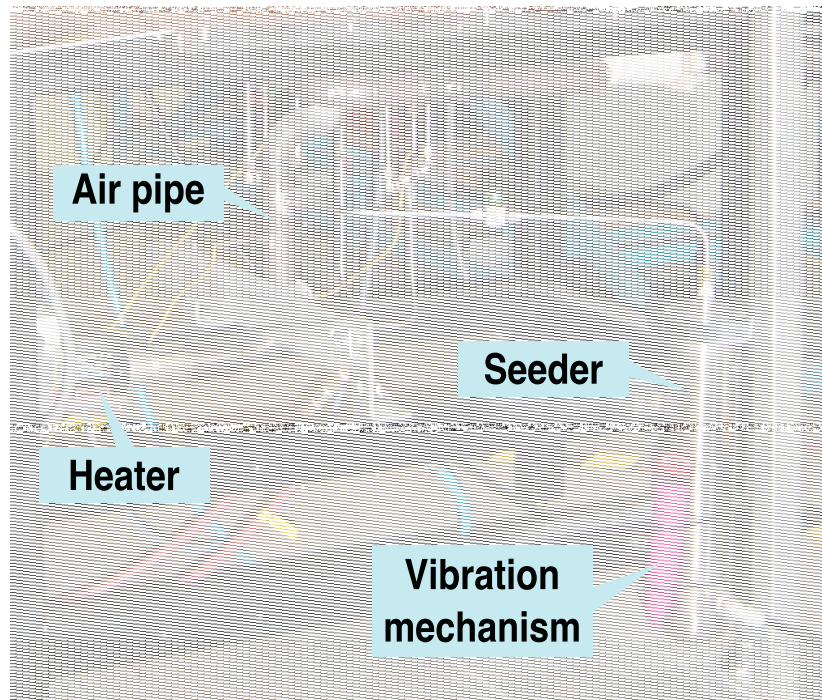
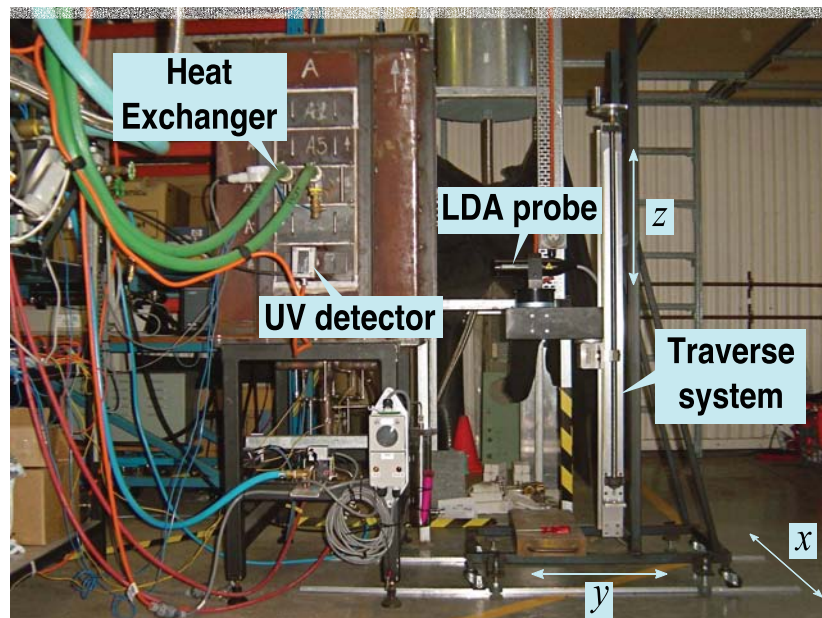**Figure 3.8:** Photograph of the particle seeding system.

Figure 3.9: Photograph of the MILD combustion furnace installations and the 3-axis traverse system.
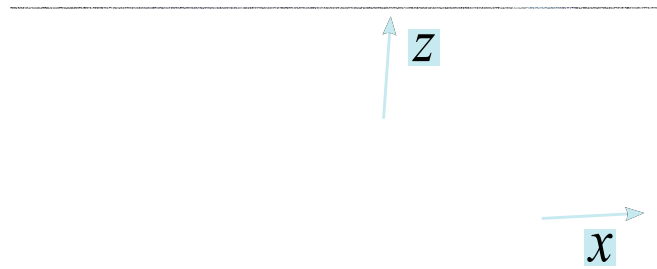
Figure 3.10: Photograph of the target used for alignment.

The velocity profiles were measured along the furnace centrelines ($x = 0$ and $y = 0$) at five different heights, $z = 60.5$, 176.5, 292.5, 408.5, and 524.5 mm. Each vertical position corresponded to the centreline of the window opening on side B of the furnace (see Figure 3.1). Measurements were also made at other locations along the x and y directions with an arbitrarily chosen offset distance from the centreline, so that asymmetries in the flow could be measured. All these points were typically separated by 5 mm in both x and y directions. Thus, the measurement points were located at $x = $ -35, -30, -25, ... , 25, 30, 35 mm and $y = $ -130, -125, -120, ... , 25, 30, 35 mm, with a total of at least 98 measurement points for each height. A summary of the measurement locations is presented in Table 3.3.

3.3.4 Data acquisition and processing

The burst signals from scattered light were detected by photomultipliers in back scatter mode and processed by a DANTEC BSA F80 signal processor that uses a robust 8 bit Fast Fourier Transform (FFT) algorithm. The signal processing included color separation, amplification, and bandpass filtering. A commercial software called DANTEC BSA Flow Software v2.12 was used to control the data acquisition process and record the data to a computer for analysis.

A code written in FORTRAN programming language was used to compute

Table 3.3: LDA measurement locations with coordinates in mm

Nonreacting conditions		
$x = 0$	$-130 \leq y \leq 35$	$z = 60.5, 176.5, 292.5, 408.5, 524.5$
$x = -10$	$-130 \leq y \leq 35$	$z = 60.5, 176.5, 292.5, 408.5, 524.5$
$-35 \leq x \leq 35$	$y = -10$	$z = 60.5, 176.5, 292.5, 408.5, 524.5$
$-35 \leq x \leq 35$	$y = 5$	$z = 60.5$
$-35 \leq x \leq 35$	$y = 30$	$z = 176.5, 292.5, 408.5, 524.5$
Reacting conditions		
$x = 0$	$-130 \leq y \leq 35$	$z = 60.5, 176.5, 292.5, 408.5, 524.5$
$x = -10$	$-130 \leq y \leq 35$	$z = 60.5, 176.5, 292.5, 408.5, 524.5$
$-35 \leq x \leq 35$	$y = -10$	$z = 60.5, 176.5, 292.5, 408.5, 524.5$
$-35 \leq x \leq 35$	$y = 5$	$z = 60.5, 176.5, 292.5, 408.5, 524.5$

the statistical moments, with all data being corrected for velocity bias. The Chauvenet's criterion was applied to filter data points that deviated from the mean value more than twice the rms value, achieving a 95% confidence level. Measurements with unacceptable statistical errors were discarded, and a log file with information on those points was generated.

For the present optical arrangement, the light intensity in the green line was 70% higher than in the blue line, measured at the output of the LDA probe. As a result fewer particles had a high enough signal-to-noise ratio (SNR) to be validated, and high data rates for coincidental measurements were difficult to obtain in acceptable acquisition times. Therefore, noncoincidental values were used for improved first order statistics. The lack of coincidental data hindered the calculations of Reynolds stress tensors and cross moments.

Data was collected with a typical average data rate of $3-4$ kHz and $50-100$ Hz in nonreacting conditions, and of $0.5-1$ kHz and $10-30$ Hz in reacting conditions, respectively for the green and blue channels. It should be noted that the volumetric expansion due to combustion generally reduces the particle density in the burnt gases, and leads to reduced data rates at some locations. For each measurement location, at least 10,000 data points were taken to compute the mean and rms velocities in the axial direction (z-axis), and 500 in the radial direction (x-axis).

3.4 Error Analysis

Measurements of physical quantities are prone to error, even in carefully planned and well designed experiments. Experimental errors may be caused by several factors and are commonly classified as random or systematic. The potential sources of error in the measurements performed in this study are reported in the following sections.

3.4.1 General sources of error

Flowmeters and pressure gauges

Uncertainties in the inlet flow rates of air and fuel affect the overall accuracy and repeatability of the operating conditions as well as the inlet velocities. The manufacturer of the variable area flowmeters specifies an accuracy of 2% of the maximum flow with repeatability of 0.25% at full scale reading [1]. For this class of flowmeters, operation near full-scale is recommended. However, this was not always possible, and hence the errors might be a little greater than the specified values. The general service pressure gauges used in conjunction with the flowmeters are another source of error in the measurement of the volumetric flow rates. According to their specification, the accuracy of the pressure gauges is listed as 1% at full scale reading. In addition to the inaccuracies of these instruments, parallax errors when reading the values from the scales of these devices are possible. However, these errors are relatively small and do not affect the experiments.

Fuel composition

Variations in the fuel gas composition may lead to noticeable changes in the fuel input power, or burner firing rate, altering the operating conditions. Hence, historical data on the natural gas composition provided by the gas supplier Origin Energy Australia was analysed. Since no significant changes in the composition were found in the monthly records for a period of three consecutive years, an average composition can be considered to be a reliable value to represent the natural gas used in the experiments. The properties of natural gas, such as calorific value, density, and molecular weight, are then determined according to

the methods described in the ISO 6976:1995 standard [96]. A maximum error of 2% is estimated for the calorific value in volumetric terms. Daily fluctuations in the composition of natural gas are not expected to affect the experimental results. In the case of LPG, variations in the composition are negligible, and the error is limited to the chemical analysis of the content of the gas cylinder, which is rather small.

3.4.2 Temperature

According to the data logger specifications, the uncertainties associated with converting the voltage signal to temperature values, which include system noise, linearisation and cold-junction compensation, produce a maximum error of $\pm 1.07°$C in a measurement range from 250 to 1768°C. When considered alone, this represents only 0.13% error in the worst case.

The method for radiation correction described in Appendix B led to a maximum correction of 9.1% and 11.7%, and a typical correction of less than 2% and 4% between raw and actual gas temperatures. Even though this process is done with great care, uncertainties in the in-furnace temperature measurements may result from the fact that the convective heat transfer, the emissivity and the wall temperature are not precisely known. To estimate the total error in the measurements, an error propagation analysis was carried out by attributing some degree of inaccuracy to these parameters. The total uncertainty is within $\pm 2.6\%$ and $\pm 3.0\%$ and is typically $\pm 1.2\%$ and $\pm 1.3\%$, respectively for the baseline case with and without air preheat. Details of the error estimation procedure and a table with the resulting errors for each thermocouple position is presented in Appendix B.

Innacuracies of the input-output temperature measurements will lead to differences in the energy balance. For better accuracy in determining the heat extracted through the cooling loop, the water flow rate was adjusted so that the difference between the inlet and outlet water temperatures was at least 5°C. The exhaust and air preheat temperature sensors were installed in such manner to avoid bias errors that occur due to conduction along the leads. Nevertheless, these measurements may contain some level of uncertainty, but it is expected to be only a few percent.

3.4.3 Global emissions

The nominal accuracies specified by the manufacturer for the gas analyser sensors are summarised in Table 3.4. During the continuous gas sampling process, the sensing cells were periodically purged with fresh air to reduce measurement uncertainties (drift in the readings). The time interval for recording the data was carefully set to allow an adequate amount of gas to react at the sensing cells. To ensure reliable measurements of UHC the instrument was switched on and the sensing cell was left to warm up for at least ten minutes. To verify the repeatability of the operating conditions, the equivalence ratio (air-to-fuel ratio) calculated from the measured O_2 concentration in the flue gas was regularly compared to the value obtained from the knowledge of the inlet flow rates of air and fuel. The difference was found to be less than 1%, which is acceptable considering the inherent errors of the flowmeters. The analyser was checked with a calibration gas to yield total NO_x ($NO + NO_2$) emission accuracies better than ± 4 ppm for the range 0 to 70 ppm, in which all data from this study lie.

Table 3.4: Nominal accuracies for the gas analysis equipment

Species	Measurement range	Accuracy
O_2	$0-25\%$	$\pm 0.8\%$
CO	$0-2000$ ppm	$\pm 5\%$
	$2001-10000$ ppm	$\pm 10\%$
CO_2	$0-25\%$	$\pm 0.3\%$ m.v. $+ 0.44$
NO	$0-99$ ppm	± 5 ppm
NO_2	$0-99.9$ ppm	± 5 ppm
UHC	$100-4000$ ppm CH_4	< 400 ppm

3.4.4 LDA measurements

The total uncertainty in the LDA measurements can be divided into three categories: calibration, data acquisition and data reduction uncertainties [125]. The calibration uncertainty represents the alignment errors in the optical arrangement. The data acquisition uncertainty is an estimate of the sources of error in the Doppler frequency measurements, which mainly consist of velocity bias, gradient bias, particle seeding bias, fringe bias, angle bias, and validation bias.

The data reduction uncertainty refers to the propagation of the previously mentioned errors to the final velocity result. The sources of error most relevant to the present LDA measurements are discussed in more detail below.

Alignment errors and fringe bias

The fringe model assumes that the fringe spacing and the velocity of the seeding particles through the measurement volume are constant to determine the Doppler frequency (f_D from equation 2.23). Thus a nonuniformity in fringe spacing caused by optical misalignment will bias the measurement results. To avoid fringe distortions, the optics must be aligned so that the laser beams cross at their waists. Since the LDA probe has been factory-aligned prior to the investigation, the calibration uncertainties of the focal length and beam separation are considered to be negligible.

According to equation 2.19, another source of error in the alignment of the optics is the half-angle. Any deviations of the incident beams when passing through the optical access will lead to uncertainties when determining the fringe spacing. As previously mentioned in §3.3.3, a target was used to align the LDA probe perpendicularly to the window maintaining the uniformity of fringe spacing in the measurement volume. In addition, the laser power and the light distribution between the blue and green channels were checked daily to maximise fringe visibility. Even though this method avoided detectable changes in the half-angle, the probe volume has shifted 1.6 mm in the y direction due to refraction. The coordinates for all measurement locations were corrected for this systematic bias.

Another possible source of uncertainty in the optical arrangement is the traverse system. Every effort was taken to reduce the errors due to spatial mismatch. Based on repeated measurements at the lowest vertical location ($z = 60.5$ mm) for nonreacting conditions, the measured repeatability was on average 3% for the mean and 4% for the rms velocity profiles.

Velocity bias and particle seeding bias

The sampling process depends on the velocity of the seeding particles. In practice, high velocity particles are sampled more often than low velocity particles. As a result, pure arithmetic averaging will skew the mean value of the statistical

distribution towards higher velocities. To correct for this velocity bias, transit time weighting was used for data processing, i.e., the time needed for a particle to travel through the measurement volume with the local mean velocity.

The bandpass filtering process can also cause velocity bias in the LDA signal. If the filter window is not set correctly, frequency signals that would otherwise be a valid velocity will not be measured. To avoid this form of validation bias, the frequency response was optimised for the measured velocity range.

The source of particle seeding bias is the relative velocity between the fluid and the seed particles. The smaller the difference between these velocities, the lower the uncertainty because the particles are able to closely follow the flow. This form of bias can increase with the level of turbulence in the flow. However, the particle size was chosen to minimise the velocity discrepancy. According to equation 2.25, Al_2O_3 particles with a mean size of 1 μm can follow flows with velocity fluctuations of up to 1.59 kHz, assuming a 1% relative slip velocity, an acceptable level for this study.

Density bias

In combustion environments, an additional bias due to density gradients needs to be considered [8]. The disturbances caused by refractive index gradients can lead to significant degradation of the laser beam profile and to changes in the light collection path within the furnace, reducing the signal transmission efficiency. Because MILD combustion reactions occur over a large volume with a nearly uniform temperature profile, the density gradients are very low relative to conventional combustion. Hence the density bias is expected to be negligible.

Other sources of error

While every effort is taken to ensure accurate measurements, other inaccuracies may occur in collecting the velocity data. Amongst the other sources of errors are the data reduction process, the LDA probe cooling system, the bluff-body positioning, the fuel inlets, and the window cavity.

The total statistical error in the data reduction process can be determined from the number of data points and the local mean velocity and turbulence level [203]. The procedure explained in §3.3.4 leads to maximum uncertainties of ±0.5% and

$\pm 1\%$ in the axial direction (z-axis), and $\pm 2.5\%$ and $\pm 5\%$ in the radial direction (x-axis), respectively for the mean and rms.

The LDA probe cooling system was essential to the velocity measurements. Although the cooling system did not affect the repeatability of the measurements, it caused a slight reduction in the data rates. Data sets taken at identical locations and conditions with and without the cooling device showed that the decrease in data rates is at most 5%.

It is acknowledged that the air inlet velocity profile is affected by the presence of a bluff-body inside the air pipe. To minimise the inaccuracies related to spatial relocation and repeatability, a stopper was installed to ensure that the bluff-body remained retracted inside the air pipe at 70 mm upstream the exit plane during the tests (see Figure 3.4). Although desirable, it was not possible to retract the bluff-body even further upstream due to space limitations. The effect of the bluff-body positioning is expected to be minor and restricted to radial locations close to the furnace centreline. Furthermore, it has little effect on the overall mixing patterns inside the furnace.

Because the four fuel nozzles on the primary burner have a relatively small dimension ($2-3$ mm), changes in jet diameter can affect the inlet velocity and potentially modify the reaction zone structure. Although the fuel inlets may be subject to slight thermal expansion during the operation of the furnace, this effect is expected to be negligible. In addition, great care was taken to avoid scale deposits on the heated tubes.

The window openings that provided optical access to the combustion chamber are essentially cavities with a depth equivalent to the insulation thickness (≈ 152 mm). These window cavities can potentially interfere with the flow field and bias the results. LDA measurements inside the window cavity showed velocities lower than 0.2 m/s, and therefore suggesting that the cavity does not introduce a significant problem to the flow structure inside the furnace, and is definitely not likely to modify the general trends which are observed.

Chapter 4 Numerical Modelling

4.1 Introduction

As computer processing speeds continue to increase, numerical modelling prove an essential complement to combustion theory and experimental investigations. In this context, computational fluid dynamics (CFD) and reactor modelling approaches has found extensive application in the solution of complex reacting flows with practical relevance. It is not only a powerful design tool, due to its adaptability and cost effectiveness, but also an important analysis tool.

The furnace/burner configuration used in this research provides well defined boundary conditions that lends itself to mathematical modelling. A CFD model is developed to assess the suitability of current combustion models to predict the distributed and diluted reactions of MILD combustion. It is also used to better understand the thermal and flow fields and the parameters that influence their structure. The results from the CFD model will be validated against the experimental data shown in Chapters 5, 6, and 7. In addition to the CFD model, a perfectly stirred reactor (PSR) model and equilibrium calculations are used to evaluate the chemical kinetic effects on the combustion process. This chapter summarises the model parameters and specifies the boundary and initial conditions.

4.2 CFD Model Description

The CFD modelling performed in this study used the commercial package FLUENT 6.3 [62]. This finite volume code solves the Reynolds-averaged Navier-Stokes (RANS) equations for the conservation of mass, momentum, and energy, together

with turbulence closure and radiation models. Additional transport equations are also solved, when a combustion model is used to describe the coupling between the flow field and chemical reactions. A steady pressure-based segregated solver is used with implicit formulation. A second-order discretisation scheme was used to solve all governing equations with the SIMPLE algorithm for pressure–velocity coupling.

Solution convergence was ensured by two criteria. First is ensuring that the residuals of the solved equations drop at least three orders of magnitude (10^{-3}) for all variables, except for the energy and radiation equations for which a threshold of 10^{-6} was used. The second convergence criterion is ensuring that the value of a sensitive variable at a critical spatial location has stabilized and is no longer changing with iterations. For example, monitoring the average temperature on the surface of the heat exchanger, the O_2 concentration at the exhaust ports, or the axial velocity profile along the $y-$axis through the furnace centreline at a certain axial location.

4.2.1 Computational domain

The CFD model developed for this study is based on the configuration and dimensions described in §3.1. The computational domain consisted of two volumes: the combustion chamber and the heat exchanger with 25% insertion at position A3. Although there is symmetry along the $x - z$ plane, the domain could not be simplified to one half of the furnace because the inlet air velocity profile is not symmetrical (refer to §4.2.6).

The preprocessing software GAMBIT 2.3 [63] was used to create the geometry as well as generate the mesh. The unstructured three-dimensional hybrid mesh is illustrated in Figure 4.1 as well as details of the air, fuel, and water inlets, and the exhaust and water outlets. A boundary layer was applied to both internal and external surfaces of the heat exchanger to accurately capture the heat transfer from the furnace gases to the cooling water stream. The mesh was refined near the burner exit plane (≈ 100 mm downstream) for smooth representation of the initial stages of flow development. For the same reason, the tip of each fuel tube (50 mm upstream) was also represented in the domain. Size functions were used to ensure a gradual increase in cell size and maintain skewness and aspect ratio
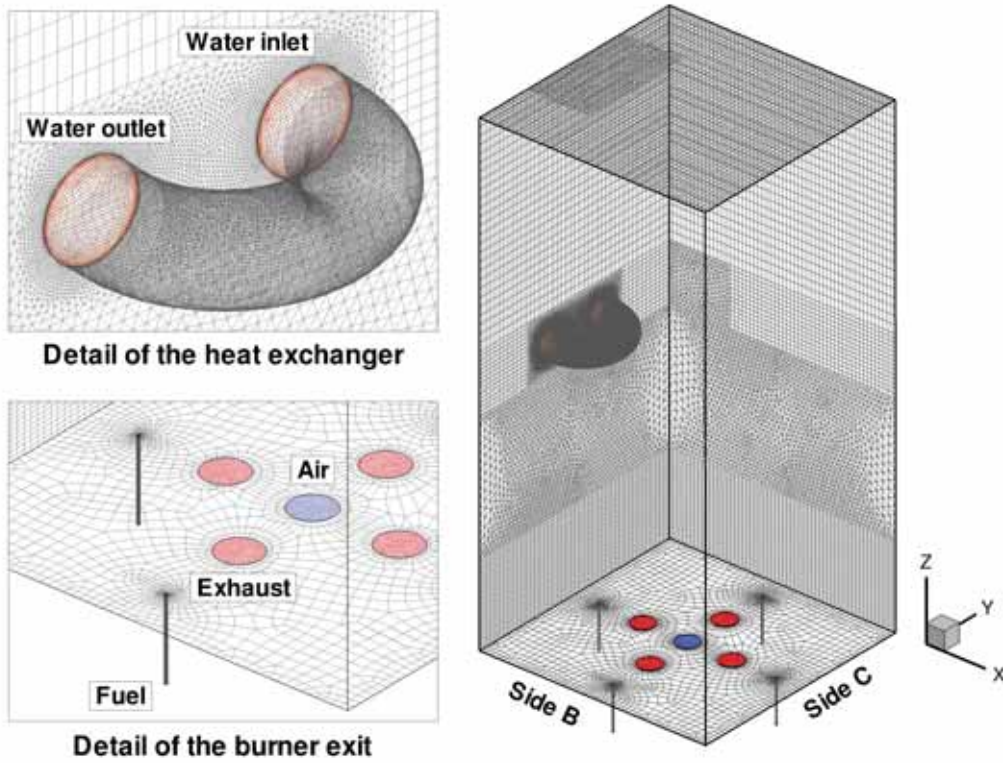
Figure 4.1: Meshed computational domain for the MCF.

below 0.82 and 10, respectively.

A grid resolution study was performed to achieve grid independent results. Three different mesh sizes, which contained about 0.6, 1.25 and 2.5 million hexahedral and tetrahedral cells, were tested. Based on comparisons of velocity and temperature profiles between the three meshes for a reference operating condition, the mesh with 1.25 million cells was selected. The finest mesh showed only marginal improvements for a much higher computational cost.

4.2.2 Turbulence models

Many techniques are available to model the unclosed Reynolds stress terms in the momentum equations. The $k - \epsilon$ turbulence is a semiempirical approximation based on the Boussinesq gradient approximation that assumes isotropic turbulence [197]. This approach solves transport equations for turbulence kinetic energy (k) and its dissipation rate (ϵ), with both equations containing a number

of empirical constants. The three variants of this model are: the standard $k - \epsilon$ (SKE), the renormalization group (RNG), and the realizable $k - \epsilon$ (RKE) models. The RNG and RKE models attempt to address the deficiencies of the SKE model by including additional terms and functions, or by modifying the formulation for turbulent viscosity to improve the accuracy for round and planar jets, swirling flows, or flows involving recirculation regions [197]. A simpler modification to the SKE model to compensate for the round-jet/plane-jet anomaly is to adjust the standard constants $C_{\epsilon 1}$ and $C_{\epsilon 2}$ in the dissipation rate equation.

A more rigorous alternative to the two-equation models mentioned above is the Reynolds stress model (RSM). The RSM takes into account the effects of anisotropy in the turbulence field and solves the exact transport equations for the Reynolds stresses, together with an equation for the dissipation rate. In principle, the RSM yields more accurate predictions for flows involving rotation, swirl, and sudden changes in strain rate.

In this thesis, the performance of the three variants of the $k - \epsilon$ turbulence model, two modified versions of the SKE model and a Reynolds stress model (RSM) was evaluated for an isothermal nonreacting condition. The turbulence model that provided the best agreement with the experimental data for jet spread and decay rates for that condition was applied to the reacting cases. A non-equilibrium wall function was needed to accurately describe the heat transfer process on the surface of the heat exchanger.

4.2.3 Combustion models

In a multicomponent reacting flow, chemical reaction rates appear as a source term in the Reynolds-averaged conservation of species equation. One of the main challenges in turbulent combustion is modelling the mean reaction rate with an adequate representation of the chemistry. In this study, the closure for the chemical source term is based on volumetric reaction methods. The performance of two combustion models for predicting the oxidation of methane in MILD conditions is assessed. Those are the finite-rate/eddy dissipation model (FRED) with a two-step global reaction and the eddy dissipation concept (EDC) with a multistep chemical kinetic mechanism. A brief description on how each combustion model handles the turbulence-chemistry interaction and chemical kinetics is given

below.

The eddy dissipation model (ED) is a modification of the eddy-break-up (EBU) model of Spalding [172] developed by Magnussen and Hjertager [120]. It is based on the assumption that combustion is fully controlled by turbulent mixing, thereby neglecting the influence of chemical kinetics. In the ED model, the over-all production rate of species i due to reaction r, $w_{i,r}$, is taken as the minimum of the following three rates:

$$\omega_{i,r} = \min\left(\rho A Y_F \frac{\epsilon}{k}, \; \rho A \frac{Y_O}{\nu_{(O/F)}} \frac{\epsilon}{k}, \; \rho A B \frac{Y_P}{(1 + \nu_{(O/F)})} \frac{\epsilon}{k}\right), \tag{4.1}$$

where ρ is the density, A and B are empirical constants, $\nu_{(O/F)}$ is the stoichiometric oxidiser-to-fuel mass ratio, Y is the mean mass fraction, and the subscripts refer to fuel (F), oxidiser (O), and product (P). In equation 4.1, combustion reactions are initiated once $k/\epsilon > 0$. This approach can cause premature ignition in regions where the chemical reactions are not mixing-limited. To prevent this, a finite-rate chemistry (FR) term based on the Arrhenius rate expression is included in the model formulation. The FRED model then uses the lowest of these two overall reaction rates, Arrhenius rate or eddy dissipation rate, to determine the chemical source term.

Since every reaction has the same mixing time scale (k/ϵ in equation 4.1), the FRED model is prone to large discrepancies for multistep reaction schemes. Therefore, it is limited to global reactions and cannot predict radical species. A two-step reaction scheme that includes six chemical species (CH_4, O_2, N_2, CO, CO_2 and H_2O) was used with the FRED model. Methane is first oxidised to CO and H_2O, and subsequently, CO burns to form CO_2 (refer to equations 2.12 and 2.13).

The EDC model, which is an extension of the ED model, allows detailed chemical kinetic mechanisms to be incorporated in the calculations [119]. The EDC model assumes that chemical reactions take place in small turbulent structures, called fine scales. The size of these fine scales (ξ^*) is determined from turbulence quantities as

$$\xi^* = C_\xi \left(\frac{\nu\epsilon}{k^2}\right)^{\frac{1}{4}}, \tag{4.2}$$

where the asterisk (*) denotes fine-scale quantities, ν is the kinematic viscosity, and C_ξ is a volume fraction constant equal to 2.1377. Combustion is then assumed to occur within the fine structures over a characteristic residence time (τ^*) defined as

$$\tau^* = C_\tau \left(\frac{\nu}{\epsilon}\right)^{\frac{1}{2}}, \tag{4.3}$$

where C_τ is a time scale constant equal to 0.4082. Finally, the chemical source term for species i is given by;

$$\omega_i = \frac{\rho(\xi^*)^2}{\tau^*[1 - (\xi^*)^3]} (Y_i^* - Y_i), \tag{4.4}$$

where Y_i^* is the fine-scale species mass fraction after reacting in a constant pressure reactor with a residence time of τ^*. The evolution of Y_i^* depends on the numerical integration of the chemical kinetic mechanism. The skeletal mechanism developed by Smooke et al. [170] for methane, which involves sixteen species (CH_4, CH_3, H, O_2, HO_2, H_2, O, OH, H_2O, CH_2O, HCO, CO, CO_2, CH_3O, H_2O_2, and N_2) and 46 reactions, was used with the EDC model.

For a detailed reaction scheme like the Smooke mechanism, direct integration is computationally expensive, because the system of ordinary differential equations (ODE) is invariably stiff. To reduce the computational cost of integration, the in situ adaptive tabulation (ISAT) method developed by Pope [156] is used. Numerically accurate solutions are ensured here by adopting an ISAT error tolerance of 1.0×10^{-6}, and an ODE error tolerance of 1.0×10^{-8}. The error tolerance for the ISAT table (ϵ_{tol}) was determined by examining the influence of different values, namely 1.0×10^{-3}, 1.0×10^{-4}, 1.0×10^{-5}, and 1.0×10^{-6}, on the O_2 concentration at the exhaust. The same ISAT error tolerance of 1.0×10^{-6} has been previously used for the Smooke mechanism to yield high levels of accuracy in calculations of turbulent lifted flames in vitiated conditions similar to those of MILD combustion [76]. The average time per iteration is around 40 minutes with a mesh consisting of 1.25 million cells for the EDC-Smooke case with $\epsilon_{tol} = 10^{-6}$ on a 64-bit Linux box with an Intel Core 2 Duo 2.66 GHz processor and 4 GB of RAM.

4.2.4 Radiation model

The intensity of thermal radiation is a function of the fourth power of temperature, and thus may have a significant influence on the predictions of heat transfer and properties like the concentration of radical species. The discrete ordinates (DO) model [157] was adopted to account for the radiative heat transfer within the furnace, with absorption coefficients computed using the weighted sum of gray gases model (WSGGM) [169]. The DO model solves transport equations for radiation intensity for a number of discrete solid angles across the computational domain, and is applicable across a wide range of optical thicknesses. Since the optical thickness in furnaces operating in the MILD regime is not well known, the DO model is considered suitable for this study. An angular discretisation of 2×2 and a pixelation of 1×1 was specified.

4.2.5 NO$_x$ post-processor

Calculations of NO$_x$ production are based on the assumption that the NO chemistry is much slower than the fuel oxidation and mixing processes, and therefore can be decoupled and dealt with in a post-processing stage. The post-processor calculates NO reaction rates using the previously computed velocity, turbulence, temperature and species concentration fields [62]. This approach is appropriate because NO concentrations are too small to influence the heat release. In this study, the thermal, prompt and N$_2$O-intermediate formation pathways of NO are considered as well as the reburn destruction route (refer to §2.1.1). To determine the relative importance of each NO formation mechanism, each model was also individually employed in the calculations. For the sake of clarity, a brief description of each NO$_x$ model available in FLUENT is provided below.

Assuming a quasi-steady-state approximation for N atoms, which is valid for most combustion cases, except in highly fuel-rich conditions, the thermal-NO formation rate is given by;

$$\frac{\mathrm{d}\,[\mathrm{NO}]}{\mathrm{d}t}\,(\text{thermal})\,\left[\mathrm{mole/m^3s}\right] = 2k_{f1}\,[\mathrm{O}]\,[\mathrm{N_2}]\left(\frac{1 - \frac{k_{b1}k_{b2}[\mathrm{NO}]^2}{k_{f1}k_{f2}[\mathrm{N_2}][\mathrm{O_2}]}}{1 + \frac{k_{b1}[\mathrm{NO}]}{k_{f2}[\mathrm{O_2}]+k_{f3}[\mathrm{OH}]}}\right) \qquad (4.5)$$

where k_{fr} is the forward (f) and k_{br} backward (b) rate of reaction r of the extended Zel'dovich mechanism (equations $2.1-2.3$), and the square brackets denote molar concentration of species i. In the Arrhenius form, the rate coefficient is expressed as $k = AT^{\beta} \exp(-E/RT)$, where A is the pre-exponential factor, β is the temperature exponent, E is the activation energy for the reaction, R is the universal gas constant, and T is the absolute temperature. The values of the rate constants A, β, and E are taken from the evaluation of Dean and Bozzelli [47].

The concentrations of all species required to compute the rates of formation and/or destruction from equation 4.5 are directly obtained from the predictions of the kinetic mechanism. When detailed chemistry is not available, i.e., when global chemistry is used, the concentration of the O and OH radicals are estimated from partial-equilibrium assumptions.

The prompt-NO formation process is modelled according to the global reaction rate proposed by De Soete [46] as follows:

$$\frac{d\,[NO]}{dt}\,(\text{prompt})\,\left[\text{mole/m}^3\text{s}\right] = f_{pr}\,C\left(\frac{RT}{p}\right)^{a+1}[O_2]^a\,[N_2]\,[\text{FUEL}]\,\exp\left(\frac{-E_a'}{RT}\right),$$

$$(4.6)$$

where p is pressure, $C = 6.4 \times 10^6$ 1/s, $E_a' = 303{,}474.125$ J/mol, and the fuel concentration refers to a set of fuel species defined as sources of prompt-NO (e.g. CH_4, CH_3, etc).

The correction factor, f_{pr}, which incorporates the effect of fuel type, is given by;

$$f_{pr} = 4.75 + 0.0819x - 23.2\phi + 32\phi^2 - 12.2\phi^3 \qquad (4.7)$$

where x is the number of carbon atoms in the hydrocarbon fuel molecule, and ϕ is the global equivalence ratio. Equation 4.7 is an empirical correlation found for aliphatic alkane hydrocarbon fuels and valid within a range of $0.6 \leq \phi \leq 1.6$.

In equation 4.6, the oxygen reaction order, a, is related to the oxygen molar fraction in the flame as;

$$a = \begin{cases} 1.0, & X_{O_2} \leq 4.1 \times 10^{-3} \\ -3.95 - 0.9 \ln X_{O_2}, & 4.1 \times 10^{-3} < X_{O_2} \leq 1.11 \times 10^{-2} \\ -0.35 - 0.1 \ln X_{O_2}, & 1.11 \times 10^{-2} < X_{O_2} < 0.03 \\ 0, & X_{O_2} \geq 0.03 \end{cases} \qquad (4.8)$$

A simplified form of the chemical system shown in §2.1.1 is used to calculate the formation of NO via the N_2O-intermediate mechanism. Considering only two reversible elementary reactions, equations 2.6 and 2.7, the net production rate of NO is expressed as

$$\frac{d\,[NO]}{dt} \,(N_2O \text{ interm.}) \,[mole/m^3s] = 2 \left(k_{f2}\,[O]\,[N_2O] - k_{b2}\,[NO]^2 \right). \qquad (4.9)$$

The concentration of nitrous oxide needed to solve equation 4.9, assuming a quasi-steady-state, is given by;

$$[NO_2] \,[mole/m^3] = \frac{k_{f1}\,[N_2]\,[O]\,[M] - k_{b2}\,[NO]^2}{k_{b1}\,[M] + k_{f2}\,[O]} \qquad (4.10)$$

where M may be any other species (third body). The forward and backward rate coefficients for equations 2.6 and 2.7 have been widely reported in the literature (e.g. [47, 70]). The concentration of N_2, O_2, M, and O atoms is determined in the same manner as specified for the thermal-NO model.

Reburning is a process of NO_x destruction that occurs through reactions of hydrocarbon radicals with NO, leading to the formation of hydrogen cyanide and other minor intermediate radical species. For hydrocarbon diffusion flames, the following reaction set can reasonably represent the reburning mechanism;

$$CH + NO \;\rightarrow\; HCN + O \qquad (4.11)$$

$$CH_2 + NO \;\rightarrow\; HCN + OH \qquad (4.12)$$

$$CH_3 + NO \;\rightarrow\; HCN + H_2O \qquad (4.13)$$
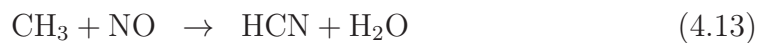
The NO_x reduction rate via reburn is then modelled as

$$\frac{d\,[NO]}{dt}\,(reburn)\,\left[mole/m^3s\right] = -k_1\,[CH]\,[NO] - k_2\,[CH_2]\,[NO] - k_3\,[CH_3]\,[NO]\,,$$
(4.14)

where k_1, k_2, k_3 are the kinetic rate coefficients for equations $4.11-4.13$. The concentrations of CH, CH_2, and CH_3 are obtained either from the results of the combustion model, or from partial-equilibrium of CH_i radicals.

Since turbulent mixing results in fluctuations in temperature and species concentrations, the interaction between the NO_x chemistry and the turbulence is taken into account by using a presumed β-shape joint PDF of temperature and O_2 concentration.

4.2.6 Boundary and initial conditions

In this study, CFD calculations of a nonreacting isothermal case and two selected reacting cases are considered. The boundary and initial conditions, based on the computational domain detailed in Figure 4.1, are listed in Table 4.1. For the exhaust ports and water outlet, the boundary conditions were set to ambient conditions (pressure boundaries).

Because there was no access to LDA measurements at the burner exit plane, the air inlet velocity profile was determined from hot-wire measurements. A portable LT Lutron AM-4204HA hot-wire with a telescopic probe was used to measure the velocity profiles for the dominant flow direction (z-axis) at approximately 9 mm downstream the jet exit. Figure 4.2 shows the results of these measurements normalised by the bulk velocity, U_o. It is readily seen that the air inlet profile is not a fully-developed symmetric flow. The asymmetry and change in the incoming air flow direction are primarily caused by the presence of a bluff-body (see Figures 3.4 and 5.2), which remains retracted inside the air pipe at 70 mm upstream the exit plane during the tests. Since no reliable measurements were available, the velocity components in the x and y directions were estimated. This was done by evaluating the tilt or injection angles from the experimental data, and calculating an average value from a vector analysis.

Table 4.1: Boundary and initial conditions for the CFD model

	Nonreacting case		Baseline case without air preheat			Baseline case with air preheat		
	Air	Fuel	Air	Fuel	Water	Air	Fuel	Water
Temperature (K)	298	294	363	298	288.2	768	298	287.6
Mass flow rate (kg/s)				7.5×10^{-5}	0.1567		7.6×10^{-5}	0.1567
k (m^2/s^2)	0.307	19.97	0.466	6.664	241.38	2.12	6.843	240.38
ϵ (m^2/s^3)	1.169	0.389	2.188	1,413.4	23,166.7	21.3	1,470.7	23,022.2
V$_x$ (m/s)	-0.25	0	-0.25			-0.25		
V$_y$ (m/s)	2.0	0	2.0			2.5		
V$_z$ (m/s)	measured profile ($U_o = 9.6$)	9.1	measured profile ($U_o = 11.9$)			measured profile ($U_o = 25.6$)		
Species mass fraction								
N$_2$	0.77	1.0	0.77			0.77		
O$_2$	0.23		0.23			0.23		
CH$_4$				1.0			1.0	
H$_2$O(L)					1.0			1.0
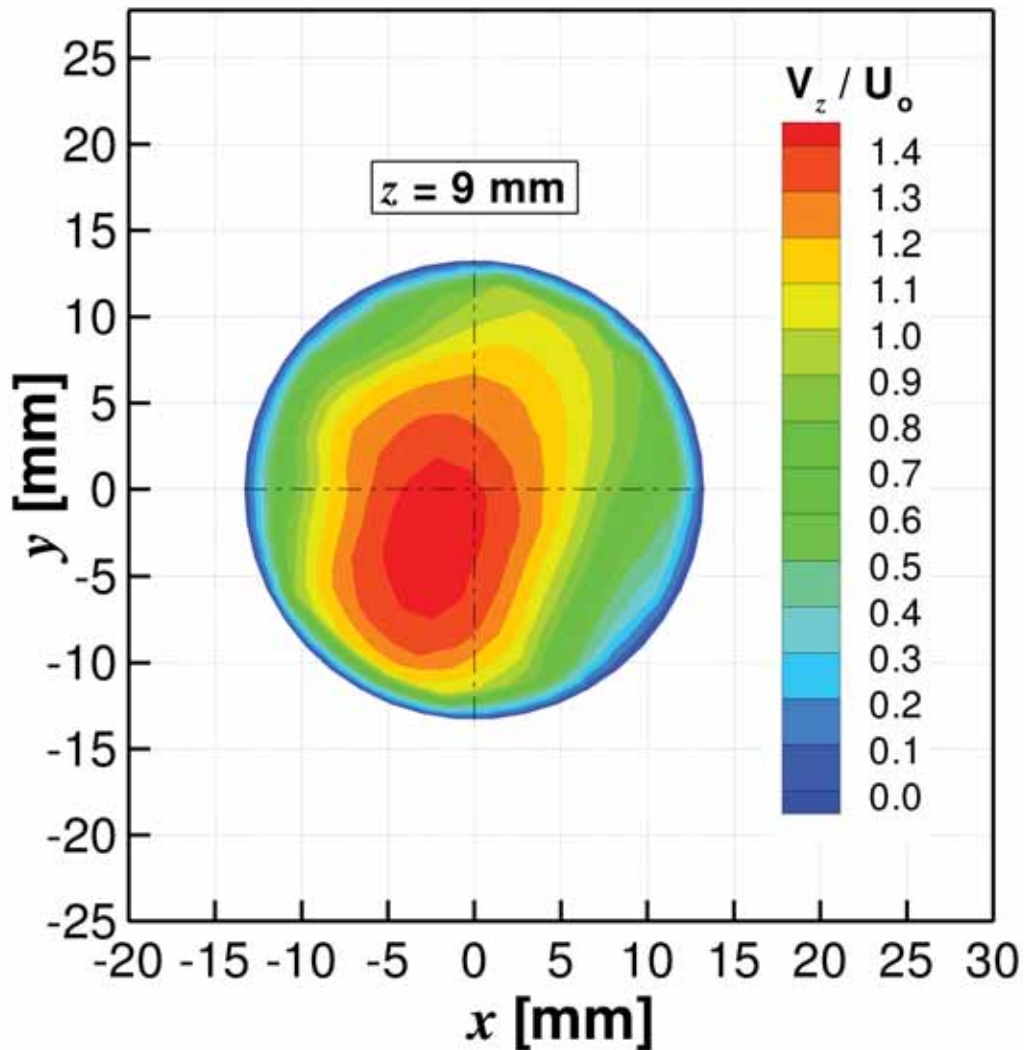
Figure 4.2: Air inlet axial velocity, V_z, profile normalised by the bulk velocity, U_o, at $z = 9$ mm.

When using the $k - \epsilon$ turbulence model, boundary conditions are required for the turbulent kinetic energy, k, and the turbulence dissipation rate, ϵ. Since no measurements were available for turbulence quantities at the inlets, the parameters were estimated from assigned values of turbulence intensity levels and integral length scales equivalent to the internal dimensions of the pipe. The numerical solution was found to be highly sensitive to the air inlet turbulence levels for the nonreacting case, but almost independent of the turbulence levels at the air exit plane for reacting conditions. Also importantly, the solution was found

to be insensitive to the turbulence levels at the fuel and water inlets for all cases. The turbulence intensities were set to 4.45%, 5.6% and 5.4%, and the integral length scales to 26.6 mm, 2.0 mm and 26.6 mm, respectively for the air, fuel and water inlets.

Heat extraction through the cooling loop, heat losses through the walls, and heat transfer across the fuel tube and air pipe are considered in the calculations.

The U-shaped cooling loop is modelled as a 3.38 mm thick 253MA stainless steel wall, with a density of 7800 kg/m^3, a specific heat of 500 J/kgK, and a thermal conductivity of 29 W/mK. A dummy species with the thermodynamic properties of liquid water ($H_2O(L)$), which does not participate in any of the reactions, was included in the chemical mechanism to represent the water running inside the heat exchanger volume. The water mass flow rate and inlet temperature were assigned measured values. It is worth highlighting that no fixed temperature or fixed heat flux has been imposed on the heat exchanger wall. Therefore, heat extraction is calculated directly from the solution in the cells adjacent to the water side and the furnace gases side ,i.e., using a coupled shell conduction approach. This allows predictions of the temperature distribution along the surface of the heat exchanger.

The combustion chamber walls are modelled as a 155 mm thick insulation (Kaowool$^{\text{TM}}$ 1400), with a density of 250 kg/m^3, a specific heat of 1100 J/kgK, and a thermal conductivity of 0.8 W/mK. The thermal conductivity of the insulation has been adjusted from the 0.25 W/mK at 1200°C reported by the manufacturer to better reproduce the energy balance estimated from the experimental data. The heat loss is then calculated from a combined convection and radiation heat transfer condition at the external wall surface, with a convection coefficient of 9.0 W/m^{2}K, a free stream temperature of 293 K, an emissivity of 0.8, and radiation temperatures with values assigned from experimental data (Table 4.2).

The fuel tubes are modelled as 20 mm thick AISI 316 stainless steel walls, with a density of 8238 kg/m^3, a specific heat of 602 J/kgK, and a thermal conductivity of 24.2 W/mK. Conduction across the fuel tube is computed using an estimated fixed surface temperature condition of 1000 K. Since the air inlet temperature was measured near the heater outlet upstream the air pipe, the mean air temperature at the exit plane was estimated from one dimensional steady-state conduction equations to be 90°C for the baseline case without air preheat, and 495°C for the

Table 4.2: Measured average outer wall temperatures

	Baseline case without air preheat	Baseline case with air preheat
Bottom	480 K	471 K
Top	347 K	338 K
Wall A	381 K	396 K
Wall B	425 K	432 K
Wall C	422 K	443 K
Wall D	384 K	393 K

baseline case with air preheat.

4.3 Reactor Model and Equilibrium Calculations

It is essential to understand the coupling between the flow field and the chemical processes to model complex reacting systems. For that reason, reactor modelling approaches and equilibrium calculations are frequently used to complement CFD modelling techniques. A perfectly stirred reactor (PSR) model, which assumes an ideal state of perfect mixing inside the control volume, is one way of assessing the influence of chemical kinetics on the overall combustion process in isolation from the fluid mechanics. Equilibrium calculations provide theoretical thermodynamic properties for the analysis of certain furnace performance parameters, such as CO concentrations, for different operating conditions.

The PSR calculations were carried out using the steady-state solver from the AURORA code of the Chemkin 4.1 package with the GRI 3.0 [148] detailed kinetic mechanism. The combustion chamber, which has a volume of 0.0459 m^3, was modelled as a nonadiabatic reactor at atmospheric pressure. The energy equation was solved for a fixed heat loss value of 5.5 kW for the conditions shown in §5.4.5 and 7.0 kW for the conditions shown in §5.4.6, which is consistent with the energy balance estimated from the input-output measurements (refer to §3.2.1). The basic reactor model considered an air stream, a fuel stream, and a recirculation stream that represents the diluted conditions of the MCF. When fuel dilution was modelled a fourth diluent stream was included. The inlet conditions

for the PSR calculations are presented in Table 4.3.

The chemical equilibrium concentrations were calculated from the NASA chemical equilibrium code [77] for an average furnace temperature of 1540 K and atmospheric pressure.

Table 4.3: Inlet conditions for PSR calculations

Stream	Mass flow rate $\dot{m}_i$ (g/s)	Temperature T (°C)	Reactant mole fraction X_i (%)
Fuel	0.31	20	$CH_4 = 0.9136$
			$C_2H_6 = 0.0436$
			$C_3H_8 = 0.009$
			$CO_2 = 0.021$
			$N_2 = 0.0128$
Air	4.92−6.24	450	$N_2 = 0.79$
			$O_2 = 0.21$
Recirculation	0.65	1000	$N_2 = 0.77$
			$H_2O = 0.15$
			$CO_2 = 0.08$
Diluent	0.15−0.75	20	$N_2 = 1.0$
	0.19−0.95		$CO_2 = 1.0$

Chapter 5 Temperature and Emission Measurements

5.1 Introduction

This chapter presents measurements of global temperature and emissions. Firstly, the operating conditions for this study are summarised and a description of the transition from conventional to MILD combustion is provided. Then, the effects of thermal input, heat extraction, air preheat, equivalence ratio, and fuel dilution on the furnace performance are examined. Finally, results of NO_x emissions, together with visual observations, are used to investigate the parameters controlling the stability of the parallel jet MILD combustion burner system (§3.1).

5.2 Operating Conditions

The parametric study investigated a total of 191 measurement points at various test conditions. Thermal equilibrium was ensured in all cases. The oxidant was air, whose temperature was varied from ambient to 780°C. Either commercial natural gas (NG) or liquefied petroleum gas (LPG) were used as the fuel to provide thermal inputs ($\dot{Q}_{fuel}$) over the range $7.5-20$ kW. In Table 5.1 the typical composition and properties of both fuels are listed.

Two alternative fuel nozzles were employed, namely; $\varnothing_{id} = 2.0$ mm or $\varnothing_{id} = 3.0$ mm. The global equivalence ratio (ϕ) ranged from 0.67 to 0.98, which is equivalent to an excess air range of $33-2\%$, respectively. The location of the heat exchanger was varied from the top window A1 (centreline at $z = 524.5$ mm) to the bottom

window A4 (centreline at $z = 176.5$ mm) and its exposed surface area varied from 0.015 m^2 for 25% or 66 mm insertion to 0.06 m^2 for 100% or 279 mm insertion (see Figure 3.2). The dilution of the fuel stream was varied, using either N$_2$ or CO$_2$, over the range $0-76\%$ by mass (Y_{dil}). In Table 5.2 a summary of all test conditions is presented.

The baseline case of this project was defined as the 2.0 mm burner with a 15 kW thermal input of natural gas, an equivalence ratio of 0.80, and 450°C air preheat (T_{air}). The reference position for the heat exchanger was position A3 (centreline at $z = 292.5$ mm) with 25% insertion.

Table 5.1: Typical fuel properties and composition

Fuel[a]	LHV[b]	$(A/F)_{st}$[c]	MW[d]	N_2[e]	CO_2	CH_4	C_2H_6	C_3H_8	C_4H_{10}	C_5H_{12}	C_6H_{14}
NG	51.154	17.11	17.71	1.278	2.084	91.36	4.364	0.62	0.20	0.055	0.04
LPG	45.993	15.66	44.07	0.73	0.05	—	1.12	96.32	1.78	—	—

[a]Gas analysis provided by Origin Energy Australia.
[b]Lower heating value (MJ/kg).
[c]Stoichiometric air-to-fuel ratio (kg/kg).
[d]Molecular weight (kg/kmol).
[e]Mole fraction X_i (%).

Table 5.2: Summary of all test conditions

Fuel type	Data points	$\varnothing_{id}$ (mm)	Y_{dil} (% by mass)	$\dot{Q}_{fuel}$ (kW)	ϕ	$\dot{Q}_{hx}$ (%)	T_{air} (°C)	$T_{furnace}$ (°C)	τ_G[a] (s)
NG	145	2.0	0	7.6−20.4	0.67−0.98	17−51	20−780	768−1368	2.8−11.4
	2	3.0	0	15.6	0.80	18	450	1295	3.9
NG/CO_2	8	3.0	38−76	15.6	0.80	16−34	454	1053−1309	1.8−3.1
NG/N_2	3	2.0	41−70	7.9−10.5	0.80	25−29	23−445	951−1129	3.7−4.5
	5	3.0	33−71	15.6	0.80	18	450	1285	1.6−3.0
LPG	1	3.0	0	15.0	0.80	21	450	1290	3.9
LPG/CO_2	10	2.0	31−71	9.9−14.4	0.75−0.81	24−41	458	1031−1261	1.3−3.5
	4	3.0	50−74	15.0	0.80	20	450	1268−1306	1.1−2.0
LPG/N_2	9	2.0	19−65	14.7	0.80	18−46	447	1046−1298	1.1−3.0
	4	3.0	45−70	15.0	0.79	20	450	1285−1326	0.9−1.8

[a]Global residence time as defined in equation 6.2.

5.3 Transition from Conventional to MILD Combustion

Figure 5.1 shows the temperature and exhaust gas emissions as a function of time for the baseline case. The dashed vertical line represents the time when MILD combustion was activated, the bluff-body was retracted, and no flame was visible (Figure 5.2). The successful transition between the two regimes is evidenced by the sudden decrease in furnace reference temperature and by the four-fold drop in NO_x emissions. The differences seen in the levels of O_2, and consequently of CO_2, during the transition to the MILD regime were caused by a slight increase in pressure drop in the fuel supply system. However, it is clear that these changes did not significantly influence the measured temperatures. Fine-tuning of the fuel flow rate was typically needed to compensate for small pressure variations in the supply line.

From the time the furnace was switched to the MILD regime, about 1.5 hours were needed to reach steady-state MILD combustion conditions. In steady-state conditions, the temperature difference between the top and the bottom sections of the furnace was around 110°C for the baseline case. The low temperature gradient throughout the furnace is an important characteristic of this combustion regime.

5.4 Furnace Performance Characteristics

5.4.1 Parametric Study

An assessment of the key furnace/burner input parameters was conducted parametrically. The parameters studied were the burner firing rate or fuel input, heat extraction position, heat extraction rate, air inlet temperature, overall equivalence ratio or excess air, fuel nozzle size, and fuel dilution. The parametric study seeks to identify the those parameters that cause significant change in the performance of the combustion system. It is important to clarify that, throughout this thesis, the term heat exchanger position is related to one of the five possible window openings A1−A5 (see Figure 3.1), and the term heat exchanger insertion is related to the exposed area of the heat exchanger, i.e. heat extraction rate (see Figure 3.2).
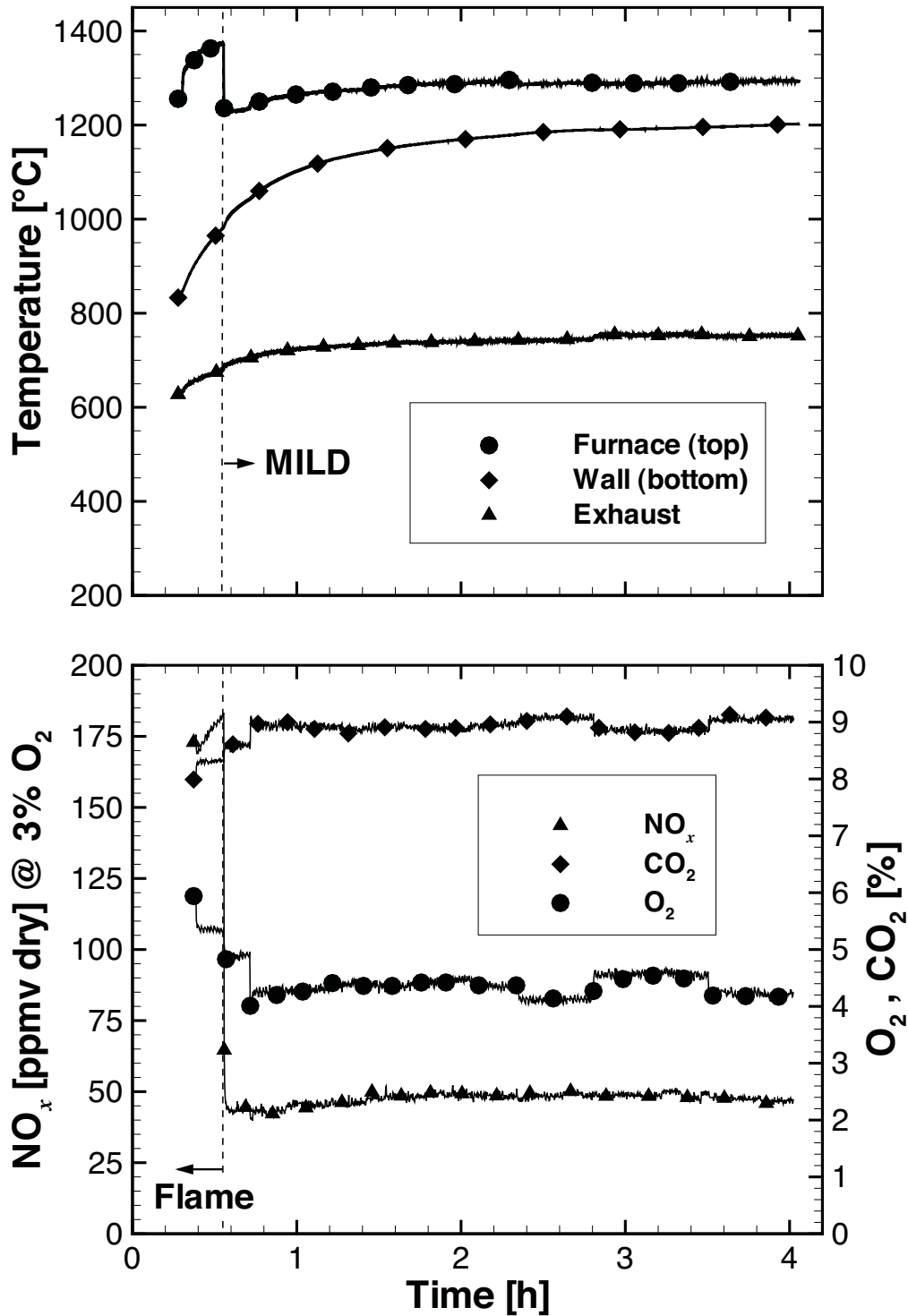
Figure 5.1: Temperature and emissions recorded during the transition from conventional to MILD combustion for the baseline operating conditions ($\varnothing_{id} = 2.0$ mm, $\dot{Q}_{fuel} = 15$ kW NG, $\phi = 0.80$, $T_{air} = 450°$C, 25% insertion at position A3).
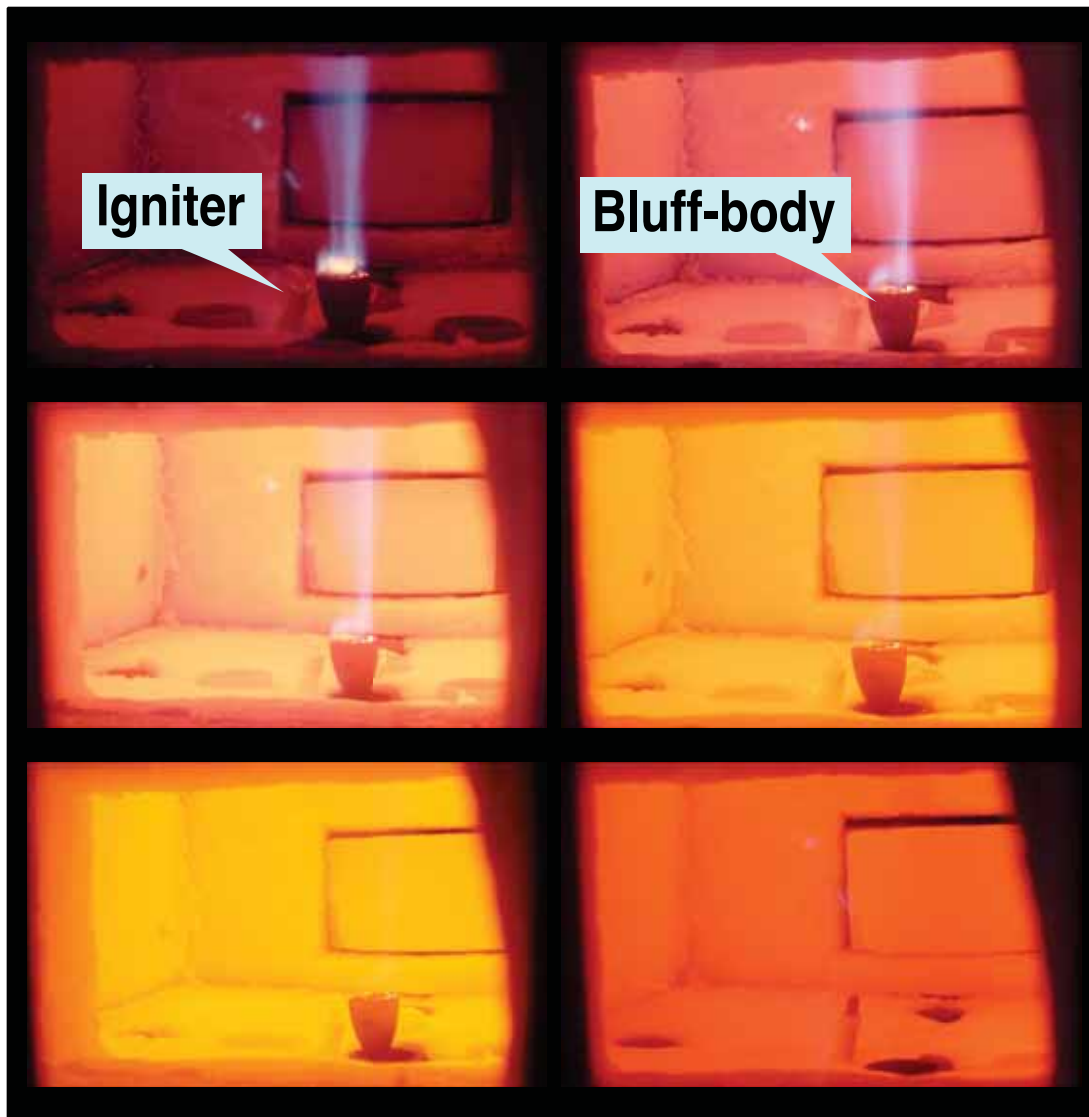
Figure 5.2: Sequence of photographs of the burner exit region from the heat up stage until the MILD combustion mode is activated.

One crucial parameter when examining furnace performance is the nozzle diameter, which characterises the momentum flux of the source jets; $G = \dot{m}u$, where $\dot{m}$ is the mass flow rate, and u is the inlet velocity at the nozzle exit. In confined jet flows the momentum flux (G) provides an indication of the mixing process and recirculation levels [159].

Based on its relevance to combustion aerodynamics, Grandmaison et al. [79] developed the strong-jet/weak-jet (SJWJ) model from simple jet physics by solving equations for a three-feed mixing problem: the strong jet is combustion air, the weak jet is a gaseous fuel, and the ambient fluid consists of recirculating furnace gases. Because of combustion stoichiometry, the air jet momentum is relatively strong, and the fuel jet weak. Their correlations are a function of different nozzle separation angles and momentum flux ratios between the air and fuel jets for a type of MILD burner. In the SJWJ approach, the jet trajectories, the junction point of the incoming jets, the entrainment of combustion products into the air and fuel streams up to the junction point, and the extent of the mixing zone can be determined. These are important features to characterise the performance and stability of the current MILD combustion system.

5.4.2 Effect of thermal input

In most combustion applications, required heat loads constantly vary, which means that the incoming flow rates of air and fuel are adjusted to meet a certain heat transfer condition. Operational constraints on the service temperature often apply, so that the control of pollutants emission, NO_x in particular, and product quality are ensured. Since the firing rate changes, flame stability is usually affected.

Figure 5.3 shows the effect of the turndown ratio on both furnace and wall temperatures, and NO_x emissions. The turndown ratio is defined as the ratio between the nominal capacity of the burner and the minimum firing rate required for stable operation. The thermal input, displayed in the abscissa, is normalised by the furnace volume. It can be readily seen from the plot that the temperature gradient between the top and the bottom sections of the furnace is around 150°C, and the difference remains constant across a turndown ratio of 1:3. The lowest fuel input produces the lowest temperatures and the lowest NO_x emissions.
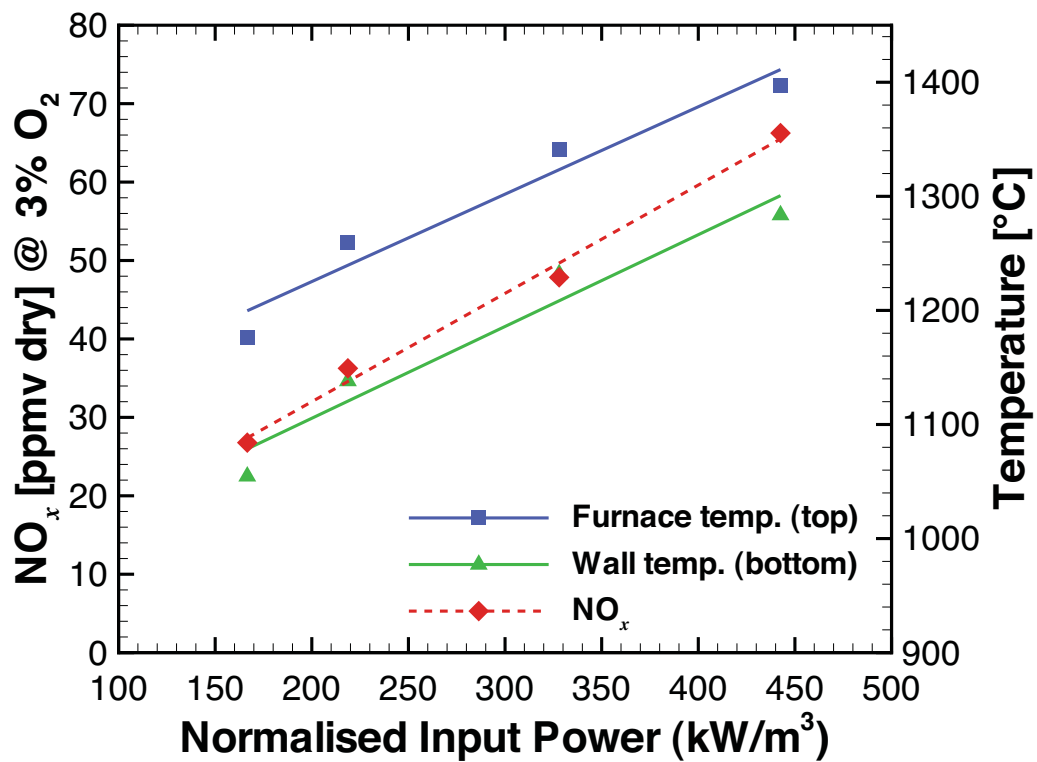
Figure 5.3: Effect of fuel input on temperature and NO_x emissions for the baseline operating conditions ($\varnothing_{id} = 2.0$ mm, $\phi = 0.80$, $T_{air} = 450°C$, 25% insertion at position A3).

5.4.3 Effect of heat extraction

Heat extraction is an important energy output term used to determine the overall thermal efficiency of a furnace. It is also particularly significant on the propagation and stability of MILD combustion due to quenching effects.

Figure 5.4 defines the operating envelope for the MCF by showing the effects of heat extraction on NO_x emissions and furnace temperature for the turndown ratio found in Figure 5.3. Here, and throughout this thesis, the heat extraction load, $\dot{Q}_{hx}$, is expressed as a percentage of the total heat input (refer to equation 3.1). The thermal input was fixed and the exposed area of the heat exchanger was gradually increased. As expected, heat extraction controls the furnace temperature, with decreasing temperatures for increasing heat extraction across all thermal input conditions. Once again, a decrease in furnace temperature leads to a decrease in NO_x emissions.
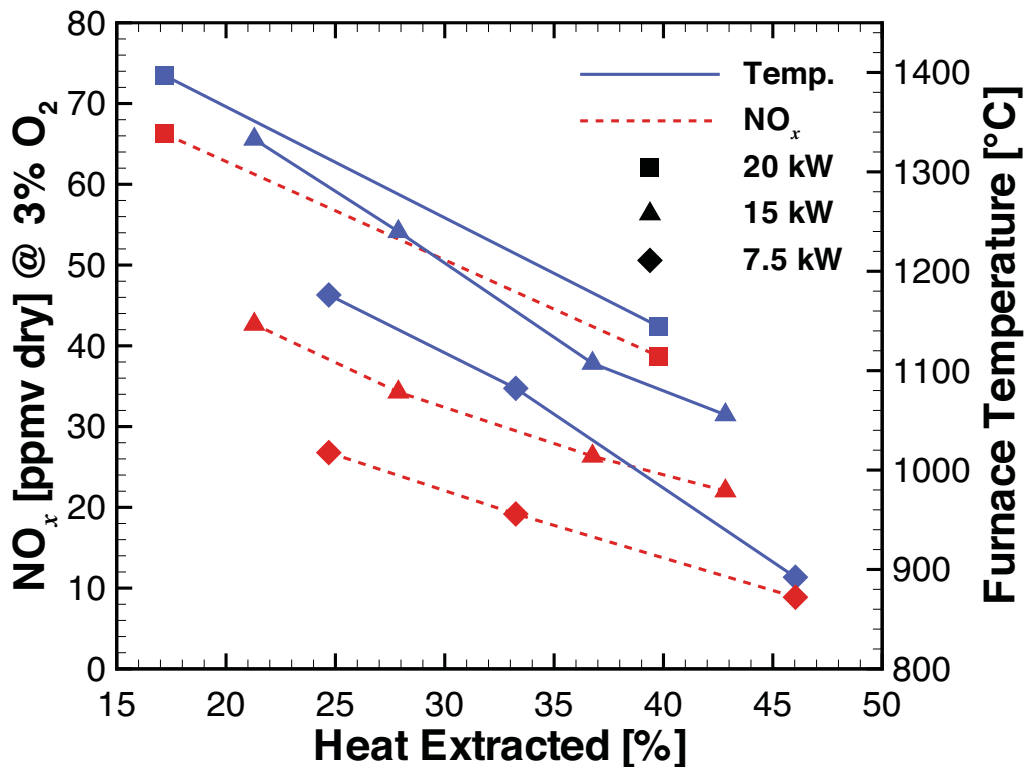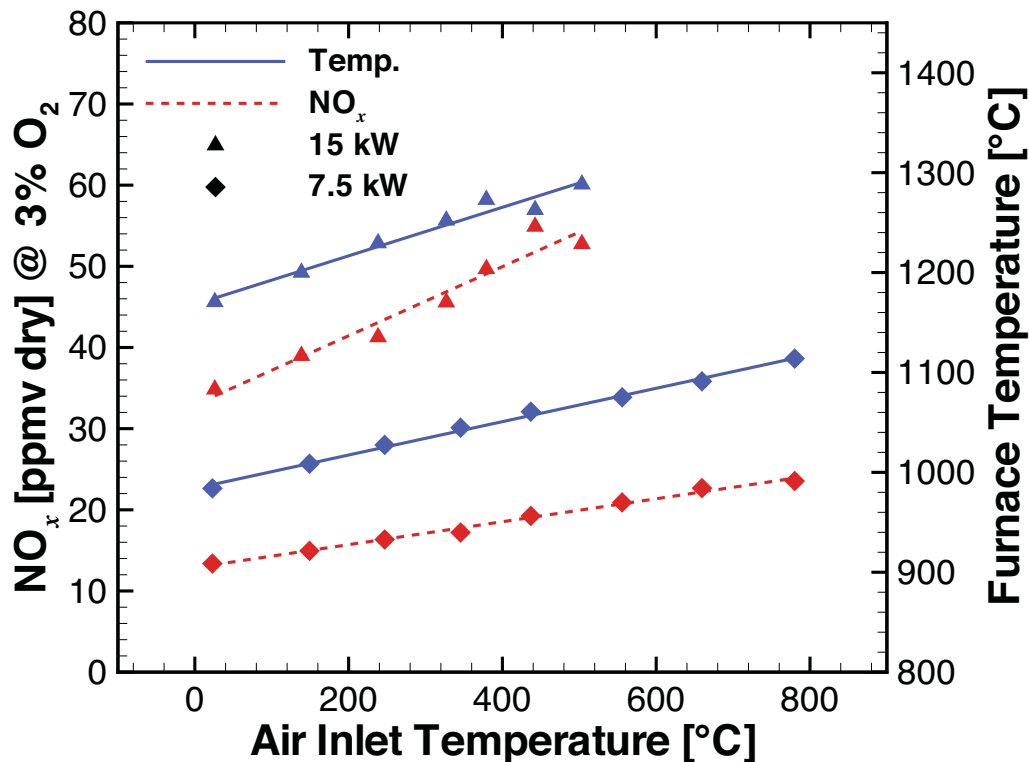

Figure 5.4: Effect of heat extraction on temperature and NO_x emissions for different thermal input conditions ($\varnothing_{id} = 2.0$ mm, $\phi = 0.80$, $T_{air} = 450°C$, heat exchanger at position A3).
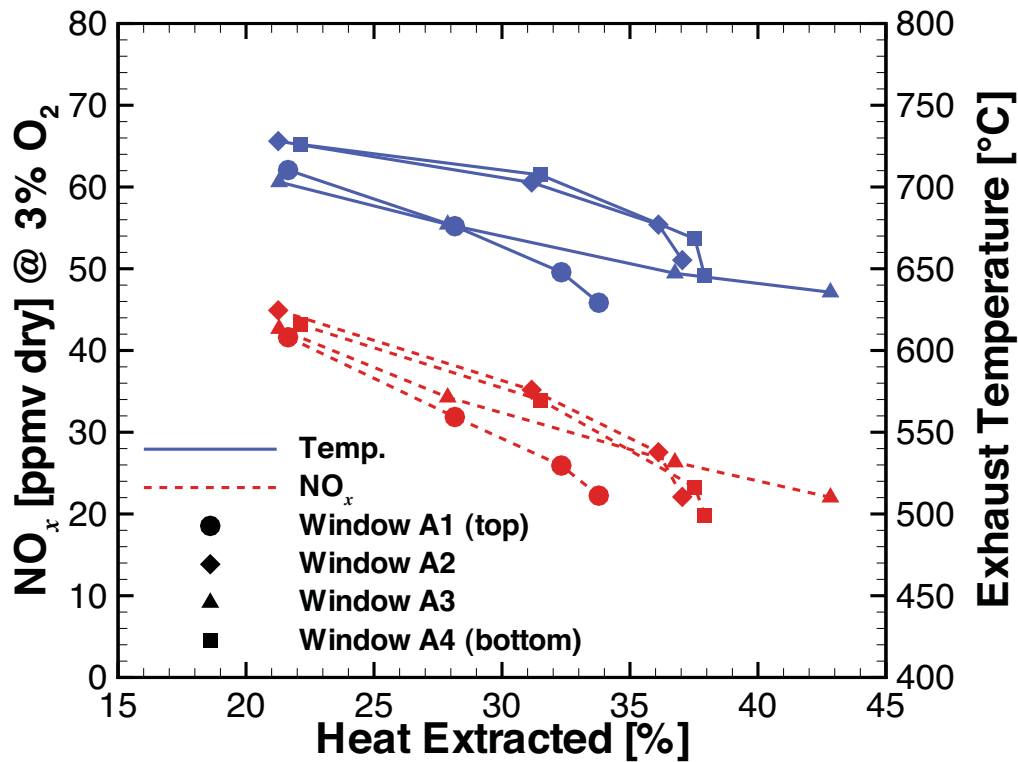
Figure 5.5: Effect of heat extraction on temperature and NO_x emissions for various heat exchanger positions ($\varnothing_{id} = 2.0$ mm, $\dot{Q}_{fuel} = 15$ kW NG, $\phi = 0.80$, $T_{air} = 450°C$)

Figure 5.5 shows the effects of heat extraction and its location on NO_x emissions and furnace temperature for the baseline operating condition. In order to avoid the temperature bias caused by the proximity of the thermocouple to the heat exchanger, the exhaust temperature is used as the characteristic global temperature. Evidently, the location of the heat exchanger does not seem to significantly affect the furnace performance. For a certain level of heat extracted, global temperature and NO_x emissions are practically the same irrespective of the heat exchanger position, respectively differing by $2-4\%$ and $3-13\%$.

5.4.4 Effect of air preheat

To examine the importance of external air preheating on the establishment of MILD combustion, an electrical heater with a nominal capacity of 3.3 kW was conveniently used to vary the air inlet temperature. Figure 5.6 shows the effect

of combustion air temperature on NO_x emissions and furnace temperature for two different thermal inputs. The same trend is observed for both firing rate conditions. As inlet air temperature decreases, NO_x emissions and furnace temperature decrease linearly. However, there is only a 10 ppm change in NO_x levels for a 760°C change in air temperature for the lowest thermal input (7.5 kW), and similarly only a 13 ppm change for a 500°C increase in air preheat for twice as much thermal input (15 kW).

Figure 5.6: Effect of air preheating on temperature and NO_x emissions for different thermal input conditions ($\varnothing_{id} = 2.0$ mm, $\phi = 0.80$, 25% insertion at position A3).

Figure 5.7 shows the effect of heat extraction on NO_x emissions and temperature for the baseline case with and without air preheating. To eliminate the bias caused by thermocouple positioning, the exhaust temperature is used as the characteristic global temperature. Neither the air inlet temperature nor the heat extraction have a strong influence on global temperature or NO_x emissions. The results suggest that external air preheating is not a necessary condition to achieve
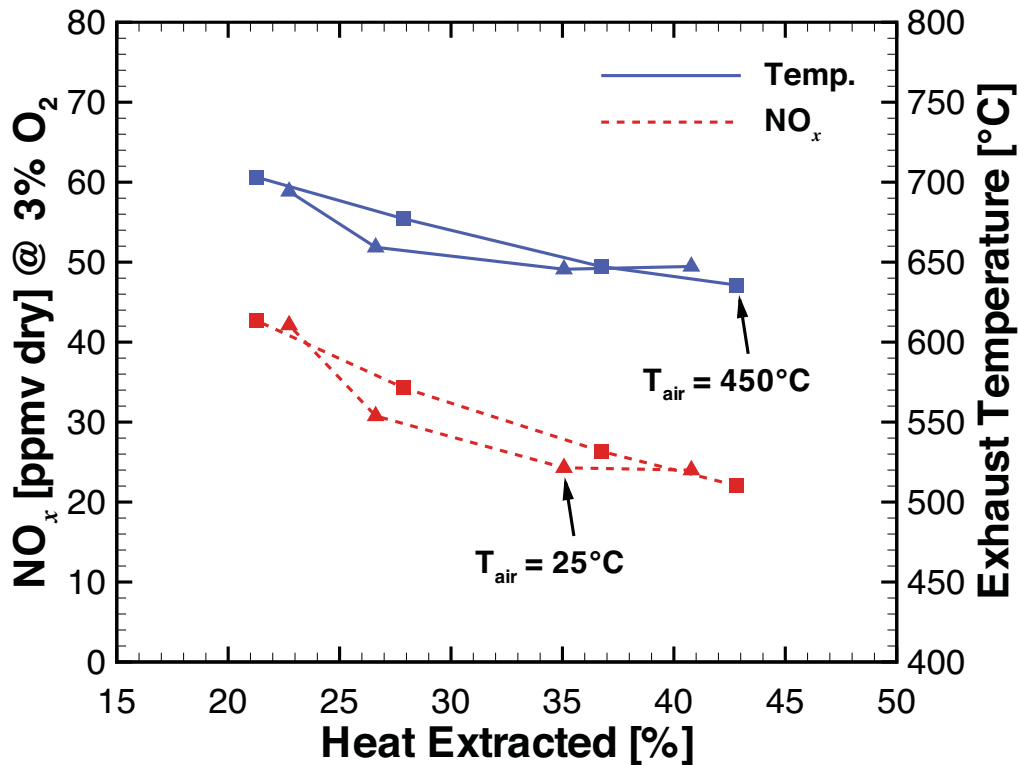
Figure 5.7: Effect of heat extraction on temperature and NO_x emissions for the baseline operating conditions with (squares) and without (triangles) air preheating ($\varnothing_{id}$ = 2.0 mm, $\dot{Q}_{fuel}$ = 15 kW NG, ϕ = 0.80, heat exchanger at position A3).

MILD combustion, even with high levels of heat extraction ($\dot{Q}_{hx} > 40\%$).

5.4.5 Effect of fuel dilution

A high degree of dilution of the reactants is one of the necessary conditions for establishing MILD combustion. An interesting approach to increasing vitiation and delaying the reaction between air and fuel is the addition of an inert gas to the fuel stream. Figure 5.8 shows the effects of fuel dilution on temperature and NO_x emissions for two different fuels and nozzle diameters under the baseline operating conditions. It also shows predictions from a perfectly stirred reactor (PSR) model to assess the influence of chemical kinetics alone on the MCF performance for the NG cases. The fuel stream was diluted using either N_2 or CO_2 and the corresponding diluent mass fraction (Y_{dil}) is displayed in the abscissa. The fuel

and the air mass flow rates were kept constant, while the mass flow rate of diluent was varied. This procedure resulted in changes in the fuel jet inlet velocity and momentum flux.

It is clear from Figure 5.8 that, although dilution can be expected to cool the reaction zone, this effect is small. For each case, up to 76% fuel dilution causes a reduction in furnace temperature of only $2-4\%$, while the decrease in NO_x emissions can be as large as 48%. The figure also shows that the furnace operates at slightly different temperatures in each case, despite the nominal thermal input being held constant. For the same diluent mass fraction, the difference between each operating condition is at most 70°C, but can be as low as 5°C. This small difference does not explain the variations observed in NO_x emissions. Hence, it is evident that fuel type, diluent, and fuel nozzle size have a significant effect on NO_x emissions. Each of these effects is examined in turn below.

First considered are the cases in which only the fuel type was varied, for instance LPG/CO_2 (3 mm) versus NG/CO_2 (3 mm). The general trend observed in the graph is that NO_x emissions from LPG combustion are higher than those from NG. Dally et al. [37] reported similar trends for diluted methane and propane flames.

Next examined are the cases in which the diluent type is varied. In agreement with the results reported by Dally et al. [37] and by Hasegawa and Niioka [85], Figure 5.8 shows that fuel dilution with CO_2 (open symbols) produces lower NO_x emission levels than does the equivalent fuel dilution with N_2 (solid symbols) for the same fuel jet diameter. Further, the CO_2 dilution causes a decrease in NO_x emissions of up to 48% over the operating range, whereas the N_2 dilution causes only about $2-10\%$ reduction, even though the N_2 content inside the furnace increases up to 19% for the highest diluent mass fraction cases ($Y_{dil} > 68\%$). The ratio of the specific heats of CO_2 to that of N_2 is 1.076 at 1280°C. Since the furnace temperature is virtually constant, the differences in specific heats and gas radiation characteristics are deduced to be unable to explain the different behaviors.

Next assessed are the results from the PSR model for the combustion of NG. The use of this model is justified because the furnace aerodynamics, which is controlled by the central air jet (see §7.3), is virtually the same for all dilution cases. The PSR calculations are represented in Figure 5.8 by the red colored lines
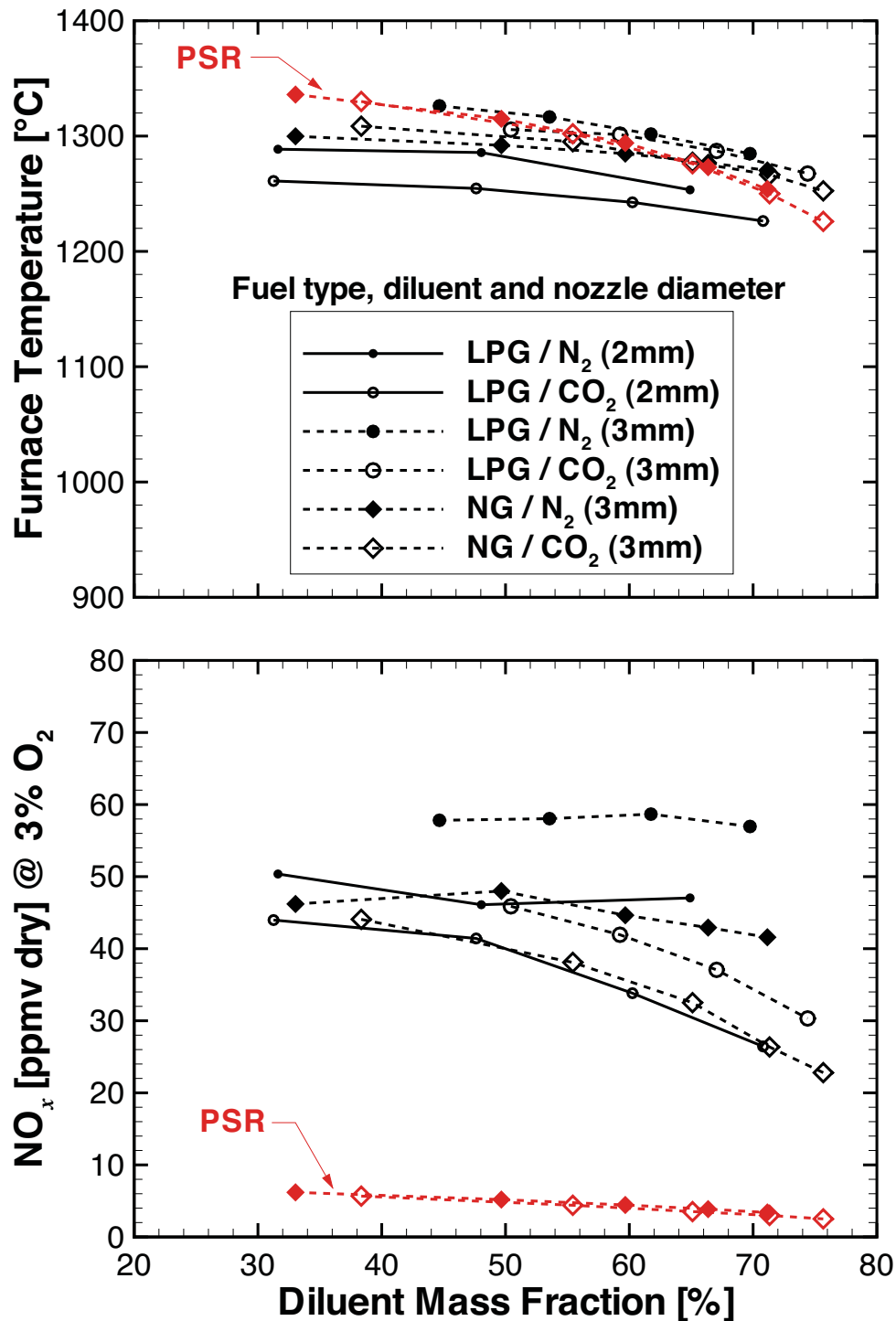
Figure 5.8: Effect of fuel dilution on temperature and NO_x emissions with fuel type and burner size as parameters for the baseline operating conditions ($\dot{Q}_{fuel} = 15$ kW, $\phi = 0.80$, $T_{air} = 450°C$, 25% insertion at position A3). Solid symbols: N_2 dilution, open symbols: CO_2 dilution, solid lines with small symbols: $\varnothing_{id} = 2.0$ mm, and dashed lines with large symbols: $\varnothing_{id} = 3.0$ mm. Red colored lines and symbols represent PSR calculations for methane (GRI 3.0).

and symbols. Refer to §4.3 for details on the inlet conditions. The predictions from the PSR model show the same general trend observed in the measurements of decreasing gas temperature and NO_x emission levels with fuel dilution. However, the maximum predicted NO_x emissions are only 6 ppm for both diluents. A sensitivity analysis (not shown) showed that the recirculation stream has little effect on NO_x formation at 1280°C. It also revealed that the reactor temperature would need to be at least 200°C higher to reproduce the NO_x emission levels observed in the experiments, which is when the thermal-NO mechanism starts to dominate.

Finally, we assess the cases in which the fuel jet diameter is varied. It is noticeable from Figure 5.8 that NO_x emissions increase when the fuel nozzle size is increased. For a constant diluent mass fraction and thermal input from the fuel, an increase in nozzle diameter causes a decrease in the fuel jet velocity by 44% and a decrease in the jet momentum flux by the same amount for the same diluent. A lower fuel jet momentum will reduce the entrainment of hot furnace gases and hence change the mixing characteristics close to the burner exit. In an attempt to confirm this trend, a third fuel nozzle of diameter 4.6 mm was also tested. However, stable MILD combustion could not be sustained for the baseline operating conditions, and a visible flame appeared at all times. A description of the stability characteristics of this multiple jet system is given in §5.5.

5.4.6 Effect of equivalence ratio

Figure 5.9 shows the effects of global equivalence ratio on temperature and emissions for various heat exchanger positions under the baseline operating conditions. This assessment seeks to identify the most suitable position for energy extraction and to assess the influence of this location on the reactions inside the furnace. Both the furnace (solid lines) and exhaust (dashed lines) temperatures are presented. The global equivalence ratio was determined from the knowledge of the inlet flow rates of air and fuel. For each heat exchanger position, the thermal input from the fuel was kept constant and the air mass flow rate was varied. The corresponding emission indices for CO and NO_x are shown in the secondary ordinate. Also displayed are equilibrium calculations (blue coloured line and circles) and predictions from a PSR model (red coloured lines and crosses). As indicated

in §4.3, these calculations are used to evaluate the importance of turbulence-chemistry interactions. However, in this case the emphasis is on CO emissions, and hence the predictions for NO_x are not presented.

It can readily be seen from Figure 5.9 that the heat extraction location does not greatly affect temperatures, CO_2 or NO_x emissions. However, it has a significant effect on CO emissions. The figure shows that the furnace temperature is slightly different in each case. For the same equivalence ratio, the difference between each operating condition is at most 80°C, but can be as small as 7°C. The furnace temperature is more susceptible to bias due to the proximity of the thermocouple to the heat exchanger. The exhaust temperature only changes by 30°C throughout the tested range, indicating that the total heat extracted varied by less than 4% for all heat exchanger positions. The decrease in the exhaust temperature observed at position A3 for $\phi > 0.9$ is due to a slight variation in the water temperature from the supply line, which slightly increased heat extraction for that particular case. It is clear that this change did not significantly influence emissions.

As expected, CO_2 concentrations increase and NO_x emissions decrease towards stoichiometric ($\phi = 1.0$) conditions due to dilution by excess air. Most importantly Figure 5.9 identifies the threshold for the sharp rise in CO emissions, which is as low as $\phi = 0.86$ for one position, and $\phi = 0.89$ for the others. Interestingly, NO_x emissions do not drop dramatically within the same equivalence ratio range, which is in stark contrast to conventional combustion. Rather, the slope is more or less constant with equivalence ratios exhibiting a decrease by about $7-12\%$. Although the general trend for CO emissions is the same for all heat exchanger positions, significant differences are apparent. Perhaps surprisingly, the lowest threshold occurs with the heat exchanger at the second to lowest position (window A3), rather than at the lowest (window A4), and the highest overall emissions occur with the heat exchanger at the top of the furnace (window A1). It is worth noting that unburned hydrocarbons (UHC) were either below the detection limit of 100 ppm or below the minimum O_2 concentration ($\approx 2\%$) for a reliable measurement.

The PSR model captures the trend of increasing furnace temperature with equivalence ratio. In contrast to the experiments, the predictions show a more gradual rise in CO emissions. Only a tripling of the CO levels is observed with a
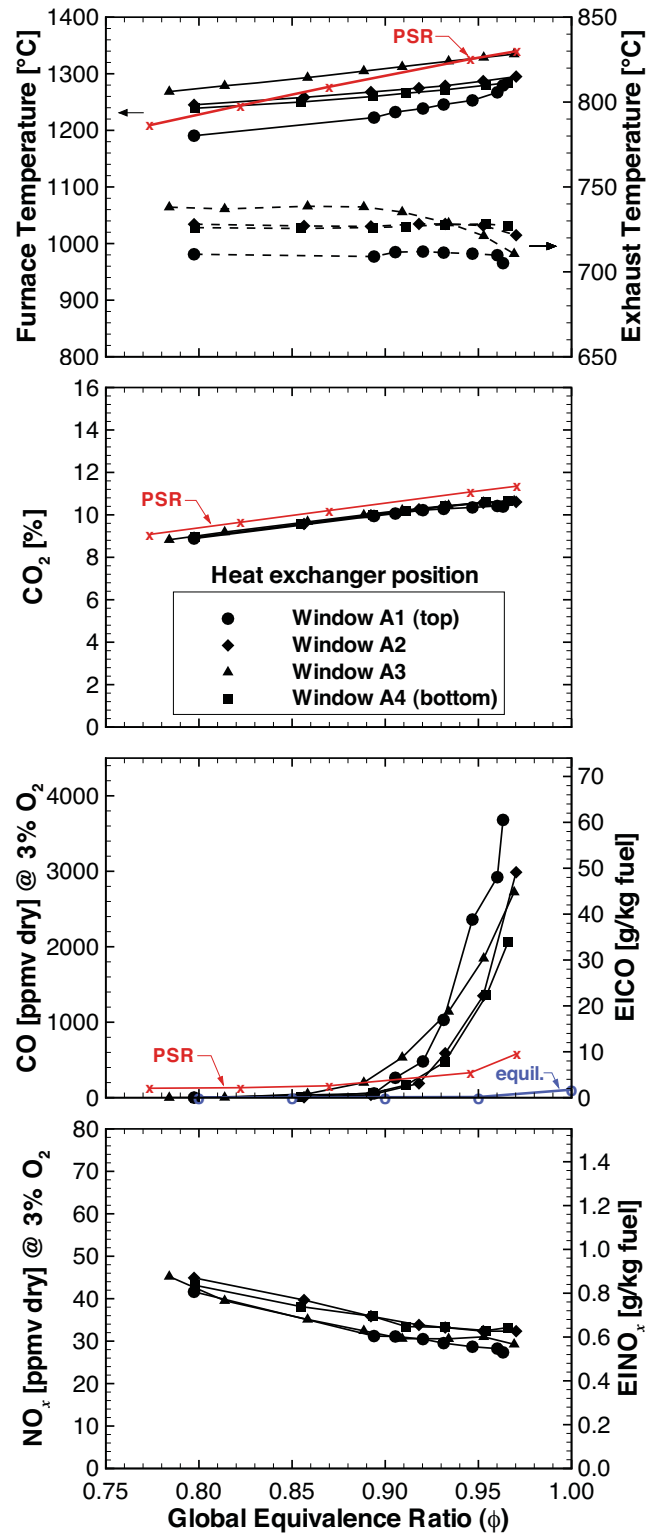
Figure 5.9: Effect of equivalence ratio (ϕ) on temperature, CO_2, CO and NO_x emissions with heat exchanger position as the parameter, for the baseline operating conditions ($\varnothing_{id} = 2.0$ mm, $\dot{Q}_{fuel} = 15$ kW NG, $T_{air} = 450$°C, 25% insertion at position A3).

maximum $3-6$ times lower than in the measurements in a range of $0.89 \leq \phi \leq 0.97$. The calculated CO_2 levels agree well with the experiments. The equilibrium values for CO are notably lower than in the experiments. This difference is likely to be a consequence of the strong interaction between turbulence and kinetics.

5.4.7 Optimisation tests

Optimisation of the equivalence ratio is common practice for avoiding excessive exhaust gas losses, and keeping emissions to a minimum. Figures 5.10 and 5.11 show respectively the effect of inlet air temperature and heat extraction on NO_x emissions and furnace temperature for two different equivalence ratios. In the first case the burner was operated with about 25% excess air ($\phi = 0.80$) and in the second case with about 10% excess air ($\phi = 0.90$). The latter condition was chosen based on the critical threshold found in Figure 5.9, which provided CO levels below 100 ppm throughout the experiments.

The same trend is observed for both equivalence ratio conditions in Figure 5.10. As combustion air temperature decreases, the NO_x emissions and furnace temperature decrease linearly. However, the influence of air preheating on global temperature and NO_x emissions is not so strong, despite the 63% reduction in air jet momentum. For each case, the furnace temperature varies about 9% and NO_x emissions $18-34\%$, despite the 500°C change in air temperature. NO_x emission levels for $\phi = 0.90$ are $9-28\%$ lower than for $\phi = 0.80$ across the air temperature range. These lower levels for $\phi = 0.90$ are in agreement with the results from Figure 5.9.

As expected from Figure 5.11, an increase in heat extraction, which conversely means a decrease in furnace temperature, leads to a decrease in NO_x emissions of up to 50%. The figure also shows that the furnace operates at practically the same temperatures in each case. Once again NO_x emission levels for $\phi = 0.90$ are lower than for $\phi = 0.80$. Noteworthy too, NO_x emissions were reduced by 42%, in relation to the higher excess air case, for a 38% heat extraction condition typical of that employed in some industrial processes, under no penalty of increased CO emissions. Consequently, $\phi = 0.90$ can be considered to be the optimal equivalence ratio needed to minimise NO_x emissions, while ensuring stable MILD combustion for the current furnace/burner arrangement.
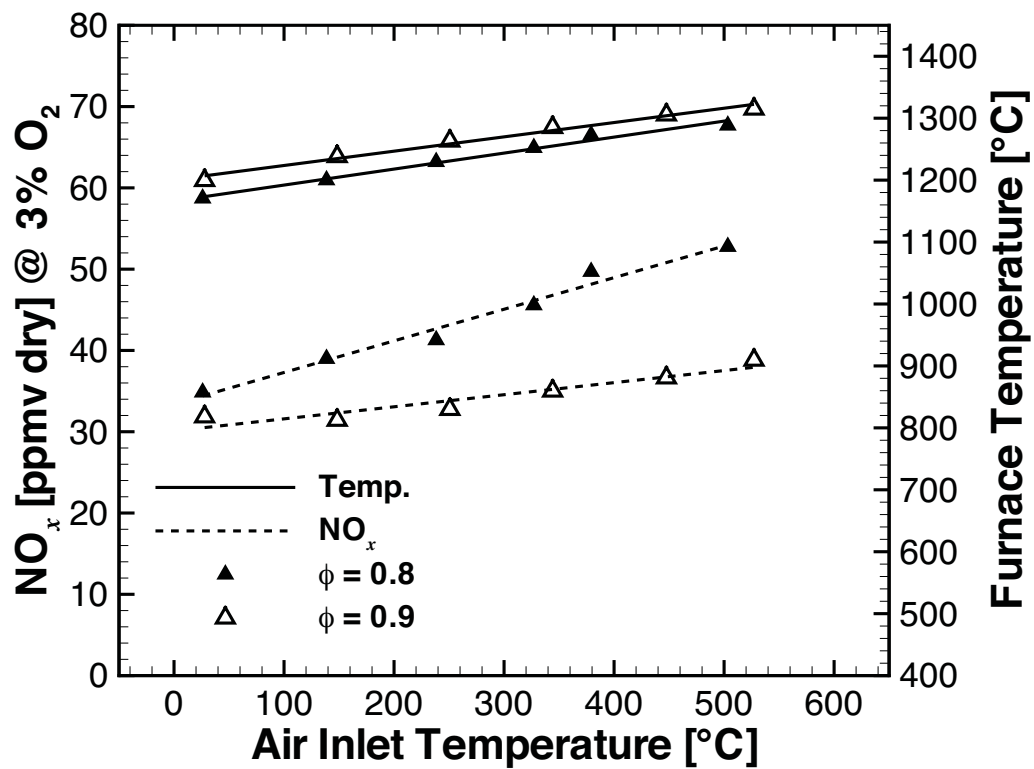
Figure 5.10: Effect of air preheating on NO_x emissions and furnace temperature for two different equivalence ratios for the baseline operating conditions ($\varnothing_{id}$ = 2.0 mm, $\dot{Q}_{fuel}$ = 15 kW NG, 25% insertion at position A3).
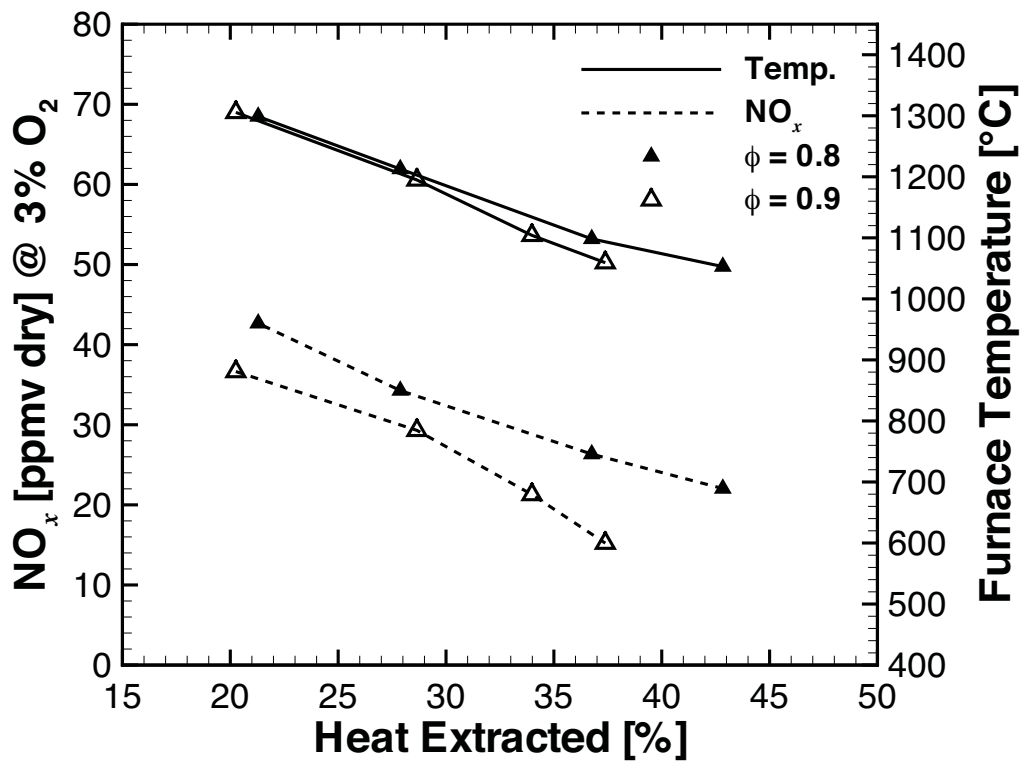
Figure 5.11: Effect of heat extraction on NO_x emissions and furnace temperature for two different equivalence ratios for the baseline operating conditions ($\varnothing_{id} = 2.0$ mm, $\dot{Q}_{fuel} = 15$ kW NG, $T_{air} = 450°C$, heat exchanger at position A3).

5.5 Burner Stability Characteristics

5.5.1 Visual observations

To investigate the stability characteristics of this multiple jet system, the fuel dilution data from Figure 5.8 is used. In this study, the definition of stable MILD combustion is based on the simultaneous requirements of no visible flame and NO_x emission levels below 70 ppm throughout the experiment. Figures 5.12 and 5.13 present a sequence of photographs of the burner exit region (window position A5 or B5) for increasing N_2 and CO_2 dilution with the $\varnothing_{id} = 3.0$ mm fuel nozzle for NG and LPG, respectively. These instantaneous images were extracted from a video recording at 25 frames per second with a conventional color digital camera at a constant exposure. Each row of a column shows three selected images for each dilution condition. The fuel and the air mass flow rates were kept constant for all cases.

It is evident from Figures 5.12 and 5.13, that a luminous (i.e. soot containing), unstable flame is present for both undiluted cases. These flames are not attached to the burner and exhibit a strong recirculating motion. As the diluent mass fraction is increased the flame becomes patchy (dashed circles in Figures 5.12c, 5.12d, 5.13e and 5.13f) and less luminous until it is no longer visible (Figures 5.12e, 5.12f, 5.13g and 5.13h). Based on visual appearance, the latter condition can be considered to be in the stable MILD or flameless regime. Because of the difference in fuel properties (notably density, but possibly also sooting propensity), more N_2 (by mass) is needed for the case of LPG combustion to achieve the same visual outcome. It is worth noting that N_2 is known to inhibit the growth of Polycyclic Aromatic Hydrocarbons (PAH) [55, 101].

5.5.2 Stability limits

In this subsection, a stability map is drawn from the results presented earlier to define the most suitable operating conditions for the MCF.

Figure 5.14 presents three diagrams related to the stability limits of the parallel jet burner system. Part (a) presents temperature as a function of diluent mass fraction, part (b) the NO_x emissions as a function of jet momentum, and part (c) the axial distance from the burner exit to the point of interaction, or junction,
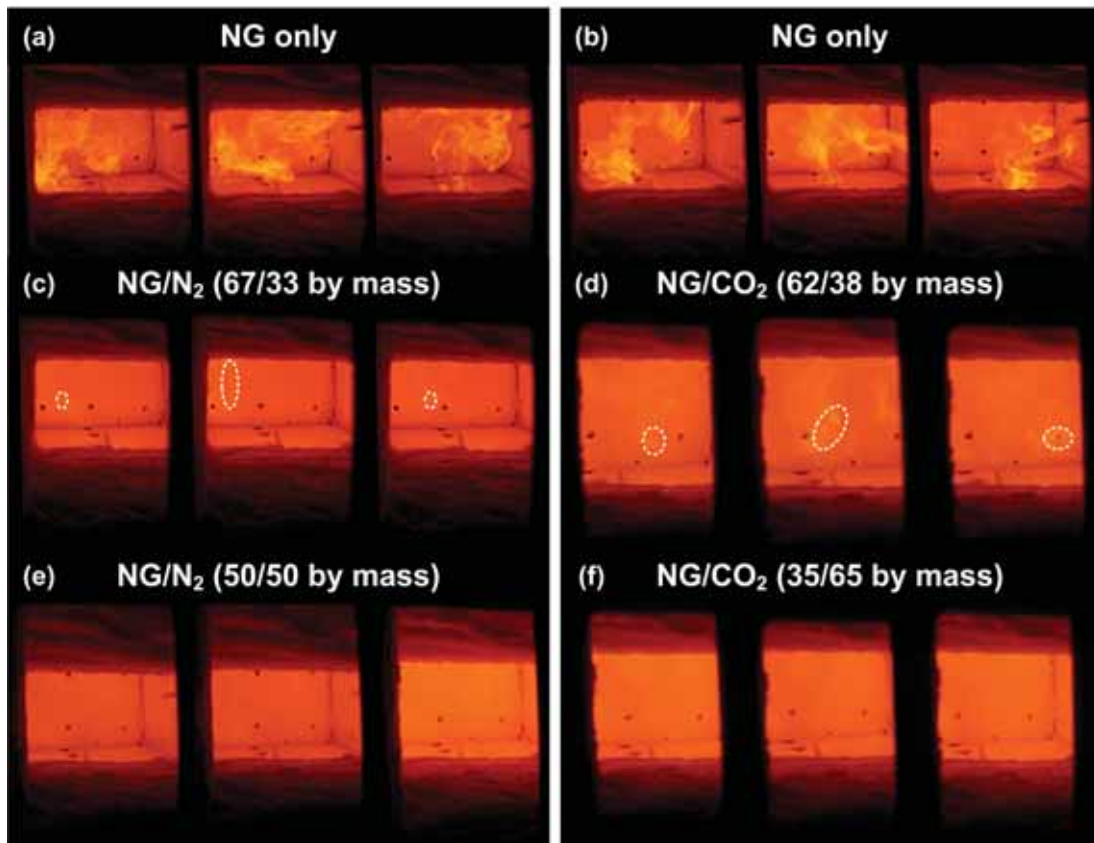
Figure 5.12: Sequence of instantaneous images of NG combustion with increasing N_2 and CO_2 dilution ($\varnothing_{id} = 3.0$ mm,). The dashed circles represent regions of visible flame.
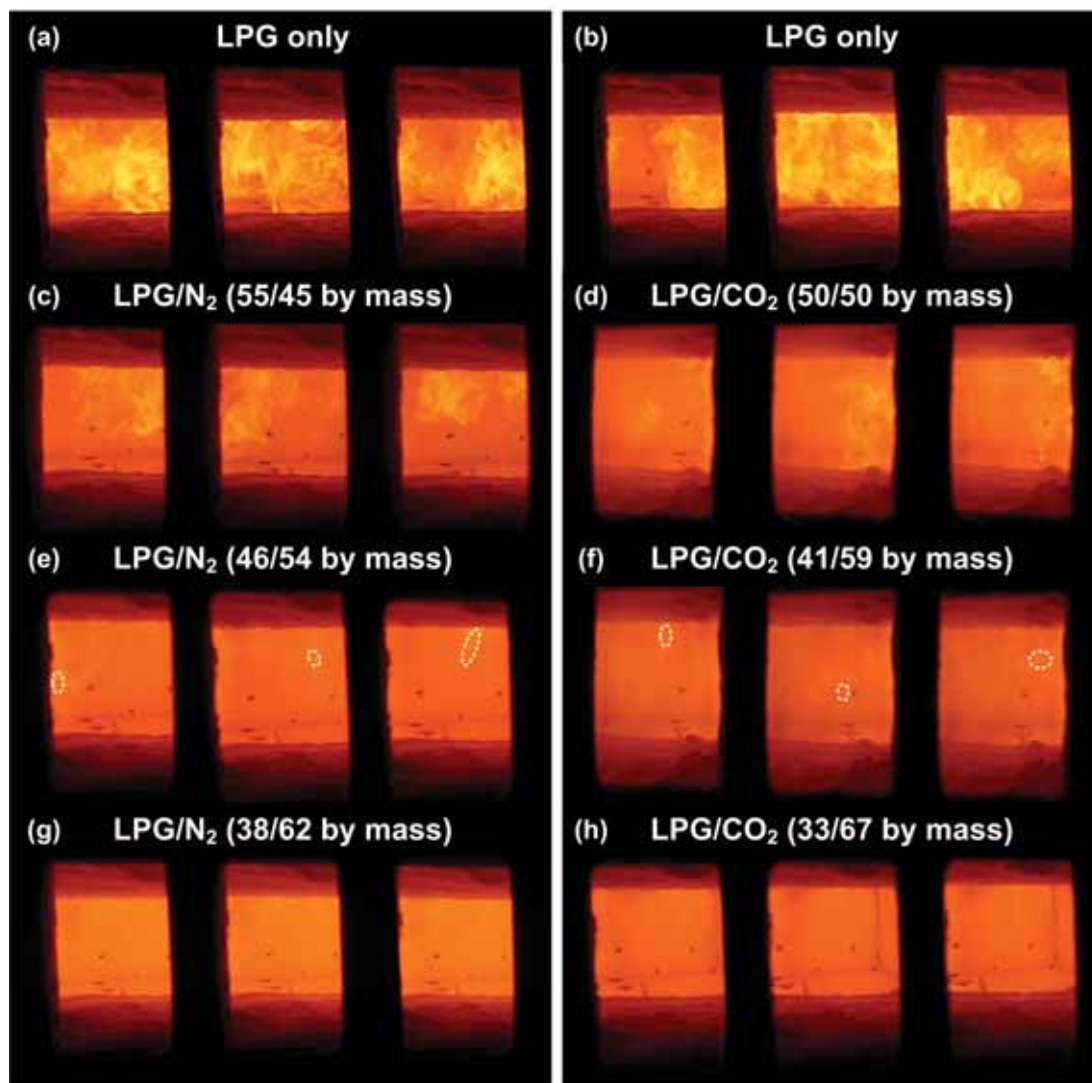
Figure 5.13: Sequence of instantaneous images of LPG combustion with increasing N_2 and CO_2 dilution ($\varnothing_{id} = 3.0$ mm,). The dashed circles represent regions of visible flame.

between the air and fuel jets (z_J) as a function of jet momentum ratio. Here, z_J was calculated from the SJWJ model [79] mentioned earlier in §5.4.1 for the appropriate conditions for the present parallel jet system, i.e. 0° port separation angle. In all figures, the experimental data points are sorted according to fuel type, diluent and fuel jet diameter. The red square and green triangle symbols shown in parts (b) and (c) represent the stable preheated and nonpreheated conditions investigated in Figure 5.7.

The fuel jet penetration distance is an important parameter for the establishment of the MILD regime because it is directly related to the entrainment of combustion products into the fuel and air streams before the mixture reacts, and hence stability characteristics of the present burner.

It is notable from Figure 5.14 that the threshold for stable operation occurs around $G_{fuel} \approx 0.001$ N (part b) at a fuel input of 15 kW. This in turn can be directly related to $G_{fuel}/G_{air} \approx 0.006$ with a minimum penetration distance of $z_J = 260$ mm (part c). Here $G_{fuel}/G_{air} = \dot{m}_{fuel}u/n\dot{m}_{air}U$, where $\dot{m}_{air}$ is the air mass flow rate, $\dot{m}_{fuel}$ is the fuel mass flow rate, u is the fuel inlet velocity for a single nozzle, U is the air inlet velocity, and n is the number of fuel nozzles. It is not surprising that both undiluted cases for the 2 mm fuel nozzle with and without air preheat fall above the stability limit threshold.

The cases with $z_J < 230$ mm correspond to a bright visible flame, consistent with lower dilution prior to the merging of the fuel and air jets. A further increase in the fuel momentum causes a patchy appearance in the flame. This transitional stage ($230 < z_J < 260$ mm) is evident in Figure 5.14c. With sufficient fuel jet momentum, $z_J > 260$ mm, stable MILD operation is ensured.

A maximum momentum threshold for this burner system could be defined as the maximum allowable penetration distance that simultaneously prevents fuel jet impingement on the top and side walls and incomplete combustion (high levels of CO). It is also noted that CO and UHC were below the detection threshold under the conditions reported here, even with unstable conditions. However, as previously shown in Figure 5.9, they do occur with lower excess air (higher ϕ).
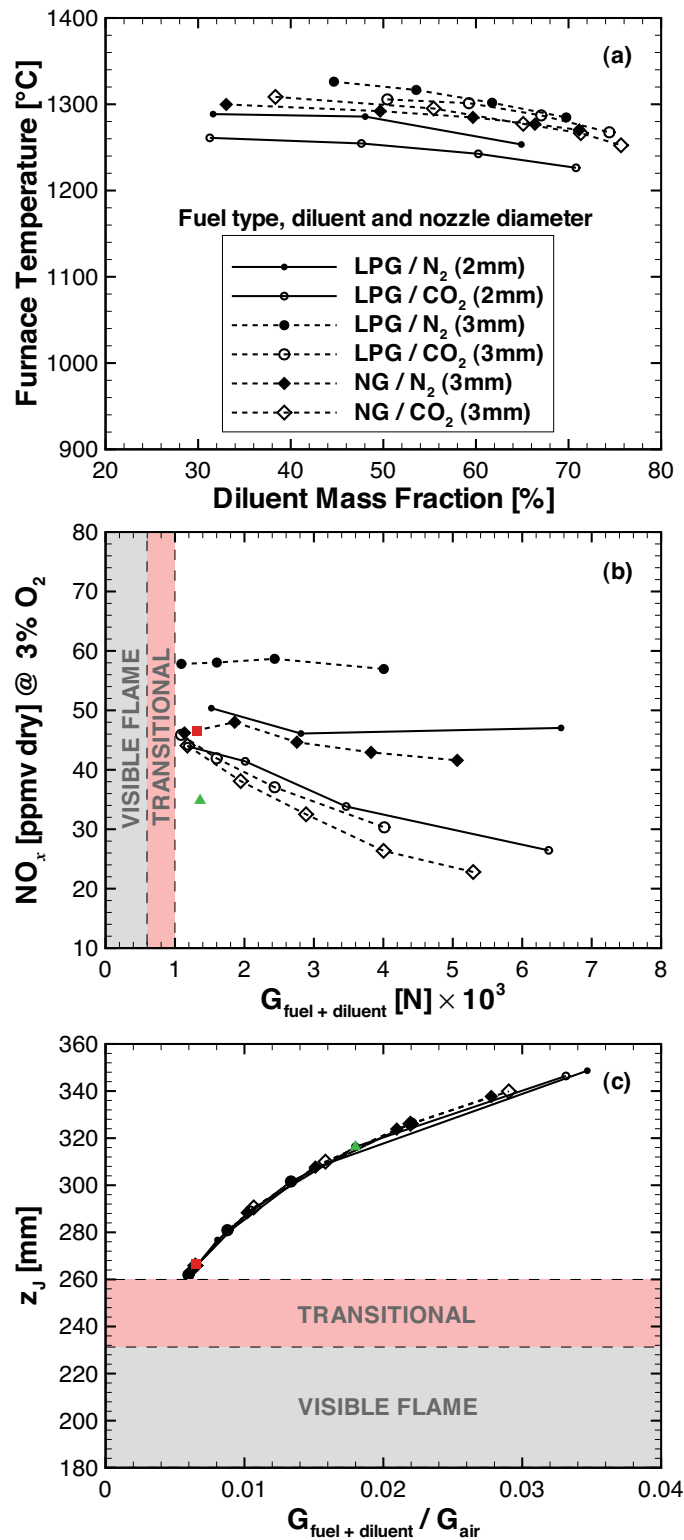
Figure 5.14: Global measurements of (a) temperature, and (b) NO_x emissions for the fuel dilution data; and (c) the axial distance to the junction point calculated from the SJWJ model [79]. Square: baseline case with air preheat, and triangle: baseline case without air preheat, as in Figure 5.7.

5.6 Summary

In this chapter the performance and stability characteristics of a parallel jet MILD combustion burner system in a laboratory-scale furnace is presented. This was achieved through the measurements of global temperature and emissions for a range of thermal input, heat extraction, air preheat, equivalence ratio, and fuel dilution levels. Visual observations were used in combination with the fuel dilution data to produce a stability diagram that shows the threshold for stable operation of this system.

The results demonstrated that the present furnace/burner configuration, in which the reactants and exhaust ports are all mounted on the same wall, is able to sustain stable MILD combustion whilst maintaining relatively high modulation ratios. Also importantly, the investigation identified cases in which the MILD regime was established without external air preheat. These operational characteristics offer the potential for the implementation of the MILD combustion technology in other heat and power systems.

It was found that fuel dilution of up to 76% by mass, with either CO_2 or N_2, reduced NO_x emissions by up to 48% and 10%, respectively. These levels of dilution did not affect furnace temperatures significantly, with a maximum reduction of only 56°C. The critical equivalence ratio, or excess air level, above which there is a steep rise in CO emissions was found to be $\phi = 0.86$ for window position A3, and $\phi = 0.89$ for the other positions of the cooling loop. In stark contrast to conventional flames, a strong decrease in NO_x emissions with flue O_2 levels within a range of $0.89 \leq \phi \leq 0.97$ was not observed, with a maximum variation of only 5%. NO_x levels as low as 14 ppmv dry at 3% O_2 were recorded for an optimum operating condition with 10% excess air ($\phi = 0.90$), in which CO levels were kept below 100 ppm and 38% of the total heat input was extracted.

For the present investigation, the fuel jet momentum was found to control the stability of this multiple jet system. The lower limit for stable operation at a fuel input of 15 kW was found to be $G_{fuel}/G_{air} \approx 0.006$. This is supported by qualitative observations of the burner exit region, and corresponds to a minimum jet penetration distance of 260 mm. This finding is not explained by previous stability criteria, such as the Wünning and Wünning [199] recirculation rate parameter, K_V.

In conclusion, the key controlling parameters that seemed to significantly affect the performance of the furnace were the equivalence ratio, heat extraction rate and the air-to-fuel momentum ratio. However, only a more detailed analysis can reveal which of the effects dominate global NO_x yields. Therefore, the following chapter is entirely devoted to examining the scaling of NO_x emissions from the MILD combustion furnace.

Chapter 6 Scaling of NO$_x$

6.1 Introduction

Understanding of NO$_x$ formation in combustion systems has developed from experimental and numerical studies of unconfined turbulent jet diffusion flames [183], and enclosed furnace environments with conventional combustion systems [90]. In those studies the scaling of NO$_x$ emissions has been widely discussed. However, as indicated in §2.1.1, the results of NO$_x$ scaling relations have not been previously reported for the MILD regime, neither in enclosed nor in open flame systems. In this chapter the comprehensive data set described in §5.2, which covers a variety of operating conditions, is used to investigate the scaling of NO$_x$ emissions with relevant global parameters. Several existing NO$_x$ scaling methodologies, developed for conventional combustion, are applied to the conditions encountered in this MILD combustion furnace. Among the methods tested are: global NO$_x$ emission correlations, Froude number scaling and temperature-time scaling. This approach aims to advance the understanding of NO$_x$ formation in complex recirculating flows with low oxygen concentrations at moderate temperature ranges, typically found in MILD conditions.

6.2 Global Nitrogen Oxides Emission Correlations

In Figure 6.1 the NO$_x$ emissions is presented as a function of the furnace reference temperature (see Figure 3.1). The experimental data points are sorted according to fuel type, diluent and fuel jet size. The solid line represents a linear fit to all of the data. Although there is a general trend of increasing NO$_x$ emissions with furnace temperature, the wide scatter and low correlation coefficient ($R^2 = 0.50$)
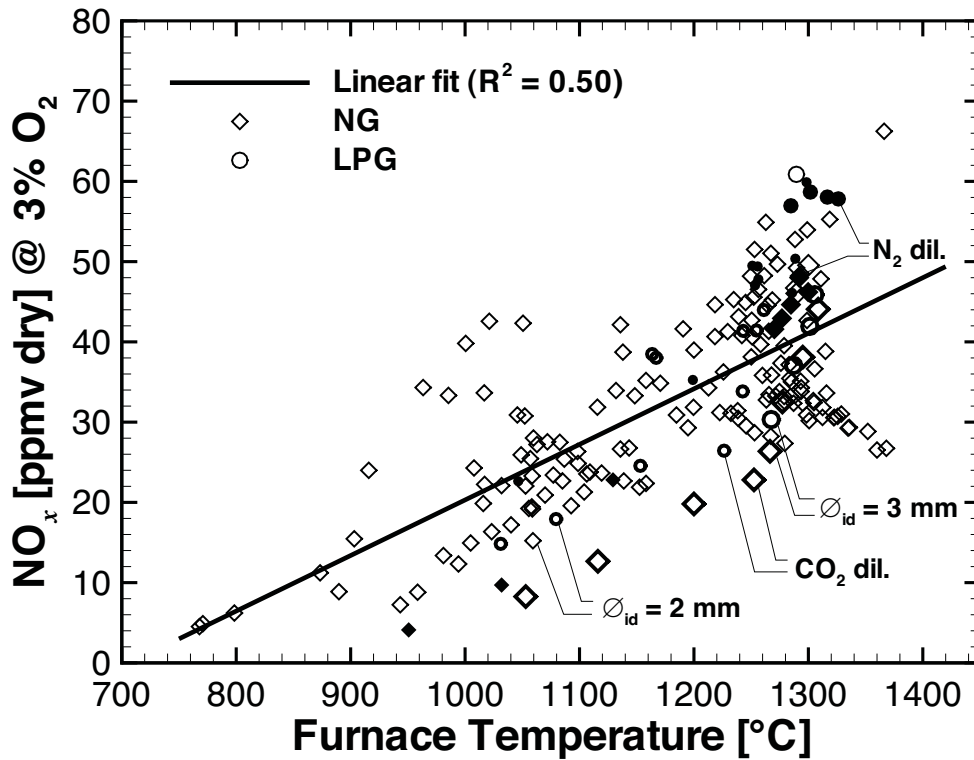
Figure 6.1: Relationship between NO$_x$ emissions and furnace temperature, $T_{furnace}$, for all tested operating conditions. The solid line represents a linear curve fit for all data. The experimental data points are sorted according to fuel type, diluent and burner size. Diamonds: NG, circles: LPG, thin line symbols: no fuel dilution, solid symbols: N$_2$ dilution, thick line symbols: CO$_2$ dilution, small symbols: $\varnothing_{id} = 2.0$ mm, and large symbols: $\varnothing_{id} = 3.0$ mm.

shows that the dependence is weak. It is worth highlighting that very low NO$_x$ levels <10 ppm are achieved for furnace temperatures below 900°C. However, at temperatures of around 1400°C, NO$_x$ emissions exceeding 60 ppm were measured in the MILD regime.

Figure 6.2 shows NO$_x$ emissions data plotted against the exhaust temperature which, while lower than the furnace temperature, avoids the bias in some data due to the location of the cooling loop relative to the thermocouple. It can be seen that there is a stronger influence of temperature for all data ($R^2 = 0.56$) and for individual fuel input ranges. Even though this general correlation is somewhat stronger, it is sufficiently poor to demonstrate that other parameters are also important. This result shows that a representative furnace temperature
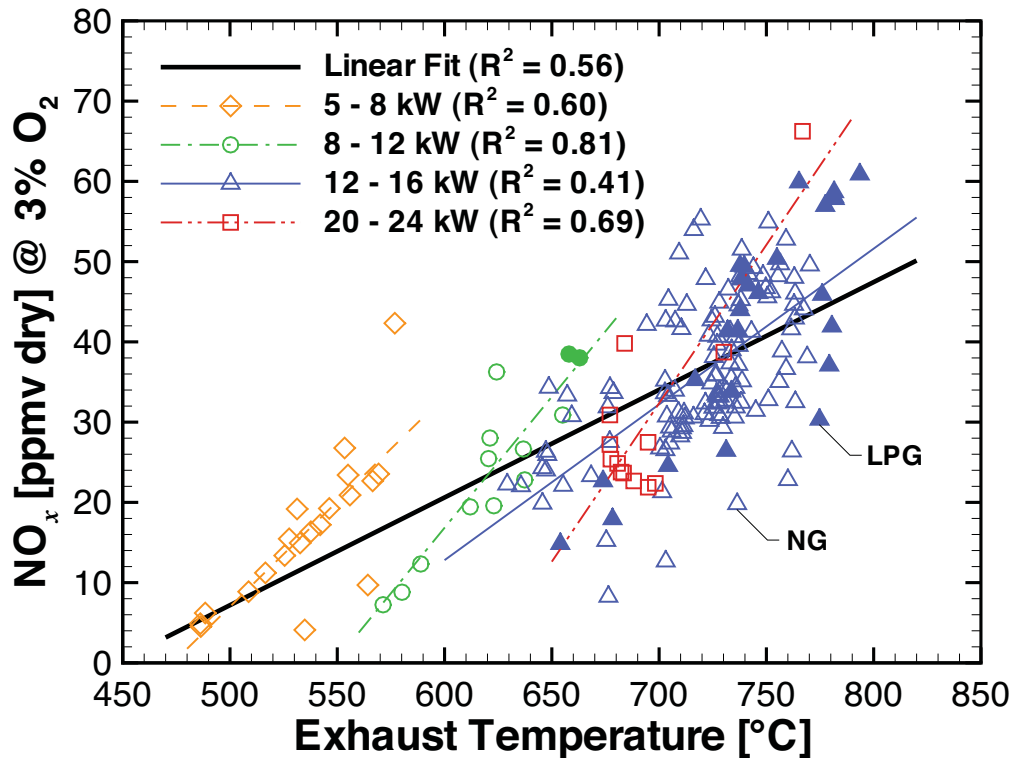
Figure 6.2: Relationship between NO$_x$ emissions and exhaust temperature, $T_{exhaust}$, for all tested operating conditions. The experimental data points are grouped according to fuel input power and fuel type. No distinction is made with respect to fuel dilution and burner size. The thick solid black line represents a linear curve fit for all data. The other thin coloured lines are linear curve fits for each fuel input power bin. Open symbols: all cases burning NG, and solid symbols: all cases burning LPG.

alone does not adequately scale NO$_x$ emissions.

Figure 6.3 shows NO$_x$ emissions plotted against heat extraction. As expected, an increase in heat extraction, which conversely means a decrease in temperature, leads to a decrease in NO$_x$ emissions. Because the heat extraction is only part of the net heat output (refer to equation 3.1), it is not surprising that the correlation with heat extraction is even weaker ($R^2 = 0.39$) than in Figure 6.2.

There is no visible correlation with fuel type, diluent and fuel jet size, neither in Figure 6.1 nor in Figure 6.3. No clear trend is found in Figure 6.2 with regard to fuel type either.
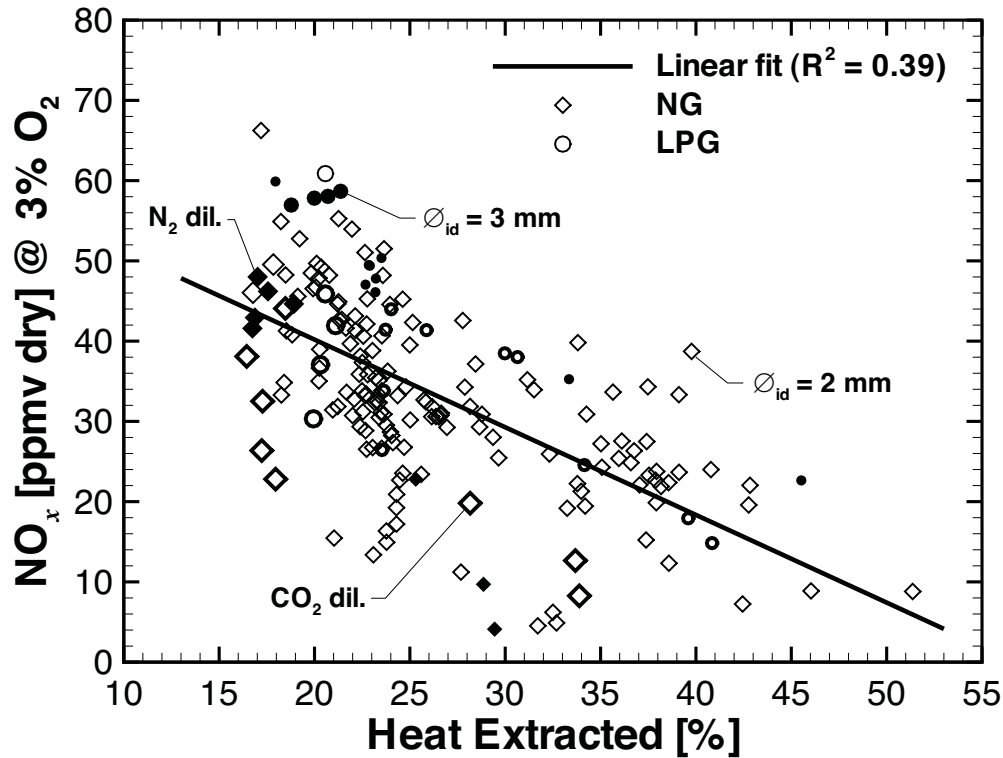
Figure 6.3: Relationship between NO$_x$ emissions and heat extracted, $\dot{Q}_{hx}$, for all tested operating conditions. The solid line represents a linear curve fit for all data. The experimental data points are sorted according to fuel type, diluent and burner size. Diamonds: NG, circles: LPG, thin line symbols: no fuel dilution, solid symbols: N$_2$ dilution, thick line symbols: CO$_2$ dilution, small symbols: $\varnothing_{id} = 2.0$ mm, and large symbols: $\varnothing_{id} = 3.0$ mm.

6.3 Froude Number Scaling

To further investigate the parameters controlling NO$_x$ yields, the leading-order scaling approach of Røkke et al. [161] is explored, despite its limitations [183]. Although developed for buoyancy-controlled hydrocarbon diffusion flames, it has been applied more broadly in the past [6, 191]. Based on a simplified finite-rate chemistry that specifically includes thermal and prompt NO formation, on the concept of laminar flamelet structure [151] and other several assumptions, the authors derived a correlation to predict the NO$_x$ emission index, EINO$_x$. In their scaling of open flames, the flame volume is the leading-order term, and the simple correlation was found to be equal to EINO$_x$ $(\rho_{fuel}u/d) \approx 44\mathrm{Fr}_{\mathrm{e}}^{0.6}$, where Fr$_{\mathrm{e}}$ is the jet exit Froude number. Weber [191] proposed an extension of Røkke's relationship to account for heat extraction in furnace conditions for the Scaling 400 burner series operating with conventional natural gas flames. He varied the proportionality constant according to the levels of heat extraction, whilst conforming to the same slope of 0.6. For example, the scaling correlation was changed to EINO$_x$ $(\rho_{fuel}u/d) \approx 23.2\mathrm{Fr}_{\mathrm{e}}^{0.6}$ for 40% heat extraction. Weber's approach resulted in a series of parallel lines.

Figure 6.4 shows a log-log graph of the variation of EINO$_x$ $(\rho_{fuel}u/d)$, with fuel jet exit Froude number. Part (a) presents all experimental data, part (b) those cases burning NG, and part (c) those cases burning LPG. In all figures, the experimental data points are sorted according to fuel type, diluent and burner size. The theoretical correlation of Røkke et al. [161] and the empirical curve fit for 40% heat extraction from previous work by Weber [191] are also displayed. The fuel jet exit Froude number (Fr$_{\mathrm{e}}$) is the ratio of jet momentum flux to buoyant forces and is calculated from u^2/gd, where g is the gravitational acceleration.

From part (a), it is evident that some data depart from the correlation for the present study (NG + LPG) by almost an order of magnitude. Indeed, several data sets are essentially independent of the Froude number, indicating that other parameters affect NO$_x$ emissions and the role of buoyancy is negligible. This is consistent with the Froude number exceeding unity by three orders of magnitude (Fr$_{\mathrm{e}} > 10^3$), which suggests a momentum-controlled system. Even those data subsets that do scale with Fr$_{\mathrm{e}}$, such as the correlation (NG reference) represented in blue in part (b), exhibit a slightly different slope ($\propto$ Fr$_{\mathrm{e}}^{0.68}$) to those found
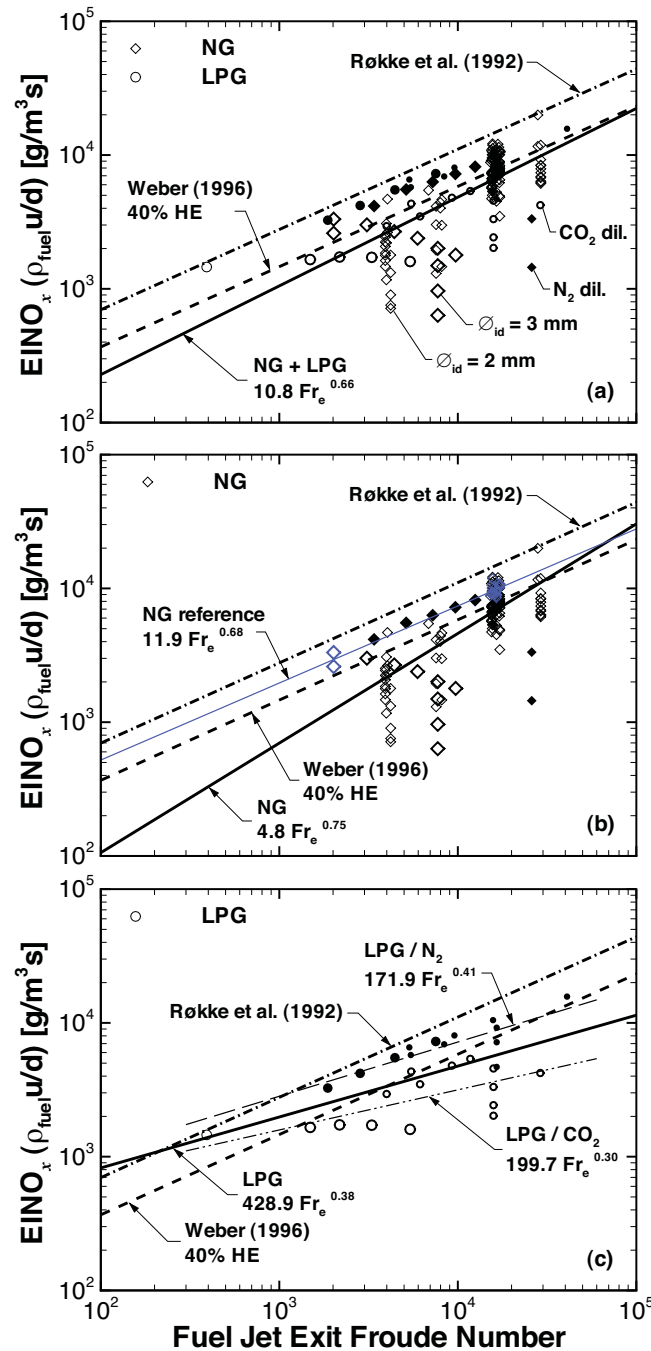
Figure 6.4: Leading-order NO$_x$ scaling correlation, $EINO_x \left(\rho_{fuel} u/d \right)$, versus fuel jet exit Froude number, Fr_e, for (a) all data points, (b) all cases burning NG, and (c) all cases burning LPG. The experimental data points are sorted according to fuel type, diluent and burner size. Diamonds: NG, circles: LPG, thin line symbols: no fuel dilution, solid symbols: N$_2$ dilution, thick line symbols: CO$_2$ dilution, small symbols: $\varnothing_{id} = 2.0$ mm, and large symbols: $\varnothing_{id} = 3.0$ mm. Blue coloured line and symbols on part (b) represent data for a reference condition ($17\% < \dot{Q}_{hx} < 30\%$, $12\,\mathrm{kW} < \dot{Q}_{fuel} < 16\,\mathrm{kW}$, $0.78 < \phi < 0.82$, $400°\mathrm{C} < T_{air} < 500°\mathrm{C}$).

earlier [161]. Costa et al. [34] found similar departures for their momentum-controlled open jet methane flames.

Part (b) and (c) of Figure 6.4, show that the slope for NG as the fuel ($\propto \mathrm{Fr}_e^{0.75}$) is significantly different from that of LPG as the fuel ($\propto \mathrm{Fr}_e^{0.38}$). The dependence on fuel type is expected from the model of Røkke et al. [161]. The effects of fuel dilution can also be observed in part (c), when the N$_2$ dilution cases ($\propto \mathrm{Fr}_e^{0.41}$) and the CO$_2$ dilution cases ($\propto \mathrm{Fr}_e^{0.30}$) are separately correlated.

Figure 6.5 shows the variation of the NO$_x$ emission index, EINO$_x$, with the momentum flux ratio of air, G_{air}, to fuel, G_{fuel}. Refer to §5.5.2 for the definition of the momentum flux ratio. Once again, the experimental data points are sorted according to fuel type, diluent and burner size. It is evident that no obvious correlation exists between EINO$_x$ and G_{air}/G_{fuel}. Other attempts to correlate EINO$_x$ with the total momentum flux ($G_{air} + G_{fuel}$), momentum flux ratio of fuel-to-exhaust ($G_{fuel}/G_{exhaust}$), and momentum flux ratio of air-to-exhaust ($G_{air}/G_{exhaust}$) have also failed to collapse the data.

The results presented in this section clearly show that the leading-order approach used for conventional combustion systems is not suitable for NO$_x$ scaling in the MILD regime. Other parameters that may influence the NO$_x$ formation in this furnace, such as chemical kinetic effects, must be examined.

6.4 Temperature-time Scaling

To further assess the role of the thermal-NO mechanism, the methodology proposed by Turns and Myhr [186] and Turns et al. [187] is adopted. They developed a successful global temperature-time NO$_x$ scaling relationship that accounted for radiation losses from open turbulent jet flames. The essence of the temperature-time scaling is the definition of a NO$_x$ production rate, which is calculated by dividing an average NO$_x$ concentration by a characteristic mixing time scale. The experimental NO$_x$ concentration is determined from mass-based emission indices and stoichiometry as,

$$[\mathrm{NO}_x] \; [\mathrm{mole/m^3}] = \frac{f \rho_{rct} \mathrm{EINO}_x}{\mathrm{MW_{NO}} \left(\frac{X_{\mathrm{NO}}}{X_{\mathrm{NO}_x}} \right) + \mathrm{MW_{NO2}} \left(\frac{X_{\mathrm{NO_2}}}{X_{\mathrm{NO}_x}} \right)} \; . \tag{6.1}$$
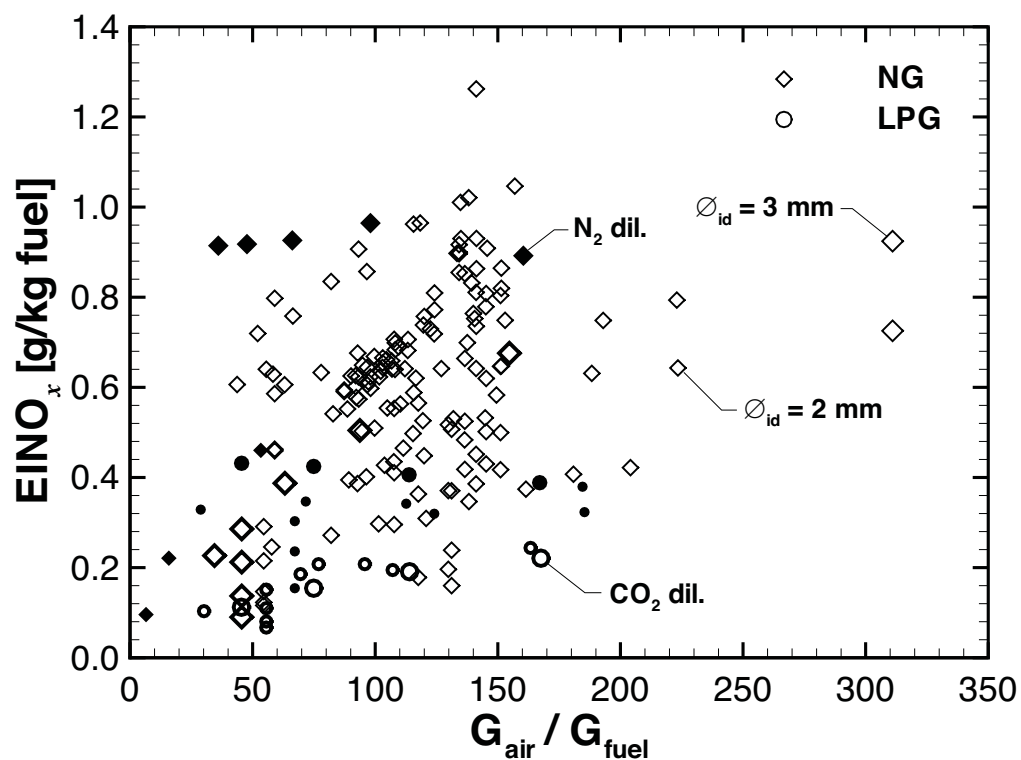
Figure 6.5: Relationship between the NO$_x$ emission index, EINO$_x$, and the momentum flux ratio of air-to-fuel, , for all tested operating conditions. The experimental data points are sorted according to fuel type, diluent and burner size. Diamonds: NG, circles: LPG, thin line symbols: no fuel dilution, solid symbols: N$_2$ dilution, thick line symbols: CO$_2$ dilution, small symbols: $\varnothing_{id} = 2.0$ mm, and large symbols: $\varnothing_{id} = 3.0$ mm.

Adapting the definition presented by Turns and Myhr [186] for open flames to enclosed multiple-jet systems, the global residence time (τ_G) is characterised by the combustion chamber volume and the volumetric flow rate of hot reactants as,

$$\tau_G\,[s] = \frac{4V_{MCF}f\rho_{rct}}{\pi d^2 u n \rho_{fuel}}\,, \tag{6.2}$$

where V_{MCF} is the MCF volume, f is the fuel mixture fraction, ρ_{rct} is the density of the mixture of reactants at furnace temperature, d is the fuel nozzle diameter, u is the fuel inlet velocity for a single nozzle, n is the number of round fuel nozzles, and ρ_{fuel} is the fuel density at ambient temperature. The use of the furnace volume to represent the reaction zone is a reasonable approximation for MILD combustion conditions and is consistent with the global treatment used in other studies involving furnaces [90]. The fuel mixture fraction is calculated from $f = \phi/\phi + (A/F)_{stoic}$ and implicitly incorporates the air mass flow rate. Here, $(A/F)_{stoic}$ is the value of stoichiometric air-to-fuel ratio. The denominator in equation 6.2 is directly related to the fuel mass flow rate, which in turn determines the fuel input power, also referred to as the firing rate.

A convective time scale, d/u, is commonly used as the scaling parameter in momentum-controlled open jet flames. For those flames, d/u is directly proportional to residence time because it controls flame volume. The convective time scale strongly influences the flame radiant fraction, and thus also the temperature and NO$_x$ emissions [139, 186]. In contrast, when the flame volume is fixed and where exit strain does not control flame stabilisation, d/u and τ_G are no longer directly proportional. For this reason, d/u is not a relevant parameter in enclosed systems, and does not collapse the NO$_x$ data.

Figure 6.6 shows an Arrhenius-type plot of NO$_x$ production rates calculated with the global residence time, τ_G, as a function of the reciprocal of the furnace temperature. The experimental data points are grouped according to global residence time. The various blue symbols refer to NO$_x$ production rates estimated from the work of various other researchers [32, 37, 98, 105, 147, 154, 171, 194, 199]. Three different lines are also shown in Figure 6.6. The dashed line represents the theoretical NO production rate via the Zel'dovich thermal-NO mechanism. The maximum NO formation rates were calculated for $\phi = 0.80$ considering a quasi-steady state approximation for N atoms, assuming equilibrium concentrations for

O atoms, and applying the forward reaction coefficient, k_{f1}, for the rate-limiting step in the thermal-NO formation process (equation 2.1), $O + N_2 \rightarrow NO + N$. The value for k_{f1} was computed from the expression recommended by Davidson and Hanson [47], k_{f1} [m^{3}s/mole] $= 1.95 \times 10^8 \exp(-38,660/T)$. The concentrations for the O and N atoms were calculated from the NASA chemical equilibrium code [77]. The dash-dotted line represents the two-parameter regression fit

$$\ln\left(\frac{[\text{NO}_x]}{\tau_G}\right) = A + B \ln(\tau_G) + \frac{C}{T} \tag{6.3}$$

for hydrocarbon flames for a residence time of 100 ms extrapolated for a lower temperature range from previous work by Turns et al. [187]. Finally, the solid line represents the data from the present study regressed in the same form as proposed by Turns and Myhr [186] and Turns et al. [187], for a residence time of 4 s. Here, [NO$_x$/τ_G] is the characteristic NO$_x$ production rate and the regression coefficients A, B and C are shown in Table 6.1.

Table 6.1: Regression coefficients for equation 6.3

Database	Parameters	A (ln(mol/cm^{3}s))	B (1/s)	C (K)	Temperature (K)
Turns et al. [187]	T_{flame} , τ_G	1.1146	-0.741	-16,347	1900−2350
	$T_{furnace}$, τ_G	-6.141	-0.387	-3,634	1050−1650
Present Study	τ_G	-8.106	-0.733	0	N/A
	$T_{exhaust}$	-2.249	0	-6,681	760−1070

Several observations arise from the results shown in Figure 6.6. The use of the global residence time to determine NO$_x$ production rates provides a general collapse of the experimental data. However, there is still considerable scatter in the data, which is slightly masked by the logarithmic scales on the axis. This scatter around a general correlation is also evident in the data of other researchers in the MILD regime. For example, the data from Plessing et al. [154] and Dally et al. [37] lie well within an acceptable error range. Interestingly, their measurements were carried out in a furnace with similar dimensions and operating conditions to the present facility, but with a completely different burner design, the FLOX® burner. On the other hand, all other data except for that of Özdemir and Peters
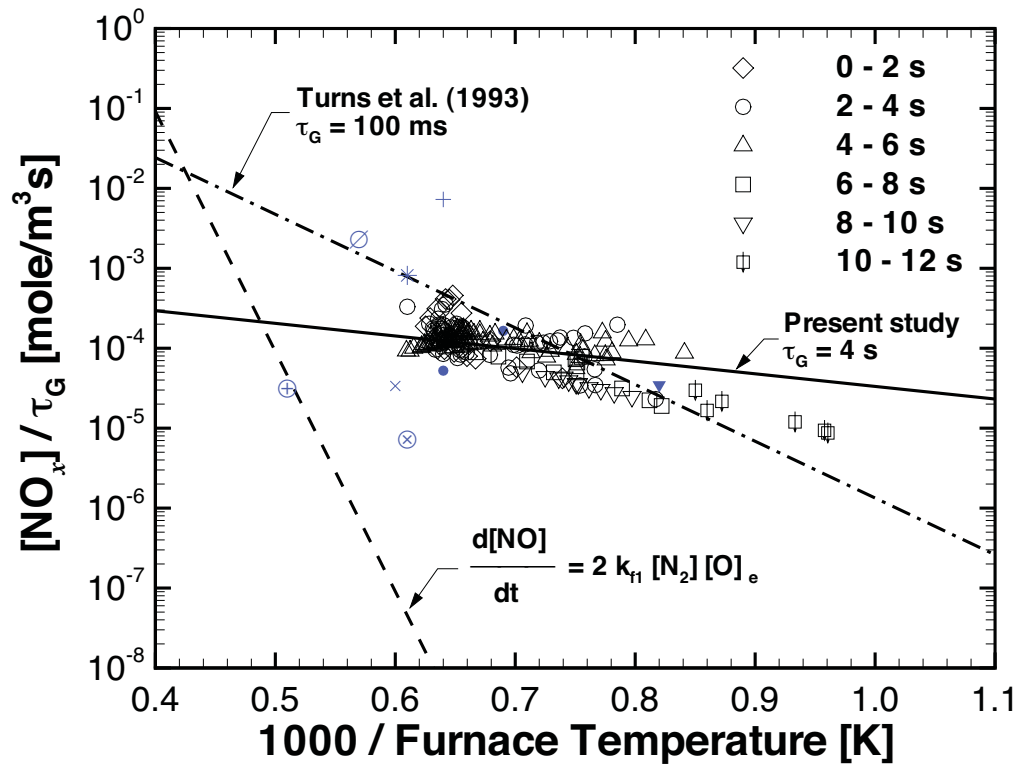
Figure 6.6: NO$_x$ production rates calculated with the global residence time, τ_G, as a function of the reciprocal of the furnace temperature. The experimental data points are grouped according to global residence time. $+$, CH$_4$ [199]; $*$, NG [98]; $\blacktriangledown$, CH$_4$ [154]; $\oplus$, NG [171]; $\times$, NG [194]; $\otimes$, CH$_4$ [32, 147]; $\varnothing$, LPG [105]; $\bullet$, CH$_4$ & C$_3$H$_8$ [37].

[32, 147], the rest of the data was measured in furnaces of different sizes that were fitted with unique burner arrangements. The temperature-time scaling demonstrates a considerably weaker dependence of NO$_x$ production rates on furnace temperature than that predicted by the thermal NO$_x$ route alone. This trend applies for highly diluted furnace environments regardless of the furnace/burner geometry. Importantly, although the magnitude of [NO$_x/\tau_G$] depends on the combustion chamber volume, the slope is independent of this definition. Sobiesiak et al. [171] also found a departure from the thermal-NO mechanism based on a well-stirred reactor model, especially at low characteristic temperatures.

The slope of the present data is also lower than the open methane, ethylene and propane flames of Turns et al. [187]. This shows that the dependence of NO$_x$ production rate on temperature is stronger for open turbulent jet flames, than for the present MILD combustion conditions. This finding is further supported by the much larger value of the temperature coefficient, C, presented in Table 6.1 for open flame conditions. Nevertheless, despite this weaker dependence, it appears that the temperature-time scaling correlation provides the single best description of NO$_x$ formation in the MILD regime.

To evaluate the quality of the regression fit for the present study, the percentage difference between the regression predictions of NO$_x$ production rates and the experiments is presented in Figure 6.7. The analysis is performed for the complete data set using a number of alternative parameters substituted in equation 6.3 (cf. Table 6.1). From top to bottom in Figure 6.7, the regression fit assesses respectively, furnace temperature and global residence time ($T_{furnace}$, τ_G), global residence time (τ_G) only, and exhaust temperature ($T_{exhaust}$) only as parameters. For the ($T_{furnace}$, τ_G) case, 77% of the data are within an error band of ±50% (or 92% within an error band of ±100%). Although the errors reach levels of up to 400%, an almost identical fit is found when only residence time is used, 77% of the data are within an error band of ±50% (or 87% within an error band ±100%). A slightly better fit is found when the regression is based on the exhaust temperature alone, 85% of the data are within an error band of ±50% (or 97% within an error band of ±100%). The higher quality of the ($T_{exhaust}$) regression than of the ($T_{furnace}$, τ_G) regression is consistent with the exhaust temperature being less susceptible to bias due to the proximity to a heat sink, as previously noted. The largest errors were found in the predictions of CO$_2$ dilution cases. However,

excluding those points did not improve the regression significantly. Likewise, a regression using exhaust temperature and global residence time ($T_{exhaust}$, τ_G) was not significantly different.
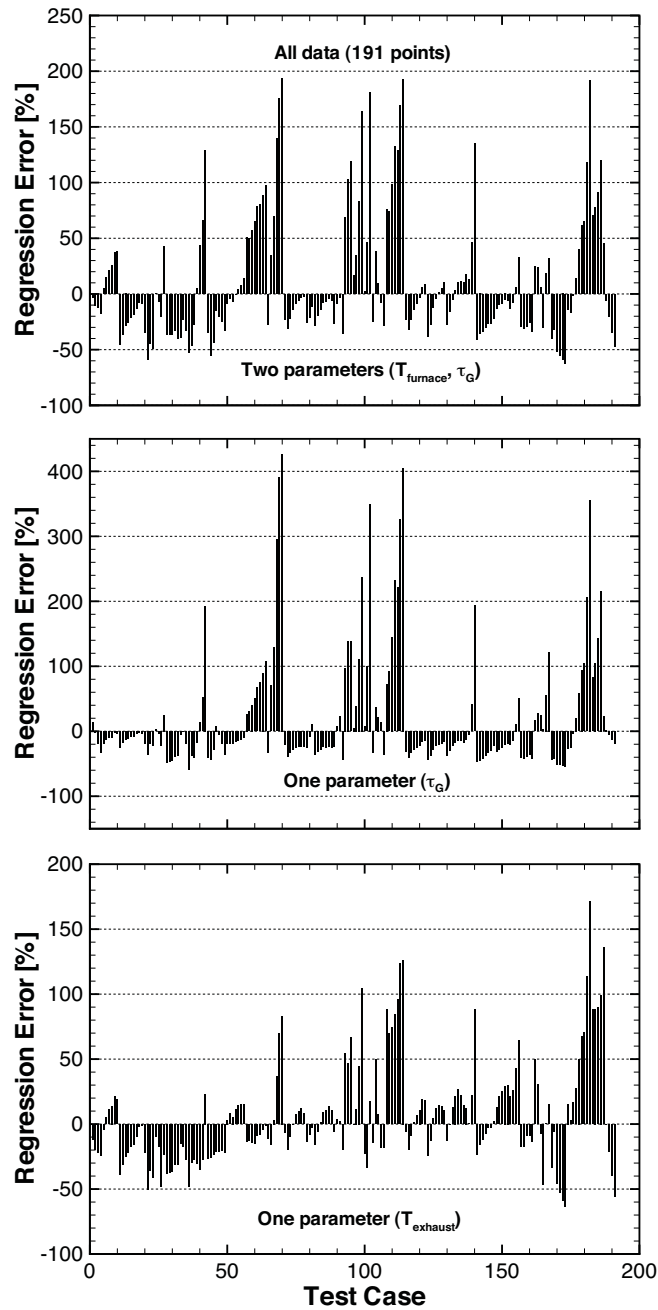

Figure 6.7: Percentage difference between the regression predictions (cf. Table 6.1) of NO$_x$ production rates and the experiments for all 191 data points.

6.5 Summary

In this chapter, the scaling of NO$_x$ emissions from the MCF was explored. A unique data set comprising 191 global measurements of temperature and exhaust gas emissions was systematically analysed. It was found that, although heat extraction, air preheat, excess air, firing rate, dilution, and fuel type all affect global NO$_x$ emissions, they do not control NO$_x$ scaling.

The leading-order approach showed that, although the jet exit Froude number has been used in the past for enclosed conventional flames, it is not the appropriate parameter for NO$_x$ scaling in the MILD regime. This is consistent with the weak role of buoyancy in a furnace with such low temperature gradients.

A global NO$_x$ production rate, calculated based on a global residence time and a characteristic furnace temperature, was found to give the best scaling of the data across all conditions assessed. However, the dependence on temperature was found to be much weaker than that expected based on the thermal-NO mechanism alone. This trend also applied to other MILD combustion systems, irrespective of the furnace/burner geometry. Furthermore, the regression analysis found that neither temperature nor global residence time provides a sufficiently strong correlation to be considered dominant. Regression-based predictions found the characteristic temperature and residence time to respectively correlate with 85% and 77% of the data within an error band of $\pm50\%$.

It is clear that no single NO$_x$ production mechanism is dominant in the present MILD combustion conditions. The nondominant role of the Zel'dovich thermal-NO mechanism is consistent with the moderate furnace temperatures ($800-1400°$C). Hence, it is deduced that the prompt-NO and/or N$_2$O-intermediate pathways are of significance comparable to that of the thermal-NO pathway. The reburn destruction mechanism, which was not accounted for in this NO$_x$ scaling analysis, may also affect global NO$_x$ emissions. Further assessments that estimate the contributions of each pathway to the overall NO$_x$ emissions through numerical modelling will be presented in the following chapters.

Chapter 7 Thermal, Flow and Scalar Fields

7.1 Introduction

This chapter examines the results of the numerical investigation described in Chapter 4. The CFD model is validated with the experimental data of a non-reacting isothermal case and selected reacting cases with and without external air preheat. The data available for validation consists of LDA measurements, in-furnace temperature measurements, an energy balance, and the exhaust gas composition. The validation process provides a way of assessing the suitability of different combustion models to predict the MILD combustion regime. The model that provided the best agreement with the experimental data is used later to further understand the passive and reactive scalar fields. The effect of the mixing patterns on the stability and reaction zone structure is investigated. Furthermore, an insight into the formation of CO and NO_x is provided.

7.2 Validation Results

7.2.1 Velocity

Nonreacting isothermal conditions

The turbulence model has a strong influence on the flow field and the turbulence-chemistry interaction in reacting flows. Therefore, an accurate description of the turbulence characteristics is crucial when modelling turbulent combustion. By

using nonreacting isothermal conditions, the performance of different turbulence models can be evaluated in isolation from the turbulence-chemistry effects. Calculations for the nonreacting case were performed with three variants of the $k-\epsilon$ turbulence model and a Reynolds stress model (RSM). Two modified versions of the standard $k-\epsilon$ (SKE) were also tested, one with the $C_{\epsilon 1}$ constant adjusted from 1.44 to 1.6 [28] and the other with the $C_{\epsilon 2}$ constant adjusted from 1.92 to 1.8 [114] in order to improve the predicted spread rate for the air jet.

Figures 7.1 through 7.4 show the comparison of measured and predicted mean axial (V_z) and radial (V_x) velocity profiles along the x and y axes for the different turbulence models at various axial locations. Despite some differences in the predictions of the maximum velocity of the air jet, the calculations near the jet exit plane show similar distributions for the axial velocity component, V_z, that are well matched to the experiments. The negative values measured for the radial velocity component, V_x, are reproduced by all models. It is worth mentioning that the first measurement height is still in the potential core of the jet, $z/D = 2.27$. Judging by the good agreement with the first two measured velocity profiles ($z = 60.5$ mm and $z = 176.5$ mm), the initial conditions for the air jet (see Figure 4.2) can be considered to be adequately represented.

Further downstream ($z > 176.5$ mm), the differences between the predictions of the models become more apparent. Interestingly, the largest discrepancies are seen for the RNG model. While the SKE model shows satisfactory predictions for most locations, some deviations from the measured values are observed, for instance at $z = 292.5$ mm of Figure 7.1 for $y > 20$ mm or at $z = 408.5$ mm of Figure 7.3. The discrepancies for the SKE model were somewhat expected because of the round-jet/plane-jet anomaly. The modification of the $C_{\epsilon 1}$ constant to compensate for the anomaly had only a marginal effect on the predictions. Adjusting the $C_{\epsilon 2}$ constant led to some improvement on the predictions, but did not correct for all deviations of the SKE model.

Overall, the velocity data for nonreacting conditions shows the recirculating nature of the flow field. The high momentum air jet expands through the furnace and generates a reverse flow ($V_z < 0$) when it interacts with the walls. The turbulence model that provided the best agreement with the experimental data was the realizable $k-\epsilon$ model. For clarity, the comparison between the velocity measurements and the predictions is repeated in Appendix E for the the realizable

$k - \epsilon$ model alone. Although the velocity profiles are well matched, particularly for the first two measurement heights ($z \leq 176.5$ mm), some discrepancies are still seen. These differences can be attributed mostly to the need to estimate the inlet velocity components in the x and y directions.

The RSM model did not provide sufficient improvements in accuracy to justify the associated computational cost. Hence, the realizable $k - \epsilon$ model was applied to the subsequent reacting cases.

Reacting conditions with and without air preheat

Profiles for mean axial velocity (V_z) at various locations for reacting conditions with and without external air preheat are shown in Figures 7.5 through 7.8. Calculations were performed with two different combustion models: a finite-rate/eddy dissipation model (FRED) with a two-step global reaction and the eddy dissipation concept (EDC) with the Smooke mechanism. The lack of measured data points at some locations is due to the volumetric expansion in the burnt gases that reduces data acquisition rates. Because of the much smaller magnitude of the radial velocity component (V_x), the data rates were very low leading to less reliable results. Hence the velocity data for reacting conditions is only presented for the axial direction, which is the dominant flow direction.

The results near the jet exit plane ($z = 60.5$ mm) clearly show the central air jet and fuel jets B and D in Figures 7.5 and 7.7, and fuel jets A and C in Figures 7.6 and 7.6. The fuel jet centres are located 110 mm from the origin and they are named according to their nearest side (see Figure 4.1). It is clear that the distance between the air and the fuel inlets delays the mixing between the reactant jets. Although the peak velocity is underestimated at $y = $ -10 mm of Figure 7.6 and at $x = $ -10 mm of Figure 7.7, the predictions of the central air jet are well matched to the experimental data for both combustion models.

There are some differences between the measured and the predicted fuel jet profiles. The EDC model consistently predicted a lower maximum velocity for the fuel jets for both operating conditions, except for fuel jet D in Figure 7.7. The axial velocities were close to zero or even slightly negative in the region between the fuel jets and the air jet, evidently due to the presence of the exhaust streams.

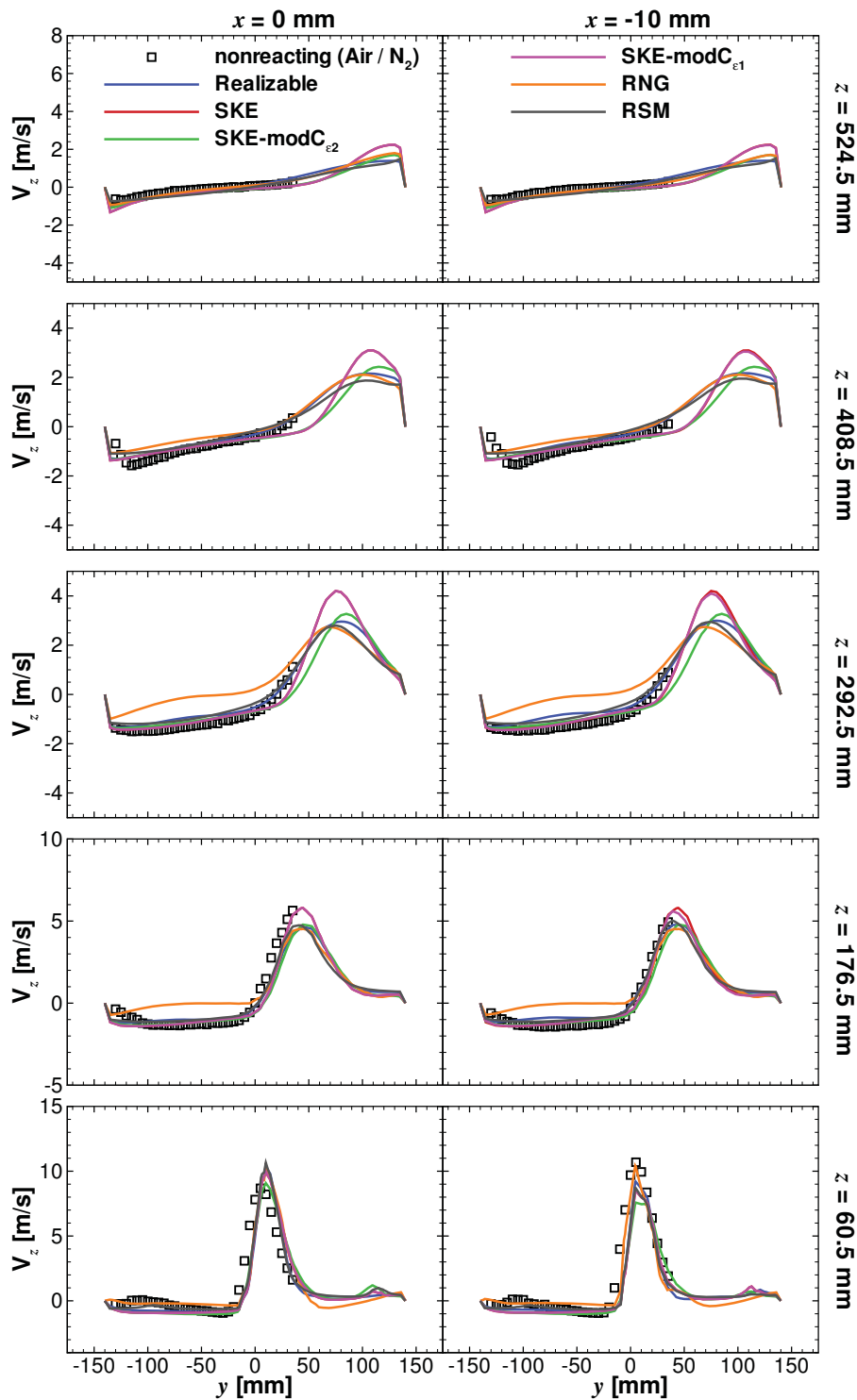The evolution of the measured velocity profiles downstream reveals an asym-

Figure 7.1: Comparison of measured and predicted mean axial velocity (V_z) profiles along the $y-$axis for nonreacting conditions at $x = 0$ (left) and $x = -10$ (right) for different turbulence models at various axial locations. Open symbols: experimental data, blue lines: realizable, red lines: $k - \epsilon$, green lines: $k - \epsilon$ with $C_{\epsilon 2} = 1.8$, purple lines: $k - \epsilon$ with $C_{\epsilon 1} = 1.6$, orange lines: RNG, and gray lines: RSM.
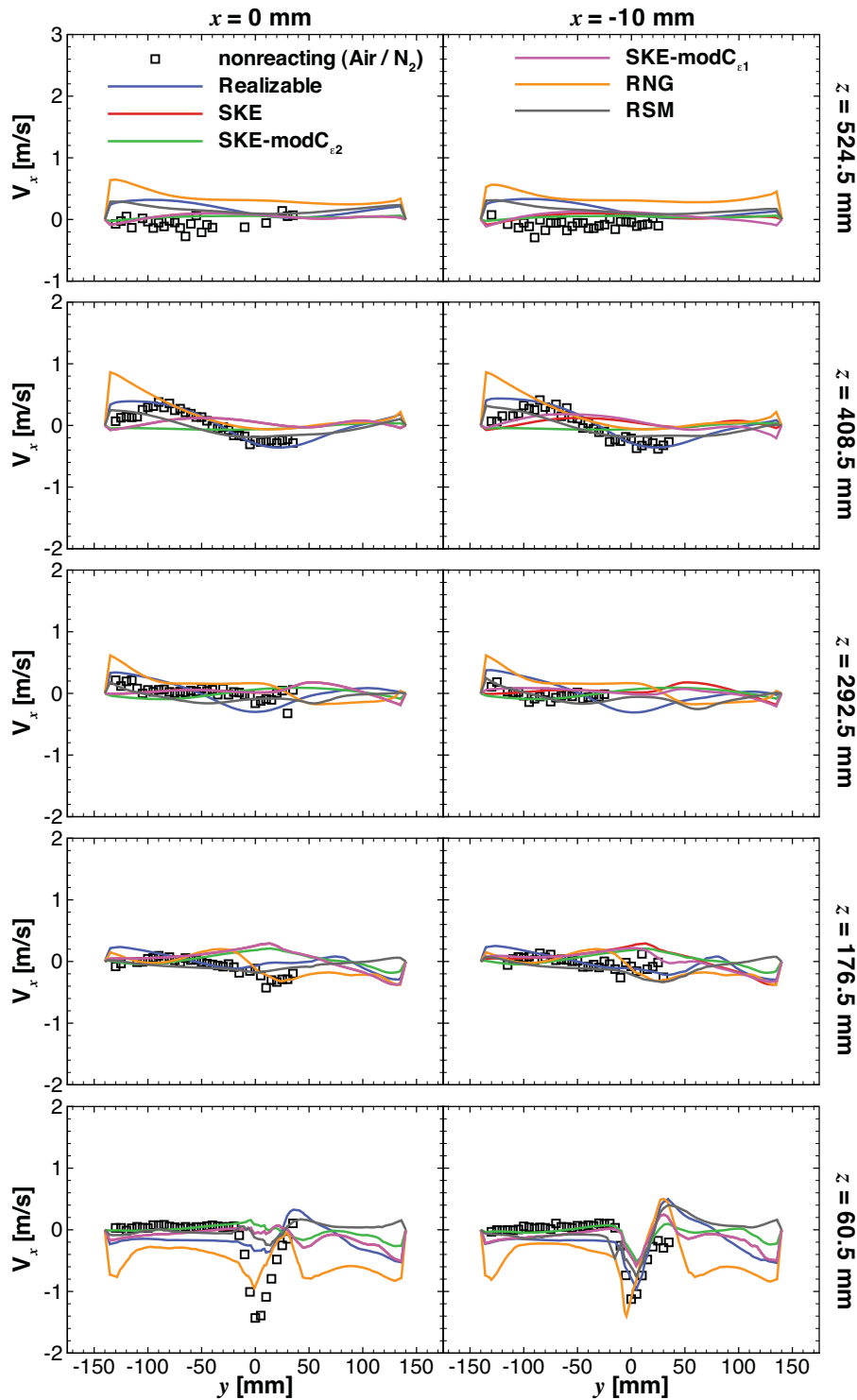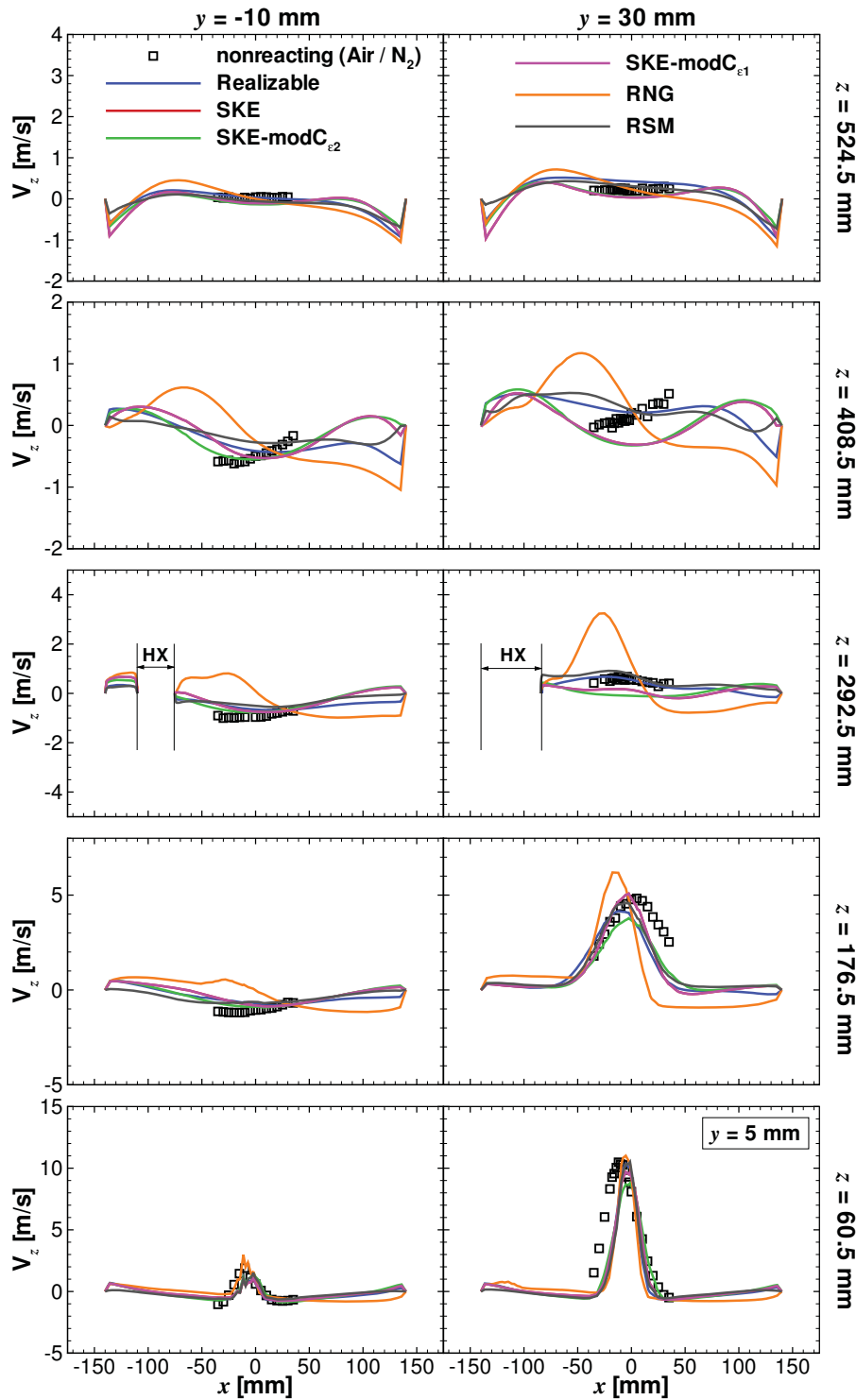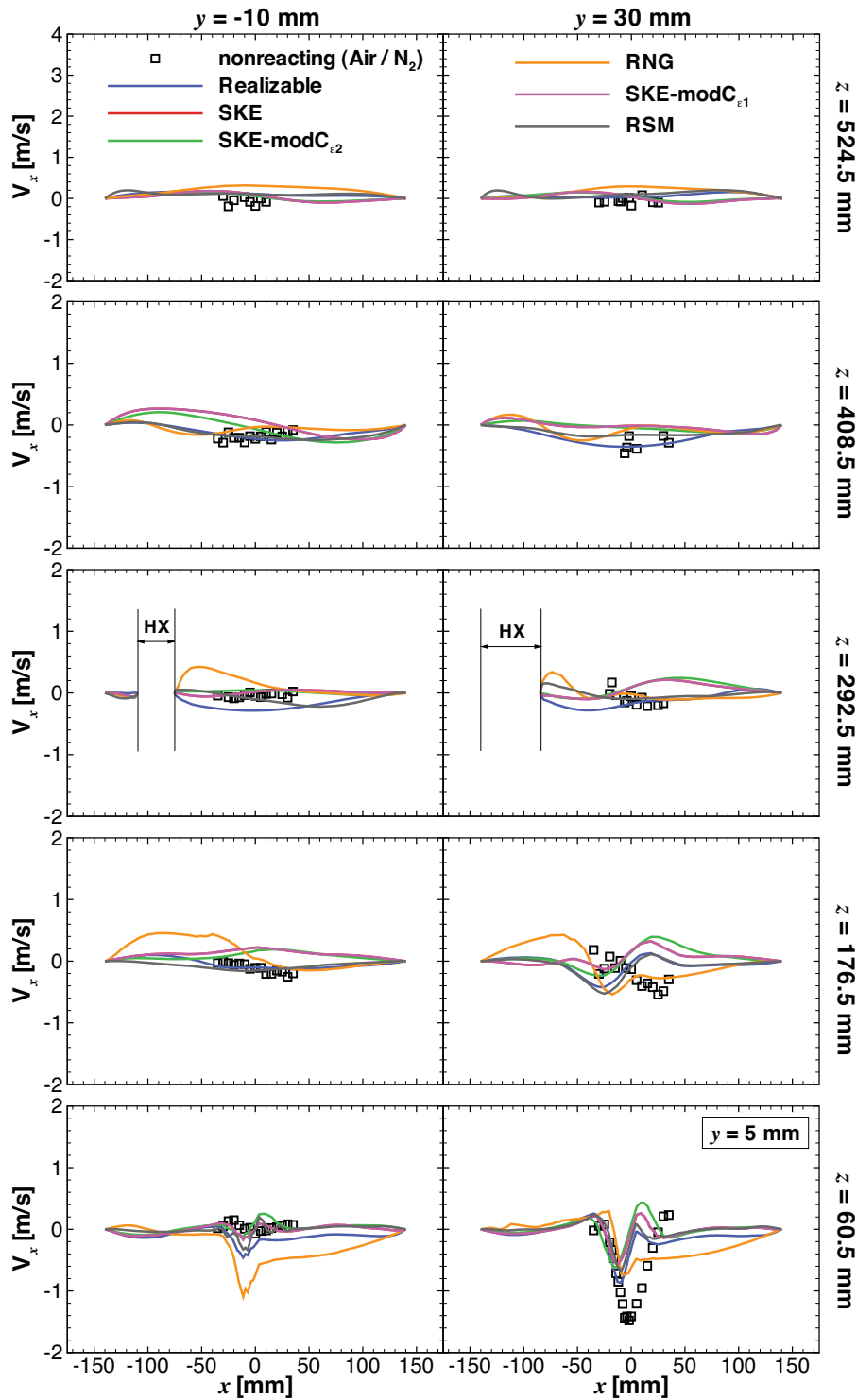
Figure 7.2: Comparison of measured and predicted mean radial velocity (V_x) profiles along the $y-$axis for nonreacting conditions at $x = 0$ (left) and $x = -10$ (right) for different turbulence models at various axial locations. Open symbols: experimental data, blue lines: realizable, red lines: $k - \epsilon$, green lines: $k - \epsilon$ with $C_{\epsilon 2} = 1.8$, purple lines: $k - \epsilon$ with $C_{\epsilon 1} = 1.6$, orange lines: RNG, and gray lines: RSM.

Figure 7.3: Comparison of measured and predicted mean axial velocity (V_z) profiles along the $x-$axis for nonreacting conditions at $y = -10$ (left) and $y = 30$ (right) with the exception of $y = 5$ (lower right) for different turbulence models at various axial locations. Open symbols: experimental data, blue lines: realizable, red lines: $k-\epsilon$, green lines: $k-\epsilon$ with $C_{\epsilon 2} = 1.8$, purple lines: $k-\epsilon$ with $C_{\epsilon 1} = 1.6$, orange lines: RNG, and gray lines: RSM.

Figure 7.4: Comparison of measured and predicted mean radial velocity (V_x) profiles along the $x-$axis for nonreacting conditions at $y = -10$ (left) and $y = 30$ (right) with the exception of $y = 5$ (lower right) for different turbulence models at various axial locations. Open symbols: experimental data, blue lines: realizable, red lines: $k-\epsilon$, green lines: $k-\epsilon$ with $C_{\epsilon 2} = 1.8$, purple lines: $k-\epsilon$ with $C_{\epsilon 1} = 1.6$, orange lines: RNG, and gray lines: RSM.

metric flow field. This was expected due to the fact that the inlet air velocity profile is not symmetrical. There are considerable discrepancies at $z = 176.5$ mm, particularly in the fuel jet. To assist in the analysis of the fuel jet expansion, auxiliary plots are shown at $z = 200$ mm in Figure 7.5, and at $z = 116$ mm in Figure 7.7. For the case without external air preheat, the FRED model overpredicts the penetration distance for fuel jet B, while the results of the EDC model show good agreement with the measurements. On the other hand, both models underpredicted the penetration distance for the case with air preheat. The FRED model appears to predict a larger penetration distance for the fuel jets than the EDC model.

The failure to predict the fuel jet structure has been attributed in the past to the non-stationary behaviour of the fuel jet [123, 146]. This possibility has been ruled out by performing unsteady calculations with the FRED model for the case with air preheat over time scales of 0.1, 0.2, 0.3, 1.3, 2.3, 3.3, 4.3, and 5.3 milliseconds. A steady-state calculation for the same conditions was performed with the $k - \epsilon$ model with the modified $C_{\epsilon 2}$ constant to test the effect of the turbulence model. No improvements were observed in the predictions of the fuel jet profiles. In light of the above it is suggested that the structure of the fuel jet at the burner nearfield is affected by the ability of the combustion model to capture the delayed ignition process.

The discrepancies observed in the air jet region in Figures 7.6 and 7.8, still at $z = 176.5$ mm, are likely a result of the failure to predict the complex entrainment process between the incoming fuel and air streams and the recirculating stream. This recirculation ($V_z < 0$), which seems to be formed as the gas stream interacts with the top surface of the furnace and side walls, is clearly visible for $z \geq 292.5$ mm. For these locations, there is no evidence of the individual fuel jets. Both combustion models show comparable predictions and good agreement with the experimental data, except in the region affected by the presence of the heat exchanger.

Overall, it is fair to say that there is reasonable agreement between the LDA data and the CFD calculations, which means that the flow structure for reacting conditions is well captured. More details of the flow field will be discussed in §7.3.
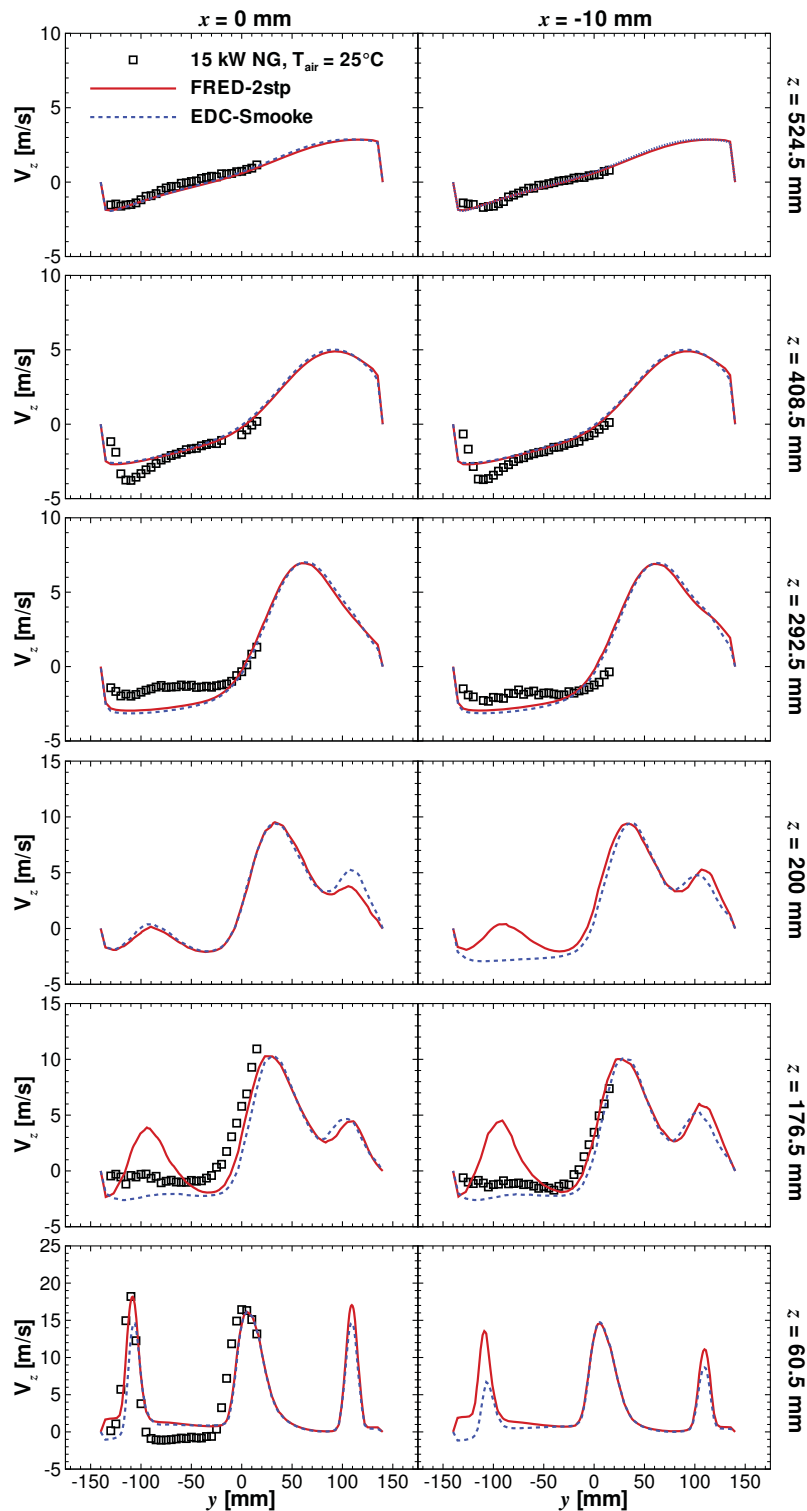
Figure 7.5: Comparison of measured and predicted mean axial velocity (V_z) profiles along the $y-$axis for the baseline case without air preheat, $T_{air} = 25°C$, at $x = 0$ (left) and $x = -10$ (right) for different combustion models at various axial locations. Open symbols: experimental data, solid lines: FRED with a two-step global chemistry, and dashed lines: EDC with the Smooke mechanism.
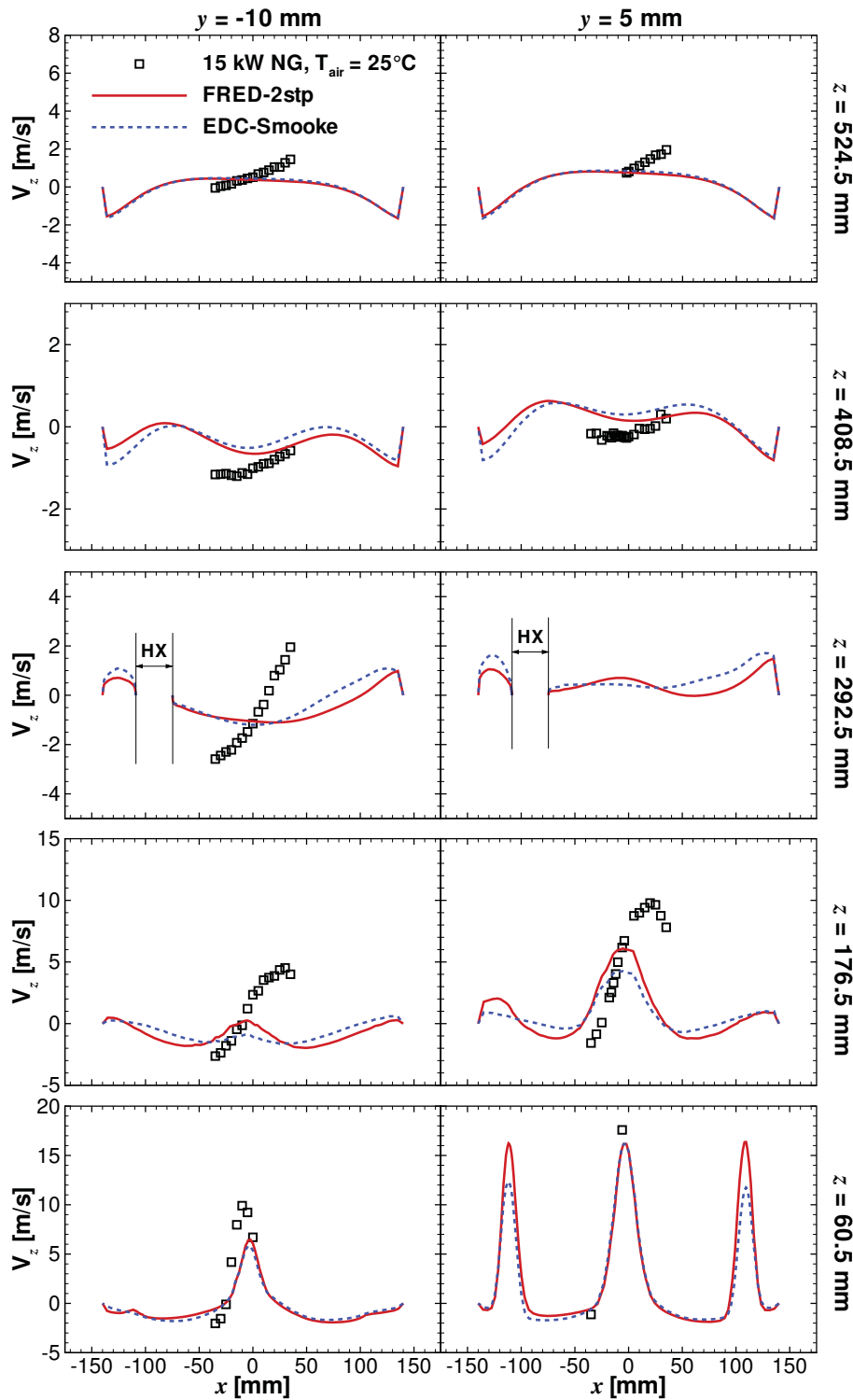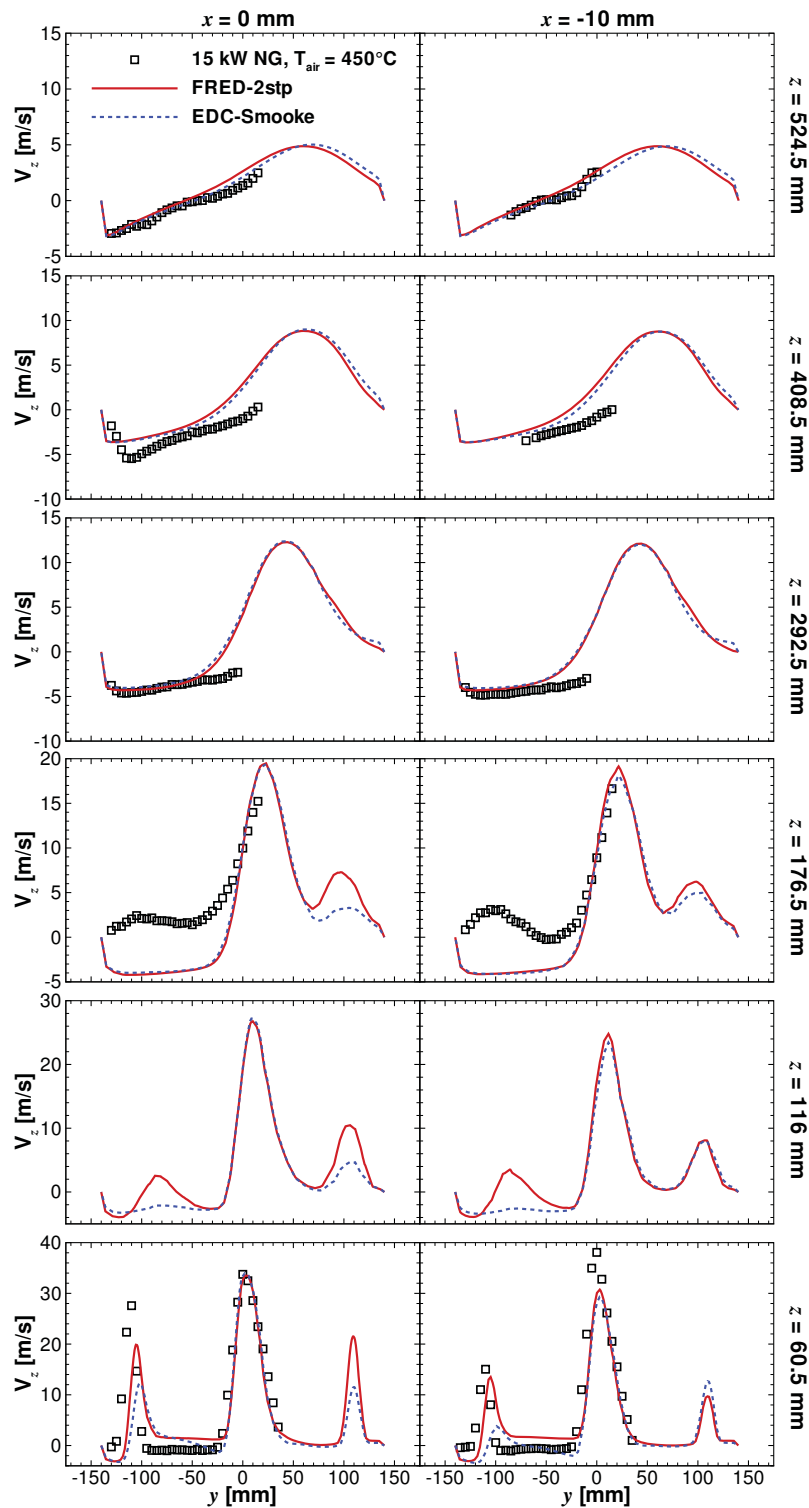
Figure 7.6: Comparison of measured and predicted mean axial velocity (V_z) profiles along the $x-$axis for the baseline case without air preheat, $T_{air} = 25°C$, at $y = -10$ (left) and $y = 5$ (right) for different combustion models at various axial locations. Open symbols: experimental data, solid lines: FRED with a two-step global chemistry, and dashed lines: EDC with the Smooke mechanism.
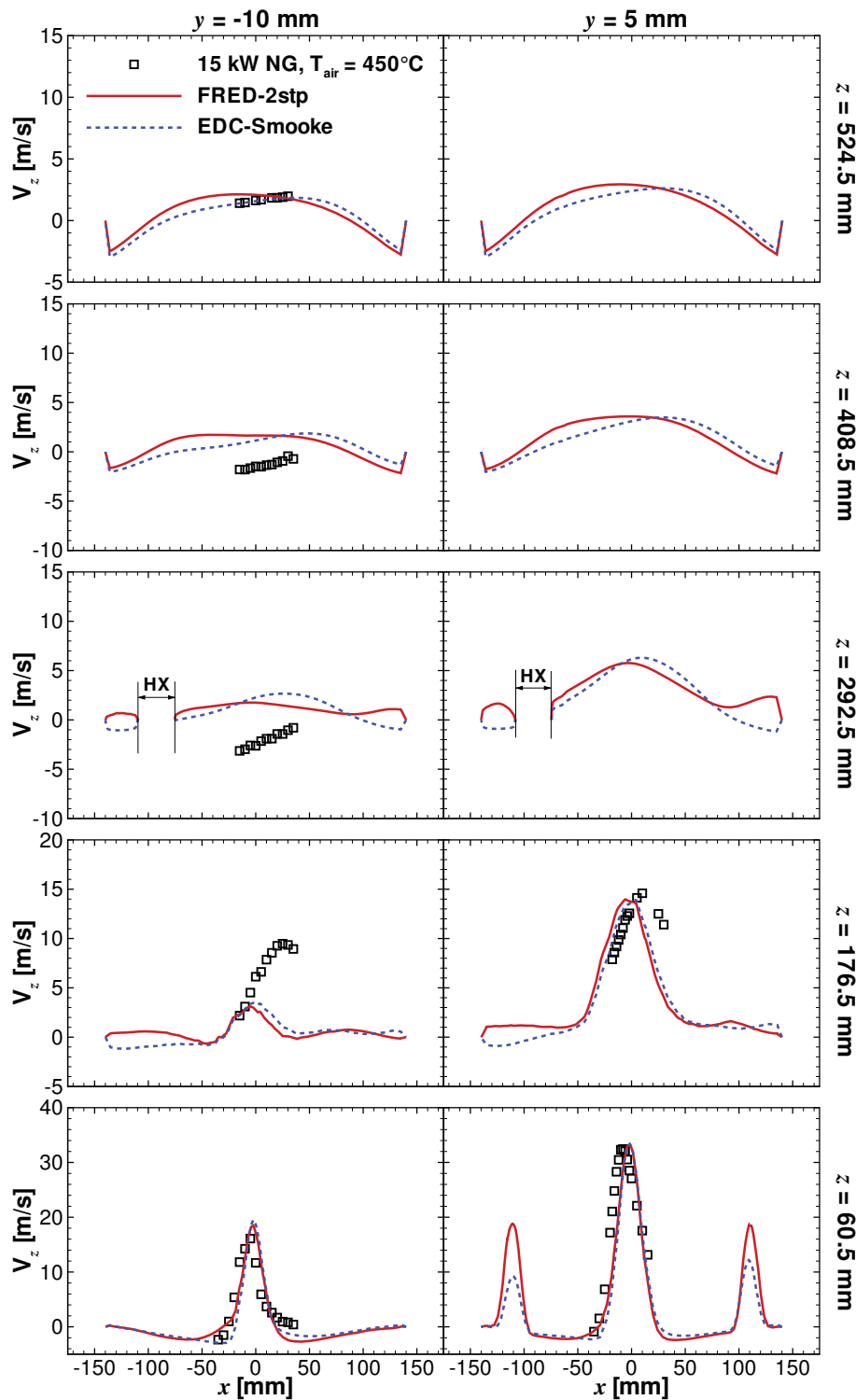
Figure 7.7: Comparison of measured and predicted mean axial velocity (V_z) profiles along the $y-$axis for the baseline case with air preheat, $T_{air} = 450°$C, at $x = 0$ (left) and $x = -10$ (right) for different combustion models at various axial locations. Open symbols: experimental data, solid lines: FRED with a two-step global chemistry, and dashed lines: EDC with the Smooke mechanism.

Figure 7.8: Comparison of measured and predicted mean axial velocity (V_z) profiles along the $x-$axis for the baseline case with air preheat, $T_{air} = 450°$C, at $y = -10$ (left) and $y = 5$ (right) for different combustion models at various axial locations. Open symbols: experimental data, solid lines: FRED with a two-step global chemistry, and dashed lines: EDC with the Smooke mechanism.

7.2.2 Temperature

Profiles for mean temperature at various axial locations are shown in Figures 7.9 and 7.10 for the baseline case with and without external air preheat. The calculations were performed using the same combustion models mentioned previously. The results show a remarkably uniform temperature distribution in a large part of the furnace. The FRED model consistently predicts higher temperatures than the EDC model. While the FRED model overpredicts temperatures up until $z = 242.5$ mm for the baseline case with air preheat and up until $z = 342.5$ mm for the baseline case with air preheat, the EDC model shows excellent agreement with the experimental data in most instances. Both combustion models show comparable predictions above these heights.

The highest temperature was predicted to be around $1640°C$ and $1400°C$ for the case without air preheat, and $1800°C$ and $1520°C$ for the case with air preheat in the region of fuel jet B at $z = 42.5$ mm, respectively for the FRED and the EDC models. It is clear from the calculations that the EDC model with detailed chemistry displays significantly slower reaction rates than the FRED model with the two-step mechanism. This is supported by the substantially lower temperatures calculated with the EDC model around the fuel jets at the burner nearfield locations. The failure of global reaction schemes to describe the delayed ignition of MILD combustion close to the burner exit plane have been previously reported [107, 146]. Other attempts to improve the predictions with simplified chemistry by either adjusting the empirical coefficients of the ED model [117, 202], or including a more complete representation of CO oxidation [99] have shown only minor improvements. This suggests that finite-rate chemistry effects need to be considered to more accurately predict the structure of the fuel jet.

The largest discrepancies between the predictions and the experiments around the air jet are seen at the centreline plane ($x = 0$ mm), particularly for the case without air preheat. These differences are quite likely caused by some of the inaccuracies observed in the predictions of the flow field, which were discussed in §7.2.1.

Within the boundaries of experimental uncertainty, the EDC model provided the most accurate predictions of the thermal field for both operating conditions.
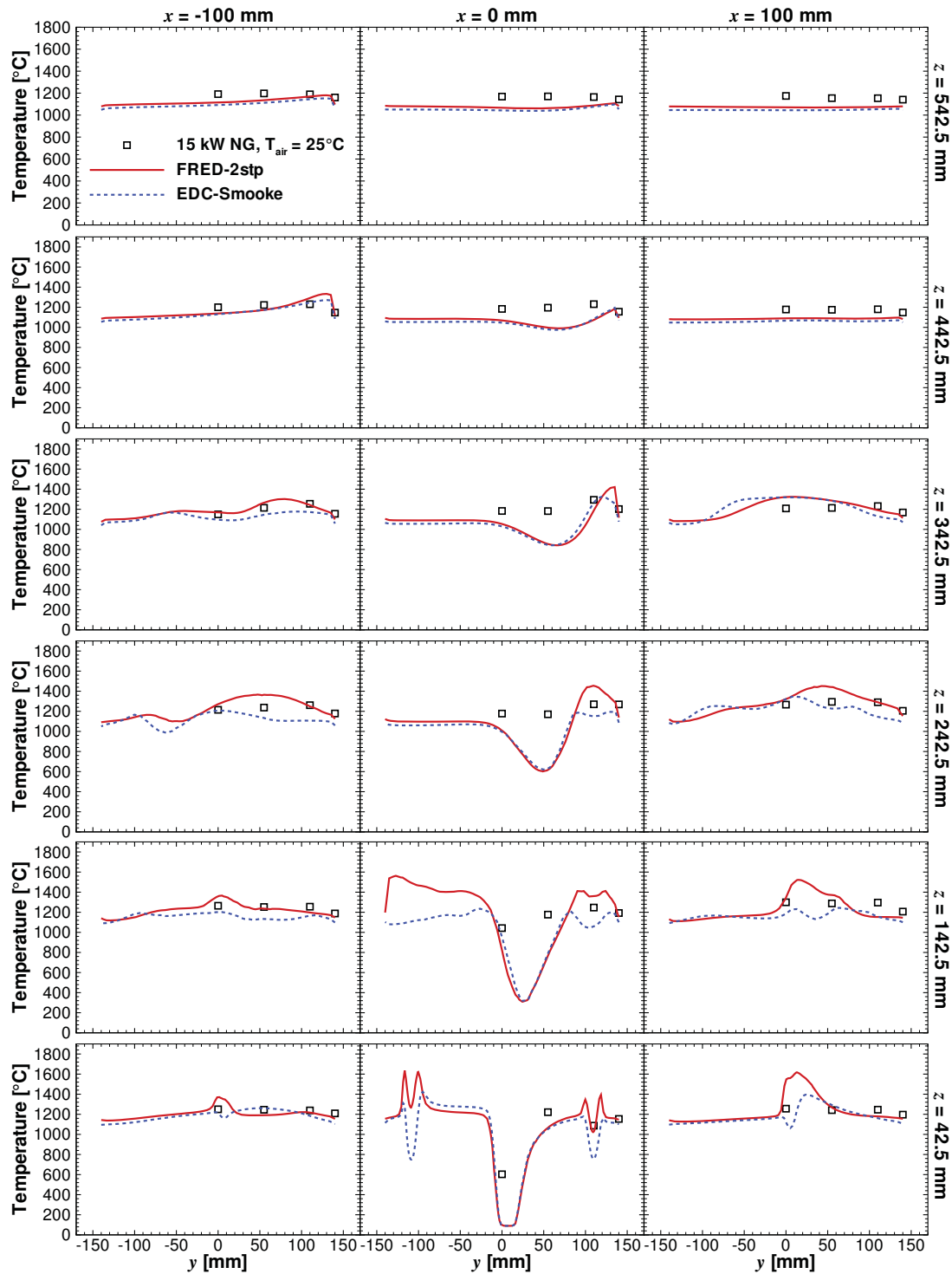
Figure 7.9: Comparison of measured and predicted temperature profiles along the y−axis for the baseline case without air preheat, $T_{air} = 25°C$, at $x = −100$ (left), $x = 0$ (centre) and $x = 100$ (right) for different combustion models at various axial locations. Open symbols: experimental data, solid lines: FRED with a two-step global chemistry, and dashed lines: EDC with the Smooke mechanism.
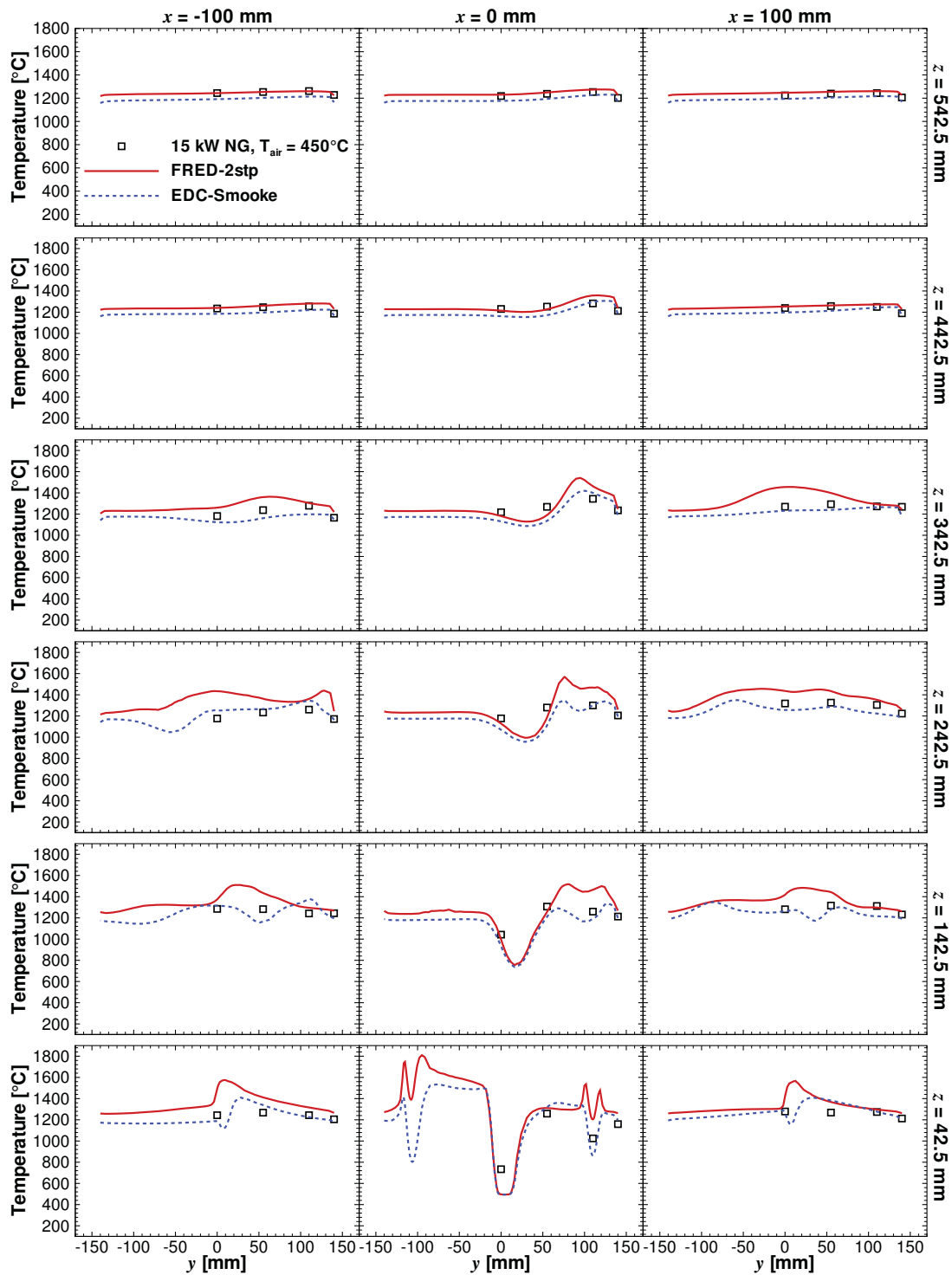
Figure 7.10: Comparison of measured and predicted temperature profiles along the y−axis for the baseline case with air preheat, $T_{air} = 450$°C, at $x = -100$ (left), $x = 0$ (centre) and $x = 100$ (right) for different combustion models at various axial locations. Open symbols: experimental data, solid lines: FRED with a two-step global chemistry, and dashed lines: EDC with the Smooke mechanism.

7.2.3 Energy balance

It is essential to accurately capture the heat losses from the combustion chamber for good quality predictions of the thermal and chemistry fields. Table 7.1 shows the energy balance obtained by evaluating the terms of equation 3.1 for the experiments and both combustion models used in this study for the baseline case with and without air preheat. Each heat loss term have been represented as a percentage of the total thermal input.

The energy balance estimated from the input-output measurements is closed to within 4% for both operating conditions, which is considered to be quite reasonable. Experimental uncertainties and unaccounted losses, such as leaks, are included in the other losses term. It is important to highlight that, because the surface-to-volume ratio of the MCF is high, the radiation losses though the windows are considerable.

The FRED model overpredicts the heat extraction by 12% and 24%, and underpredicts the walls losses by 10% and 5%, respectively for the baseline case with and without air preheat. While for the former case the EDC model underpredicts the heat extraction by 4%, it overpredicts by 16% for the latter case. The EDC model also underpredicts the wall losses by 16% and 9%. Since window openings were not included in the CFD model, the major difference between the predictions and the experimental data is the exhaust gas losses. For this reason the predicted exhaust temperatures tend to be higher than in the experiments.

Overall, the heat transfer through the heat exchanger and through the furnace walls has been captured quite well in the CFD modelling.

7.2.4 Exhaust emissions

Table 7.2 shows the comparison between the measured and predicted exhaust gas composition. The O_2 and CO_2 concentrations at the exhaust are well matched to the experimental data for both combustion models for the baseline case with air preheat. The slight departure from the measured CO_2 values is likely due to the use of pure methane as the fuel in the calculations instead of natural gas (refer to Table 5.1). Even though the boundary conditions were identical to the FRED model, the EDC model underpredicts the excess air level for the case without external air preheat, resulting in a higher concentration of CO_2.

The models captured the low levels of unburned hydrocarbons (C_xH_y) observed at the exhaust. However, while the experimental data shows virtually no emissions of CO for $\phi = 0.8$, both combustion models predict some CO emissions for both preheated and nonpreheated cases. In the former case, relatively high levels (860 ppm @ 3% O_2) were predicted with the EDC model. The reasons for this discrepancy will be investigated in §7.4.

The reference case for the NO_x predictions considered the thermal-NO, prompt-NO and N_2O-intermediate formation pathways and was termed Full NO. The influence of the NO destruction route was investigated by also including the reburn mechanism, Full NO + reburn case. To determine the relative importance of each NO formation mechanism the thermal-NO and the prompt-NO mechanisms were individually considered, Thermal only and Prompt only cases.

Although in the same order of magnitude as the measured levels, both combustion models underpredict the total NO_x emissions. While the FRED model predicts NO_x levels 43% and 55% lower than the experiments, the EDC model predicts NO_x levels 28% and 62% lower, respectively for the baseline case with and without air preheat.

The contribution of the prompt-NO mechanism to the total NO_x emissions seems to be of little importance under the investigated conditions. Since the thermal-NO mechanism only accounts for 17% and 27%, respectively for the preheated and nonpreheated cases, it is deduced that NO_x is mainly formed via the N_2O-intermediate pathway. The results show that NO destruction via the reburn mechanism is possible, and may reduce NO_x emissions up to 28%.

The same NO_x post-processor models were used with the FRED and EDC combustion models. Thus, the differences in the NO_x predictions between these models may solely be attributed to differences in the temperature and chemistry fields. The formation of NO_x will be further analysed in §7.5.

Table 7.1: Overall energy balance for the baseline case with and without air preheat for different combustion models

Case	Fuel input (kW)	Air input (kW)	Total input (kW)	Heat extracted (kW)	(%)	Wall loss (kW)	(%)	Exhaust loss (kW)	(%)	Window loss (kW)	(%)	Other losses (kW)	(%)
without air preheat ($T_{air} = 25°C$)													
Experiments	15.03	0.01	15.04	2.75	18.3	3.76	25.0	5.11	34.0	2.80	18.6	0.61	4.1
FRED-2stp	15.00	0.29	15.29	3.41	22.3	3.58	23.4	8.30	54.3	–	–	–	–
EDC-Smooke	15.00	0.30	15.30	3.18	20.7	3.42	22.4	8.71	56.9	–	–	–	–
with air preheat ($T_{air} = 450°C$)													
Experiments	15.14	3.12	18.25	4.30	23.5	4.49	24.6	5.43	29.8	3.30	18.1	0.73	4.0
FRED-2stp	15.20	2.89	18.09	4.80	26.5	4.03	22.3	9.26	51.2	–	–	–	–
EDC-Smooke	15.20	3.02	18.23	4.12	22.6	3.78	20.7	10.33	56.7	–	–	–	–

Table 7.2: Exhaust emissions for the baseline case with and without air preheat for different combustion models

Case	O_2 (%)	C_xH_y (ppmvd)	CO_2 (%)	CO (ppmvd) @ 3% O_2	NO_x (ppmvd) @ 3% O_2 Full NO	Full NO + reburn	Thermal only	Prompt only
without air preheat ($T_{air} = 25°C$)								
Experiments	4.2	< 100.0	9.0	0.9			33.3	
FRED-2stp	4.3	140.4	9.3	147.0	14.9	–	–	–
EDC-Smooke	3.8	0.2	9.6	96.8	12.8	9.2	2.2	0.1
with air preheat ($T_{air} = 450°C$)								
Experiments	4.2	< 100.0	9.0	3.5			40.7	
FRED-2stp	4.4	26.8	9.3	98.6	23.0	–	–	–
EDC-Smooke	4.2	1.6	9.3	860.2	29.6	25.3	8.1	0.1

7.3 Mixing Patterns and Thermal Field

The validation process carried out in §7.2 provided a good way for assessing the performance of each combustion model in predicting MILD combustion. However, the analysis is limited to the regions where measurements are available. Since the CFD model has been validated against the experimental data, further insight into the passive and reactive scalar fields can be gained from the numerical simulations. The validation results have shown that the EDC model with the Smooke mechanism generally provided more accurate predictions than the FRED model with the two-step global mechanism. For this reason, most of the analysis presented hereafter will use the results obtained with the EDC model.

MILD combustion systems can be assessed on the effectiveness with which they dilute the fresh reactants with combustion products before they can react. Hence the mixing patterns inside the furnace and its influence on the oxidation process must be investigated. Figures 7.11 and 7.12 show the pathlines originated in the air and the four fuel nozzles calculated with the EDC model for the baseline conditions. For better visualisation of the flow features and flame propagation, each incoming stream was represented separately with different colours and the surface where the mixture fraction is calculated to be stoichiometric was superimposed. The mean mixture fraction (ξ) was computed using the Bilger formulation [16] as follows:

$$\xi = \frac{\frac{2Z_C}{W_C} + \frac{Z_H}{2W_H} + \frac{Z_{O,2} - Z_O}{W_O}}{\frac{2Z_{C,1}}{W_C} + \frac{Z_{H,1}}{2W_H} + \frac{Z_{O,2}}{W_O}} \ , \tag{7.1}$$

where Z_i is the mass fraction, and W_i is the atomic mass for the elements carbon, hydrogen and oxygen. The subscript 1 and 2 refer to values in the fuel and air streams, respectively. All species of the Smooke mechanism were included in the calculations. For the methane-air system, the stoichiometric mixture fraction is $\xi_{st} = 0.0552$.

A highly convoluted three-dimensional flow field with asymmetrical characteristics is evident from Figures 7.11 and 7.12. The central air jet dominates the flow patterns, since its momentum flux is about 150 times higher than the fuel jet momentum for the baseline case with air preheat, and about 50 times higher for the baseline case without air preheat. The velocity isosurface plots shown in
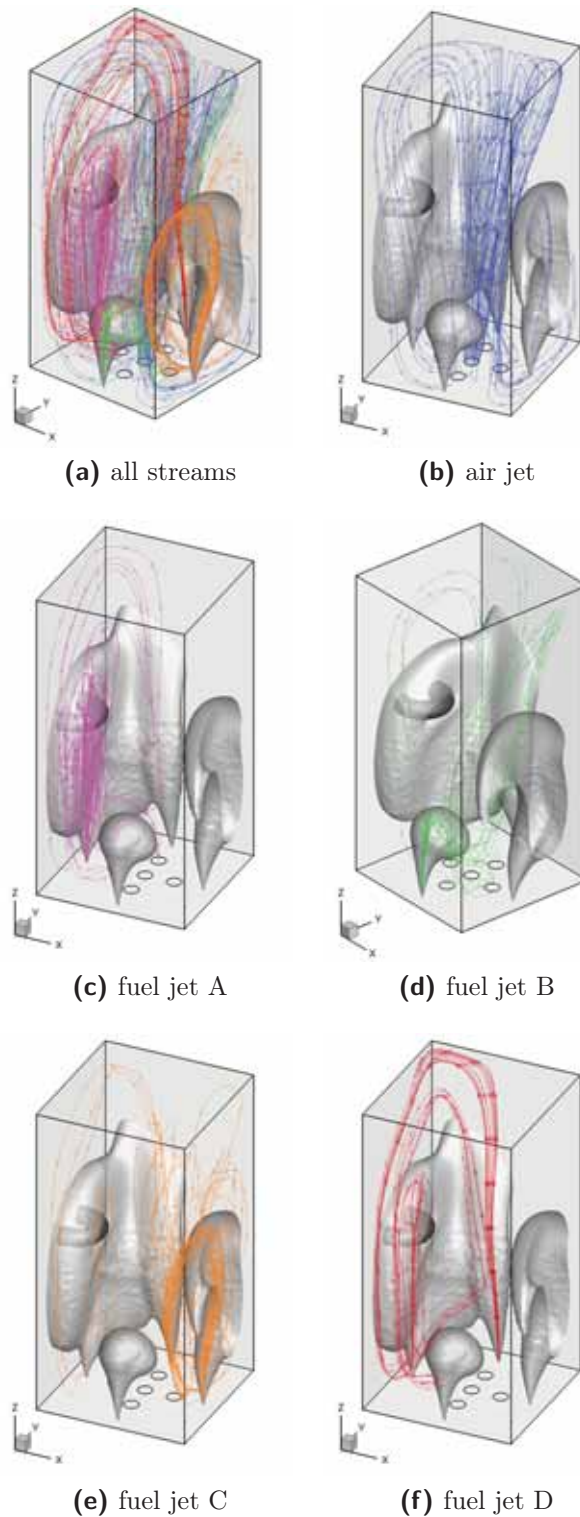
(a) all streams

(b) air jet

(c) fuel jet A

(d) fuel jet B

(e) fuel jet C

(f) fuel jet D

Figure 7.11: Pathlines inside the furnace with stoichiometric surface ($\xi_{st} = 0.0552$) overlaid for the baseline case without air preheat, $T_{air} = 25°C$, for the EDC model with the Smooke mechanism. Blue lines: air jet, purple lines: fuel jet A, green lines: fuel jet B, orange lines: fuel jet C, and red lines: fuel jet D.
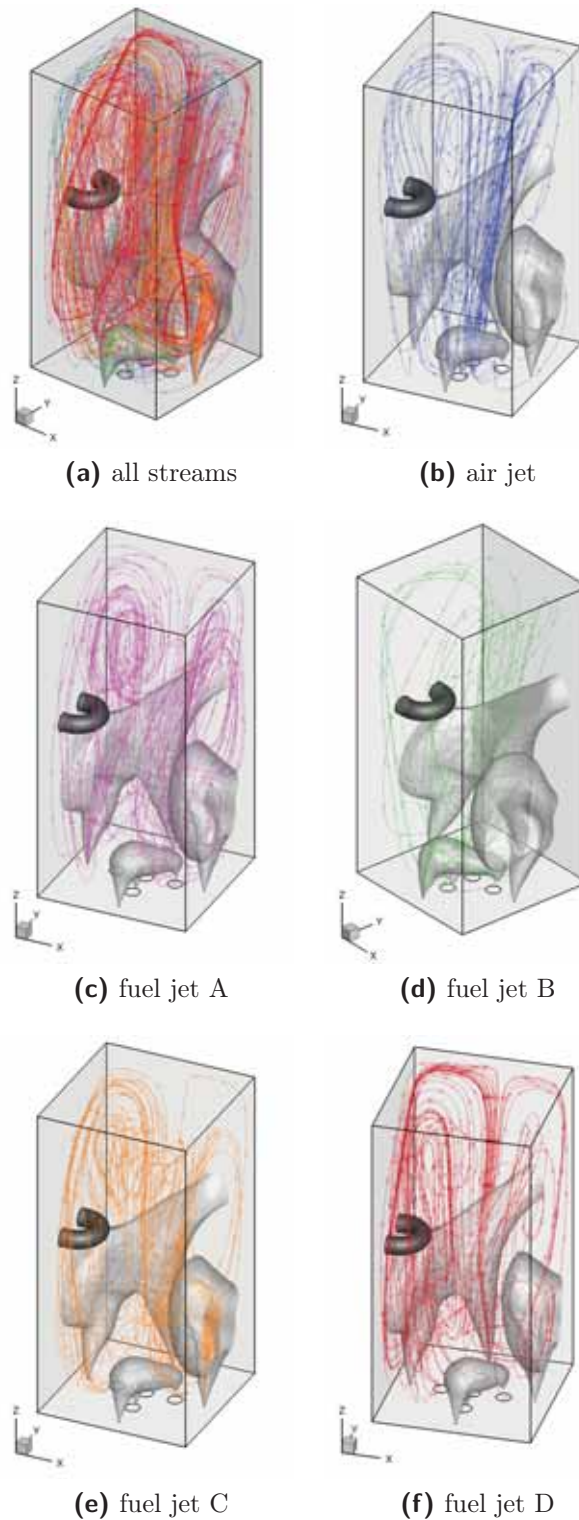
(a) all streams

(b) air jet

(c) fuel jet A

(d) fuel jet B

(e) fuel jet C

(f) fuel jet D

Figure 7.12: Pathlines inside the furnace with stoichiometric surface ($\xi_{st} = 0.0552$) overlaid for the baseline case with air preheat, $T_{air} = 450°$C, for the EDC model with the Smooke mechanism. Blue lines: air jet, purple lines: fuel jet A, green lines: fuel jet B, orange lines: fuel jet C, and red lines: fuel jet D.

Figures 7.13 and 7.14 illustrate these differences in jet momentum.

The air jet expands through the furnace and drives a recirculation zone when it interacts with the walls. The recirculation stream has a significant influence on the trajectory of the fuel jets, and hence on the structure of the reaction zone. The intense turbulent mixing conditions is evidenced by the mixture fraction contour plots shown in Figures 7.15 and 7.16. The stronger the recirculation, such as in the case with air preheat, the smaller the penetration distance of the fuel jets. Each of the fuel jets entrain furnace gases before mixing with the air stream, creating three spatially distinct reaction zones: the largest in volume being formed around both fuel jets A and D, and then around fuel jet C and the smallest around fuel jet B.

Figures 7.17 and 7.18 show a comparison of axial velocity contours for the preheated and nonpreheated conditions at different horizontal and vertical cross sections. In order to further characterise the recirculation inside the furnace, the locus of zero axial velocity is represented. It should be noted that recirculation, in the context of this thesis, is defined as negative axial velocities ($V_z < 0$), and therefore differs from the concept of circulation commonly used in fluid dynamics. Here, and wherever possible throughout this chapter, the contour scale and levels are kept the same for both operating conditions to make comparison easier.

The asymmetries in the flow patterns due to the air inlet velocity profile are clearly visible in Figures 7.17 and 7.18 with the recirculation forming preferably towards $y < 0$ alongside wall B. Since the air stream reaches velocities as high as 40 m/s for the case with air preheat, compared to a maximum velocity of around 18 m/s for the case without air preheat, a stronger reverse flow is generated. The effect of the recirculation on the penetration distance of the fuel jets, which is injected into the furnace with the same momentum for both operating conditions, is evident particularly for fuel jet B, as shown in parts (b) and (d) of Figure 7.17.

Figures 7.19 and 7.20 present the predicted temperature distribution for the baseline case with and without external air preheat through the furnace centreline and at different $x - y$ planes, respectively. To delineate the reaction zone, the temperature contours are overlaid with the stoichiometric surface ($\xi_{st} = 0.0552$). As expected, the temperatures in the case without air preheat are lower than for the case with air preheat. The difference in magnitudes between the two cases is not more pronounced because, although the heat exchanger position and
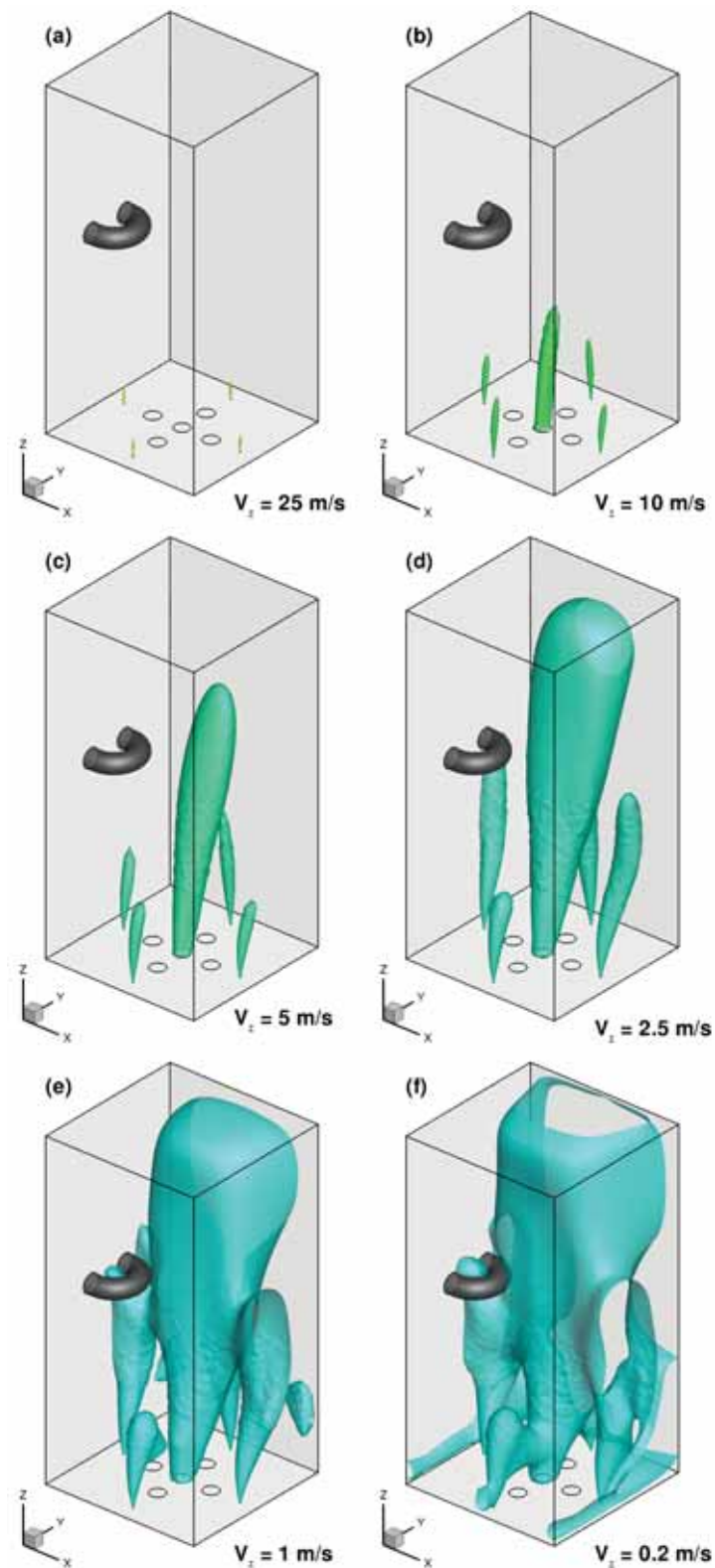
Figure 7.13: Predicted mean axial velocity (V_z) isosurface plots for the baseline case without air preheat, $T_{air} = 25°C$, for the EDC model with the Smooke mechanism. The threshold value that defines the isosurface for V_z is represented in the lower right corner of each plot.
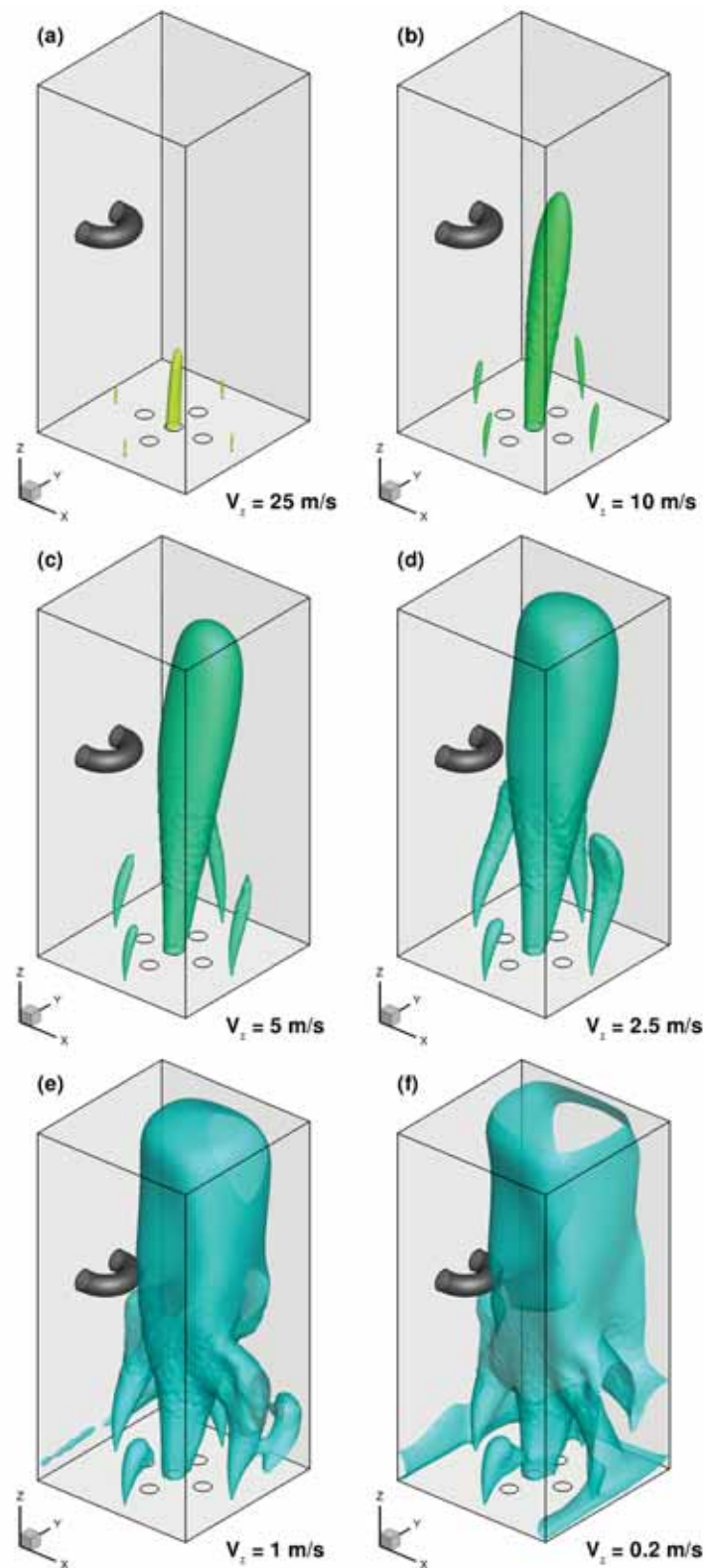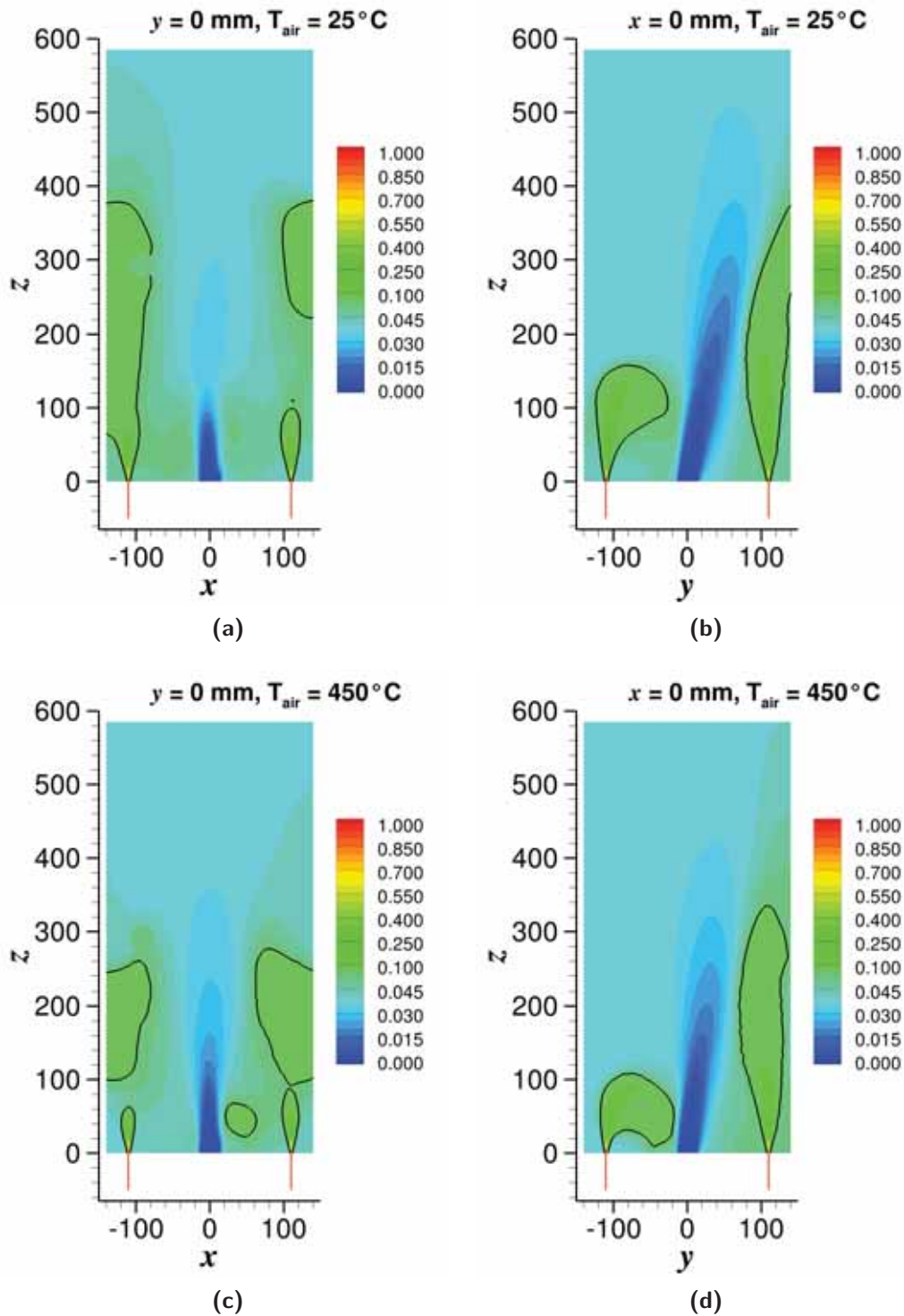
Figure 7.14: Predicted mean axial velocity (V_z) isosurface plots for the baseline case with air preheat, $T_{air} = 450°$C, for the EDC model with the Smooke mechanism. The threshold value that defines the isosurface for V_z is represented in the lower right corner of each plot.

Figure 7.15: Computed mixture fraction (ξ) contours with stoichiometric surface ($\xi_{st} = 0.0552$) overlaid for the baseline case, (a) and (b) without air preheat, $T_{air} = 25°C$, and (c) and (d) with air preheat, $T_{air} = 450°C$, for the EDC model with the Smooke mechanism at the $x - z$ and $y - z$ centreline planes.

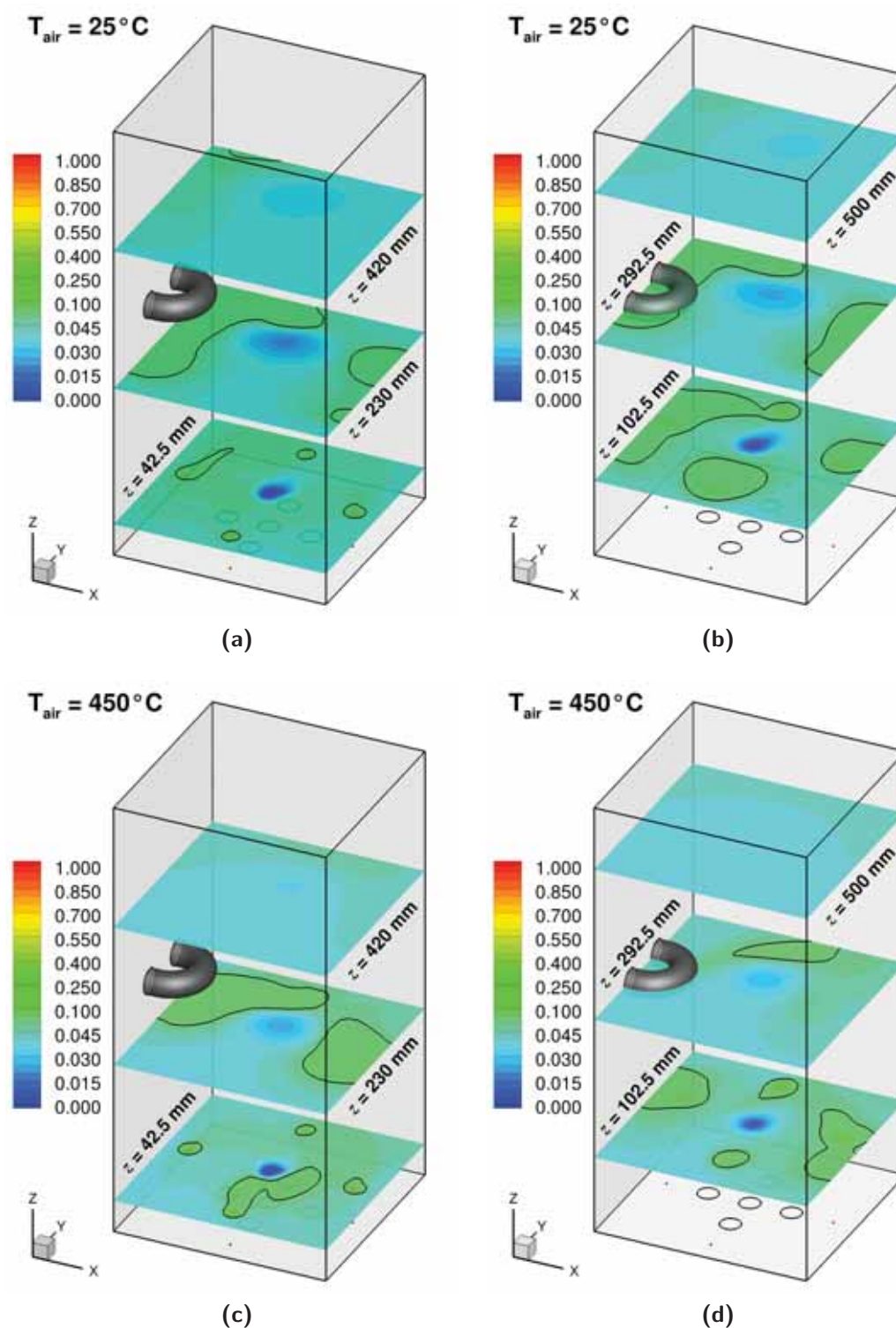**Figure 7.16:** Computed mixture fraction (ξ) contours with stoichiometric surface ($\xi_{st} = 0.0552$) overlaid for the baseline case, (a) and (b) without air preheat, $T_{air} = 25°C$, and (c) and (d) with air preheat, $T_{air} = 450°C$, for the EDC model with the Smooke mechanism at different $x - y$ planes.

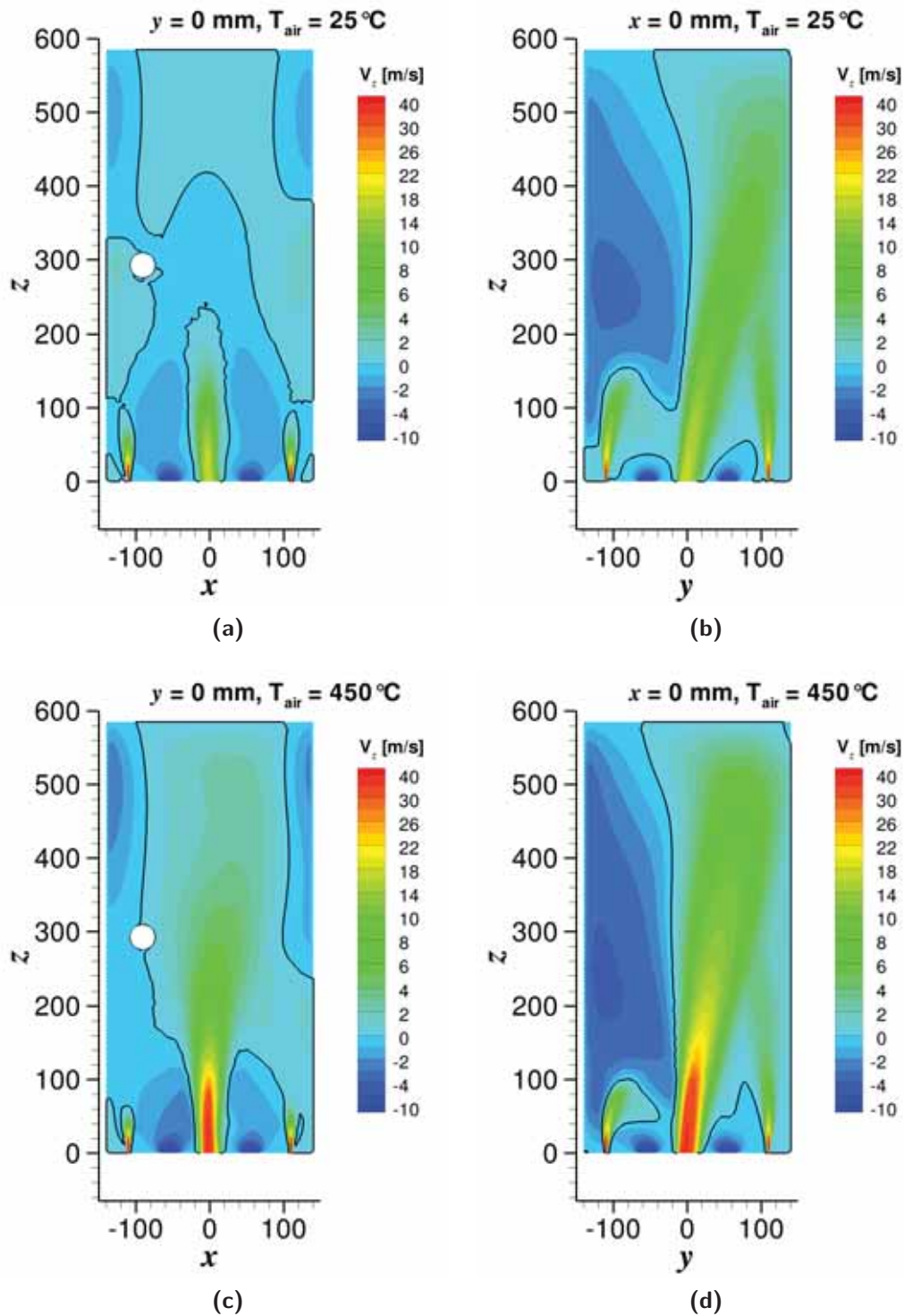**Figure 7.17:** Predicted mean axial velocity (V_z) contours for the baseline case, (a) and (b) without air preheat, $T_{air} = 25°C$, and (c) and (d) with air preheat, $T_{air} = 450°C$, for the EDC model with the Smooke mechanism at the $x - z$ and $y - z$ centreline planes. The lines represent the points in the flow field where $V_z = 0$.
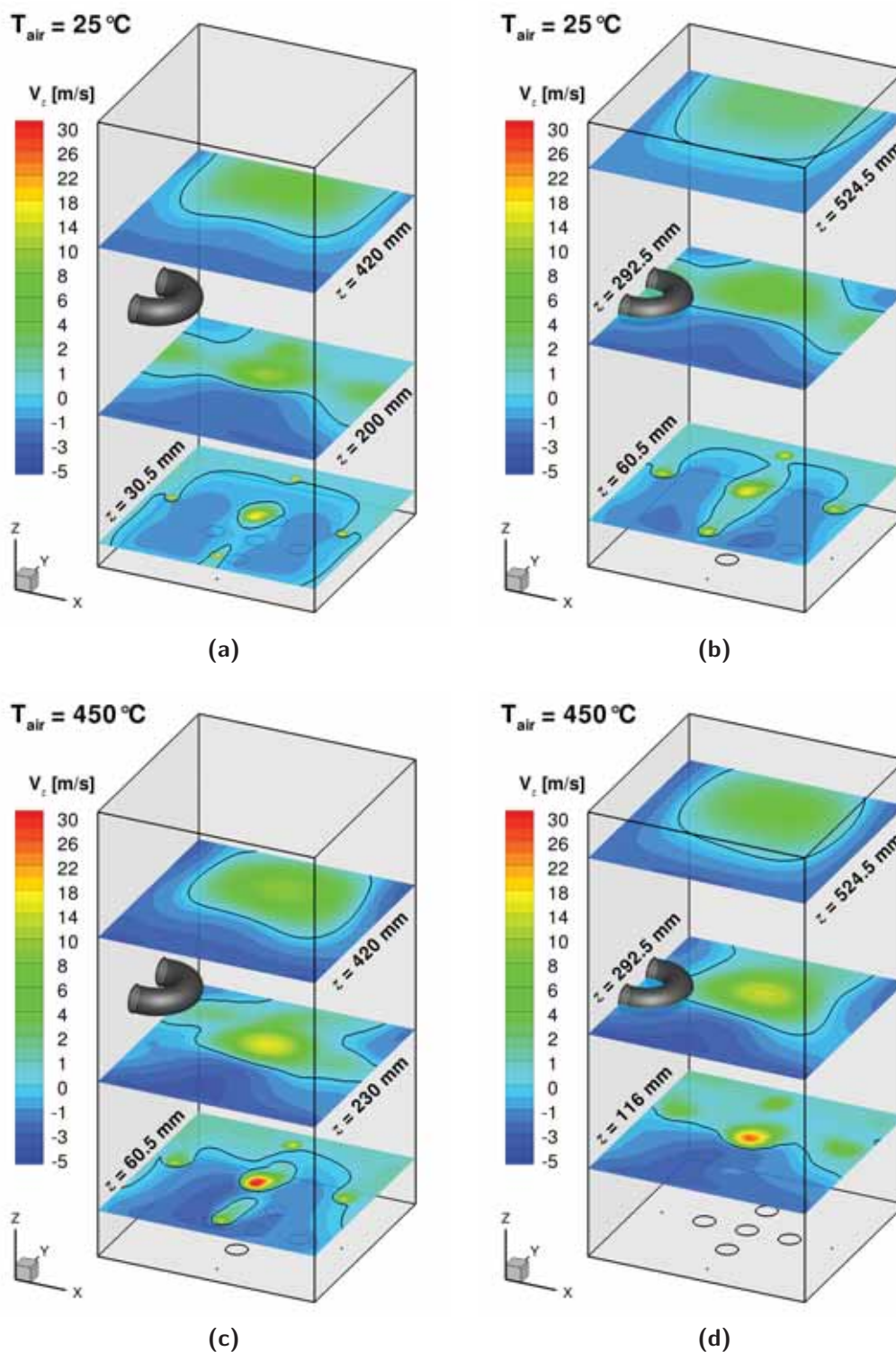
Figure 7.18: Predicted mean axial velocity (V_z) contours for the baseline case, (a) and (b) without air preheat, $T_{air} = 25°$C, and (c) and (d) with air preheat, $T_{air} = 450°$C, for the EDC model with the Smooke mechanism at different $x − y$ planes. The lines represent the points in the flow field where $V_z = 0$.

insertion length is the same, about 21% of the total thermal input is extracted for the case without air preheat, compared with about 23% for the case with air preheat (see Table 7.1).

For the conditions presented in Figures 7.19 and 7.20, the air jet momentum (G_{air}) is decreased from 0.196 N with air preheat to 0.075 N without air preheat. The 62% reduction in the jet momentum flux, which was earlier seen to modify the flow field and hence mixing patterns, does not greatly affect the temperature distribution. The maximum temperature differential is less than $150-200°$C within about two thirds of the furnace ($z \gtrsim 200$ mm) for the two cases. This high degree of uniformity observed here is an important feature of the MILD regime.

The delayed mixing between fuel and oxidant is evidenced by the thermal field. The fuel jets are entrained into the air jet roughly about halfway along the furnace for both operating conditions, except for fuel jet B. The temperature in the fuel jets gradually increases as it penetrates into the furnace due to radiation from the walls and entrainment of hot combustion products into the jet until combustion reactions can occur. Unlike in conventional flame systems, the reaction zone is distributed over a fairly large volume.

While the reaction zone for the case without air preheat extends to about $z = 420$ mm, it is confined to the bottom half of the furnace, $z \lesssim 330$ mm for the case with air preheat. The highest temperature was predicted to be around $1550°$C and $1450°$C, respectively for the case with and without air preheat, and occur relatively close to the burner exit in the reaction zone region around fuel jet B. This can be explained by the short penetration distance, which reduces entrainment of flue gases into the fuel jet prior to reaction. This observation highlights the strong coupling of the furnace aerodynamics with the reaction zone structure, and hence with stability characteristics of the burner.

The effect of heat extraction on the thermal field due to the presence of the heat exchanger through one wall is noticeable from both preheated and nonpreheated cases, parts (a) and (c) of Figure 7.19 and parts (b) and (d) of Figure 7.20. The average temperature at, or very close to, the heat exchanger surface is calculated from the CFD solution to be $\bar{T}_{hx} \approx 170°$C. The cooling effect is expected to result in local extinction and partial oxidation near to the cold surface. This particularly concerns the case without air preheat because the reaction zone formed around both fuel jets A and D encompass the heat exchanger location. However, since
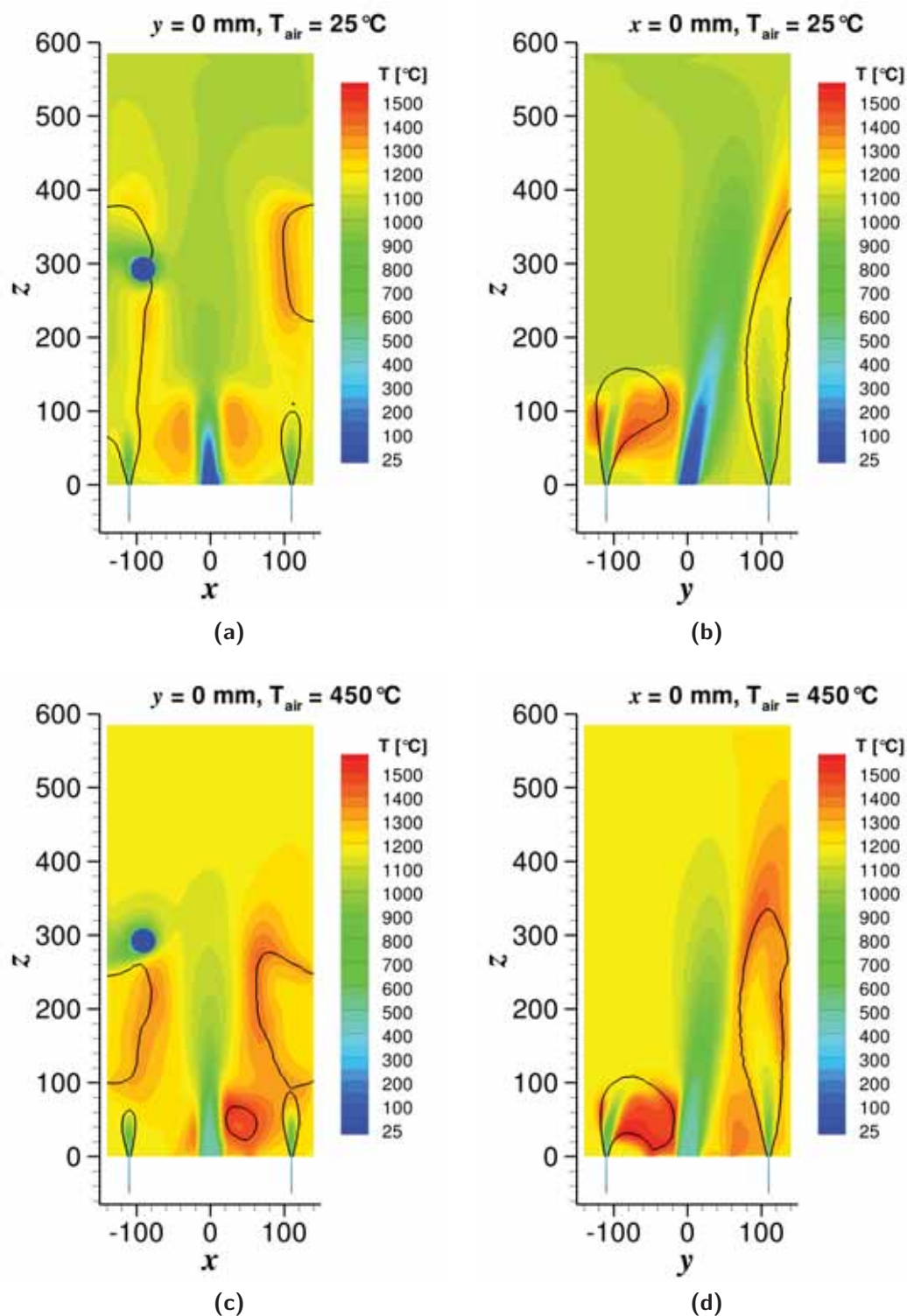
Figure 7.19: Predicted temperature contours with stoichiometric surface ($\xi_{st} = 0.0552$) overlaid for the baseline case, (a) and (b) without air preheat, $T_{air} = 25°C$, and (c) and (d) with air preheat, $T_{air} = 450°C$, for the EDC model with the Smooke mechanism at the $x - z$ and $y - z$ centreline planes.
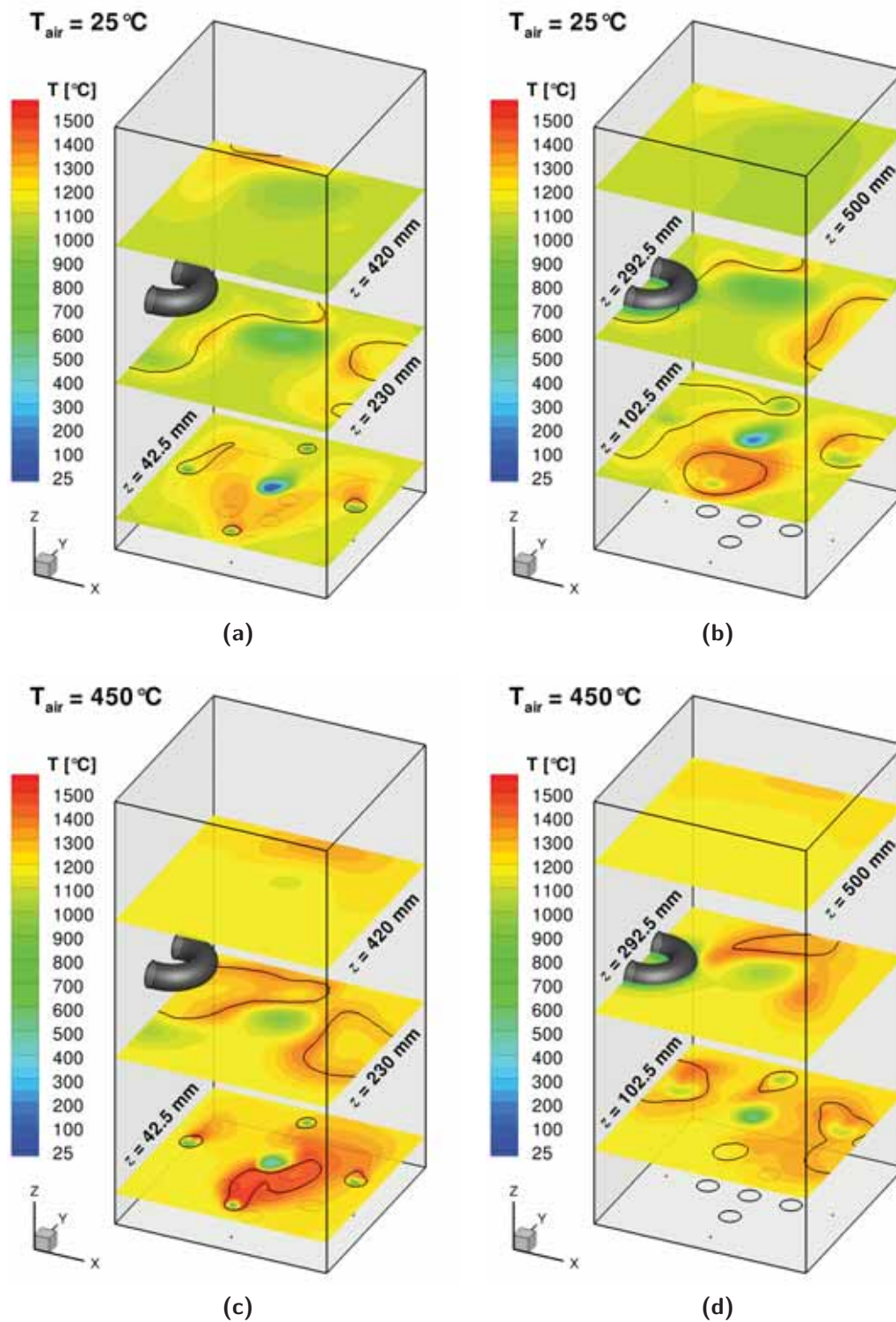
Figure 7.20: Predicted temperature contours with stoichiometric surface ($\xi_{st} = 0.0552$) overlaid for the baseline case, (a) and (b) without air preheat, $T_{air} = 25°C$, and (c) and (d) with air preheat, $T_{air} = 450°C$, for the EDC model with the Smooke mechanism at different $x - y$ planes.

the volume of the cooling loop represents less than 1% of the furnace volume, the effect is restricted to the region in the vicinity of the heat exchanger.

To emphasize the differences between the predictions of the two combustion models, temperature contours predicted using the FRED model with the two-step global reaction mechanism are shown in Figures 7.21 and 7.22. The major difference between the predictions of the EDC (Figures 7.19 and 7.20) and the FRED models are observed in the near burner region. The temperature around the fuel jets rise rapidly as soon as it enters the computational domain, generating temperatures in excess of 1750°C for the case with air preheat. This indicates early ignition, suggesting that the FRED model is not capable of capturing the diluted reactions of MILD combustion accurately. The failure to describe the delayed ignition process leads to larger penetration distances for the fuel jets and to changes in the reaction zone structure.

7.4 Investigation of Key Species

One of the main challenges involved in modelling MILD combustion is related to the turbulence-chemistry interactions. A first step in understanding the ignition and stabilisation characteristics is to investigate key species in the flow. A selection of important major and minor species relevant to methane (CH_4) combustion include O_2, CH_3, CO, CH_2O, OH, O, and H amongst others. The concentration of O_2 and CH_4 indicates the levels of dilution and fuel consumption. The methyl radical (CH_3) is one of the first steps in the destruction path of methane. Carbon monoxide (CO) is not only an important intermediate of the oxidation process, but also a hazardous air pollutant. While the formaldehyde (CH_2O) intermediate species is an ignition precursor predominant at low temperatures typically found in MILD conditions, the O, H and OH radicals are indicators of high temperature chemistry. The hydroxyl radical (OH) is used as a flame front marker. To improve readability of this section, the contour plots that characterise the compositional structure are shown in Appendix F.

Another way to visualise the penetration distance of the fuel jets is to trace the CH_4 molecules and its decomposition. The predictions of methane consumption are shown in Figures F.1 through F.4. The highest concentrations of methane

Figure 7.21: Predicted temperature contours with stoichiometric surface ($\xi_{st} = 0.0552$) overlaid for the baseline case, (a) and (b) without air preheat, $T_{air} = 25°C$, and (c) and (d) with air preheat, $T_{air} = 450°C$, for the FRED model with the two-step global reaction mechanism at the $x - z$ and $y - z$ centreline planes.
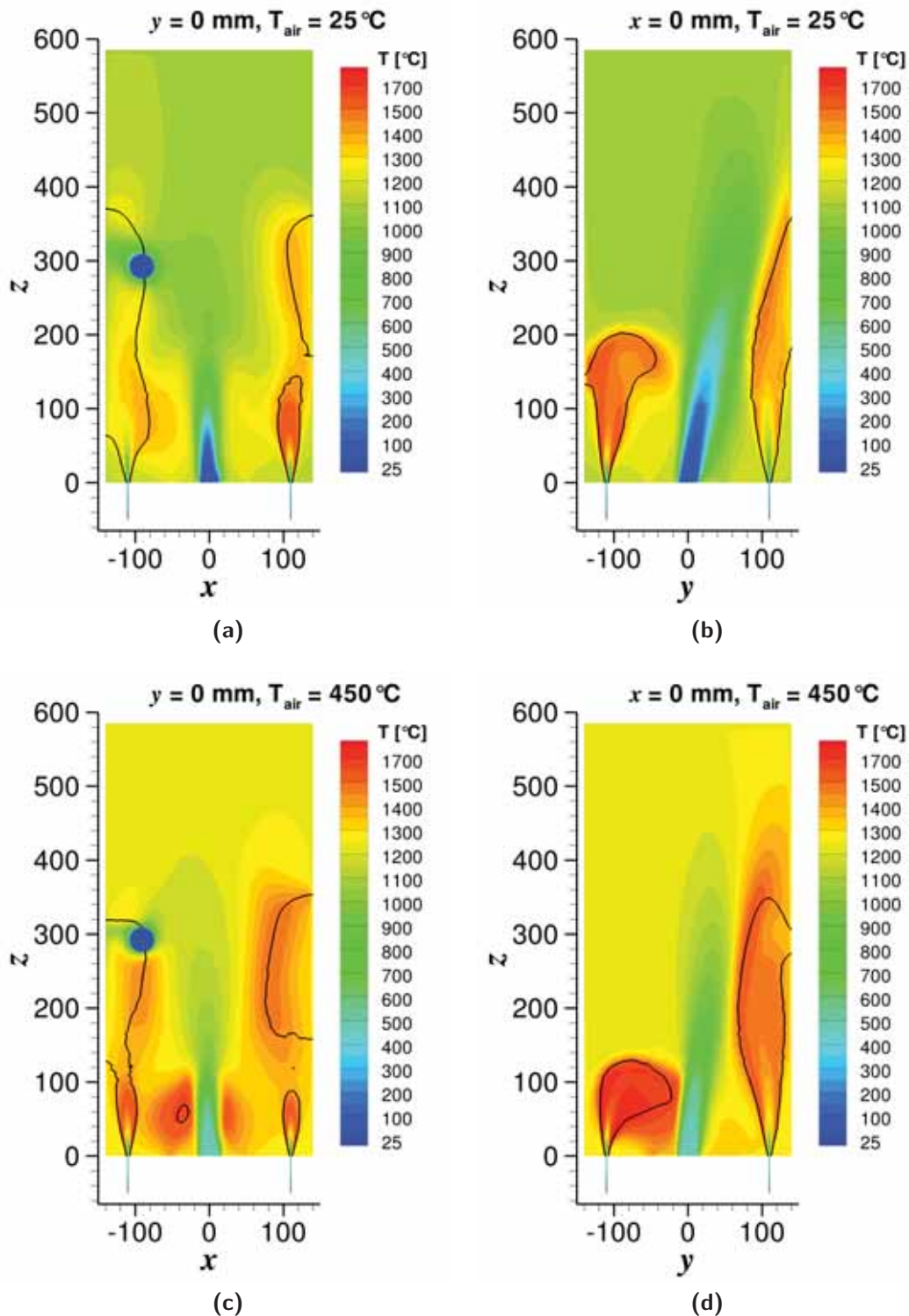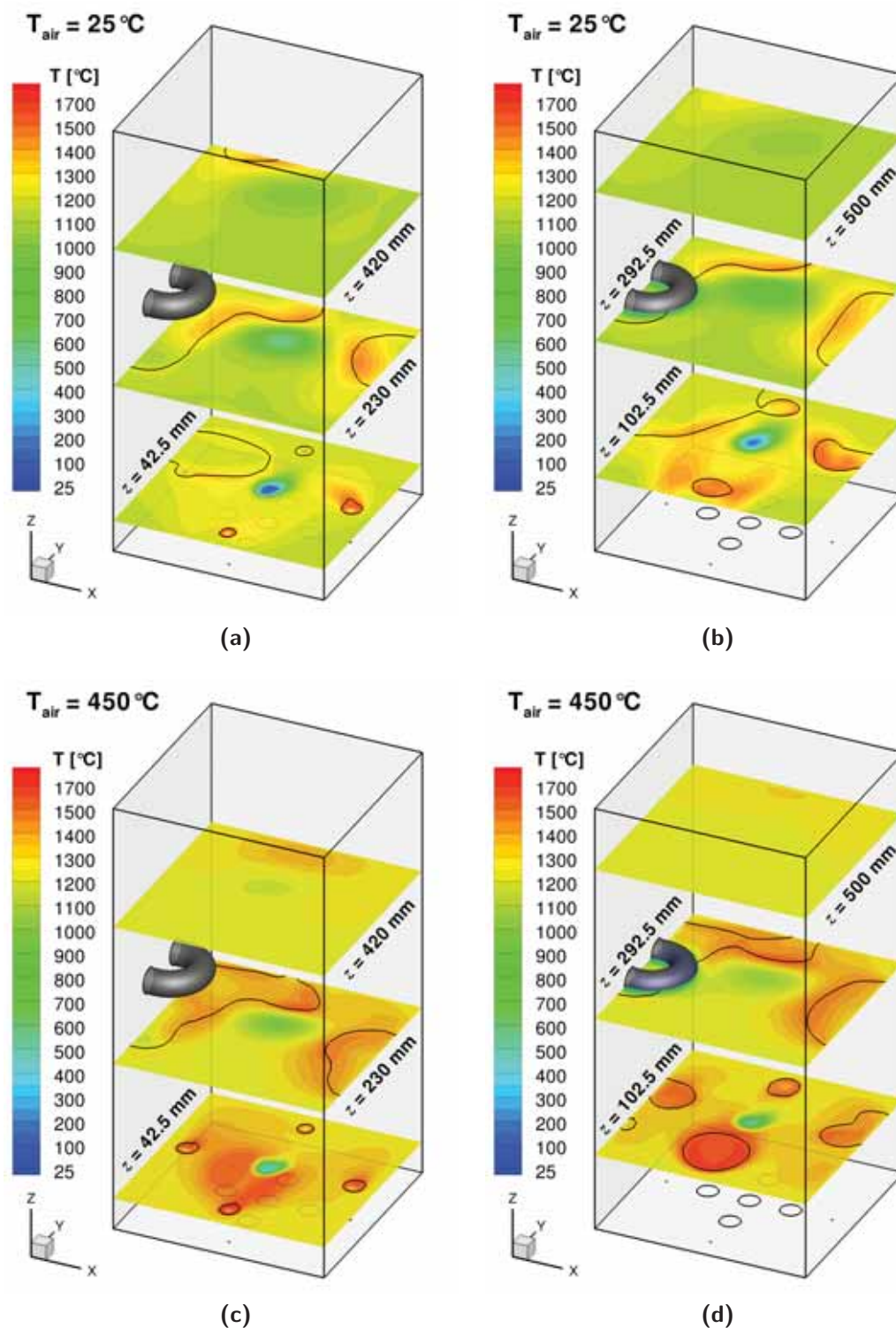
Figure 7.22: Predicted temperature contours with stoichiometric surface ($\xi_{st} = 0.0552$) overlaid for the baseline case, (a) and (b) without air preheat, $T_{air} = 25°C$, and (c) and (d) with air preheat, $T_{air} = 450°C$, for the FRED model with the two-step global reaction mechanism at different $x - y$ planes.

are observed near the burner exit plane. As the fuel streams entrain furnace gases, methane is progressively broken down to yield CH_3 radicals. Following the formation of CH_3, the diluted mixture reacts further downstream and the methane content decreases. Traces of CH_4 molecules are no longer observed at $z \approx 280$ mm and $z \approx 360$ mm, respectively for the case with and without air preheat. These downstream locations are consistent with the stability diagram presented in Figure 5.14.

The predicted contours of oxygen are shown in Figures F.5 and F.6. The high levels of dilution induced by the separation between the air and fuel nozzles is evidenced by the O_2 contours. Oxygen mole fractions of about 6% are observed at the burner nearfield ($z < 102.5$ mm). It is clear that the reactions take place in a low oxygen environment. The inherently slower reaction rates of MILD combustion caused by dilution enhance the influence of molecular diffusion effects. It has been demonstrated that differential diffusion plays an important role in the predictions of temperature and species in open flames operating in highly diluted conditions [28]. To assess its importance in the present wall-enclosed system, a molecular diffusion term was included in the calculations of the EDC model for the case with air preheat. The mass diffusion coefficients for each species were computed from a polynomial function of temperature. The results have shown that differential diffusion effects are negligible for the current system.

The formation of carbon monoxide inside the furnace is displayed in Figures F.7 and F.8. It is noted that CO forms gradually on the fuel-rich mixture, indicating that the conversion to CO_2 is slower than in conventional systems. The highest concentrations of CO are spatially located around fuel jet B for both preheated and nonpreheated conditions, which suggests that CO formation is related to the mixing patterns and local temperatures rather than the reaction quenching process caused by the heat exchanger (see thermal field in §7.3). This explains the discrepancy between the experiments and the predictions of CO emissions with the EDC model presented in Table 7.2.

The contour plots of species relevant to the ignition process, which include CH_2O, OH, O, and H, are shown in Figures F.9 through F.16. There is a significant build-up of CH_2O on the fuel-rich mixture with peak mole fraction values further downstream prior to ignition, which subsequently leads to the formation of OH on the fuel-lean mixture of the reaction zone. Formaldehyde is formed as a

product of the conversion of methane at lower temperatures [69, 129]. As the oxidation process develops the concentration of CH_2O decreases. This is consistent with the imaging measurements in the jet in hot coflow (JHC) burner reported by Medwell et al. [130, 131].

The initiation of the high temperature chemistry can be seen from the formation of O and H radicals. The concentration of these radicals tend to be higher in the case with air preheat due to the higher temperatures. This qualitative ignition behaviour with an early formation of CH_2O observed for both preheated and nonpreheated cases has been described in previous studies as an autoignition pattern under similar conditions [69, 74, 76]. The results show a pre-ignition region at the burner nearfield, where flame stabilisation depends on the levels of dilution with hot products, increasing the influence of turbulence-chemistry interactions on the flame propagation.

The concentration of the OH radical has a similar pattern to the thermal field, in the sense that the maximum values of OH correspond to the highest temperature regions on the burnt mixture. It is imperative to highlight that the OH radicals are fairly distributed inside the combustion chamber, in contrast to conventional flames, suggesting a wide volumetric reaction zone, which is an important characteristic of MILD combustion. There is little evidence of OH above $z \gtrsim 420$ mm, confirming that the flame front is forced towards the burner plane by the recirculation stream. Hence, the recirculation region formed at the top section of the furnace acts like an energy reservoir mainly containing a mixture of burnt gases.

7.5 NO$_x$ Formation

The predictions of NO$_x$ emissions have been validated against exhaust gas measurements in §7.2.4. Further assessments of the formation of NO$_x$ in this complex recirculating flow with low oxygen concentrations are presented in this section. The major NO$_x$ formation regions are identified and the relative importance of each NO formation mechanism is evaluated. The predicted NO$_x$ contour plots are shown in Appendix G.

Figures G.1 and G.2 show the predicted NO distribution inside the furnace on

a wet basis for the EDC model with the Smooke mechanism. Worth noting that a different contour scale is used for each operating condition. As expected, the NO concentrations for the baseline case with preheat are higher than for the case without air preheat. The peak NO concentrations generally occur in the highest temperature regions, but unlike in conventional diffusion flames, they are not found near the burner exit plane around the jet core. Once again, this illustrates that combustion reactions are significantly delayed by the lack of mixing of fuel and oxidant until further downstream.

It is difficult to identify the source of NO formation and/or destruction from the concentration contours, because of the balance between the convection and chemical reaction processes. Therefore, NO reaction rate contours obtained with the full NO model shown in Table 7.2 are presented in Figures G.3 through G.8 for the baseline case with and without external air preheat. The contribution of each pathway to the overall NO formation is displayed separately through the furnace centreline and at different $x - y$ planes.

In both operating conditions, NO forms in a relatively thin layer close to the reaction zone on the fuel-lean mixture. The maximum formation rates are observed at locations where dilution with combustion products was not effective, such as around fuel jet B and the elongated shear layer between fuel jet D and the air jet. Clearly, the N_2O-intermediate pathway is the dominant NO_x formation route, but the thermal-NO mechanism still contributes substantially in higher temperature regions. The prompt-NO pathway is basically negligible. This is consistent with the NO_x scaling analysis shown in Chapter 6.

These results suggest that, although NO_x emissions are at least four times lower than in the conventional regime for the present burner configuration (see §5.3), effective mixing is essential in order to increase dilution before reaction and suppress NO_x production.

7.6 Summary

In this chapter, the numerical modelling results were used to better understand the passive and reactive fields, and the parameters that influence their structure. The experimental data available for validation of the CFD model consisted of in-

furnace temperature and velocity measurements, exhaust gas emissions and an energy balance. The performance of different turbulence models were evaluated for nonreacting isothermal conditions. Two different combustion models were assessed for selected reacting cases with and without external air preheat: a finite-rate/eddy dissipation model (FRED) with a two-step global reaction and the eddy dissipation concept (EDC) with the Smooke mechanism.

The turbulence model that provided the best agreement with the LDA data for jet spread and decay rates in nonreacting conditions was the realizable $k - \epsilon$ model. Despite the complexity of this highly convoluted three-dimensional flow, the validation process showed that the essential characteristics of the diluted and distributed reactions of MILD combustion have been captured. The EDC model provided the most accurate predictions of the thermal field for both reacting conditions.

Overall, the delayed mixing between fuel and oxidant has been reasonably well captured by the CFD model. The fuel jets are entrained into the air jet roughly about halfway along the furnace for both operating conditions, with the exception of fuel jet B. The discrepancies seen in the structure of fuel jet B are likely related to the ability of the turbulence-chemistry interaction model to predict the delayed ignition. The FRED model appears to predict a larger penetration distance for the fuel jets than the EDC model.

In the early stages of the oxidation process, there is an increase in local temperature due to the entrainment of combustion products into the reactant streams. This is followed by a build-up of a radical pool of species, such as CH_2O, prior to ignition. The reduction in reaction rates at low O_2 levels and the broad distribution of OH and subsequent increases in O and H were noticeable. Unlike in conventional flame systems, the reaction zone is distributed over a fairly large volume.

It was found that the mixing patterns inside the furnace have a strong influence on the trajectory of the fuel jets, and consequently on the structure of the reaction zone. The stronger the recirculation stream, the smaller the penetration distance of the fuel jets. The short penetration distance reduces entrainment of flue gases into the fuel jet prior to reaction, leading to increased temperatures in the reaction zone and higher rates of CO and NO formation. The highest concentrations of CO were observed around fuel jet B, demonstrating that the effect of heat extraction

on CO emissions is minor and localised. It has been shown that effective mixing is essential in order to increase dilution before reaction to ensure stability of this multiple jet system. Since the incoming air stream is separated from the fuel streams by a relatively large distance, the momentum ratio between the air and fuel jets control the fuel jet penetration, and hence flame stability.

The CFD model highlights the importance of accounting for finite-rate chemistry effects to accurately predict NO_x emissions. Although both combustion models underpredicted the total NO_x emissions, the quantitative analysis of NO_x formation showed encouraging results. The discrepancies are due to differences in the predicted thermal and chemistry fields. The N_2O-intermediate mechanism was found to be the dominant NO_x formation mechanism, representing 73% and 83% of the the total NO_x emissions respectively for the baseline case with and without air preheat. The prompt-NO mechanism was found to be negligible. There was evidence of NO reburning for this furnace/burner configuration, which can be explained by the recirculating nature of the flow inside the furnace.

Chapter 8 General Discussion

The combination of numerical and experimental results from Chapters 5, 6, and 7 have revealed many interesting aspects of MILD combustion. The parallel jet burner has proven to successfully operate in the MILD regime without the need for external air preheating in a wide range of operating conditions. The NO_x scaling analysis has provided unique insight into NO_x formation and/or destruction in MILD conditions. The CFD analysis has proven to be an extremely useful tool for investigating the complex flow patterns inside the furnace, and has helped in identifying the parameter that affects the stability characteristics of this multiple jet system. The major issues brought out in this study will be discussed in separate sections throughout the remainder of this chapter.

8.1 Cooling Effects and CO Conversion

The requirement of highly preheated air, typically above 1000°C, is deemed by some to be a critical factor for the establishment and stability of MILD combustion [113, 136, 182]. As already seen from the global measurements in Figures 5.6, 5.7, and 5.10 and from the numerical model in Figures 7.19 and 7.20, external air preheating is not a necessary condition to achieve stable MILD combustion. The parallel jet burner configuration allows initial dilution with hot combustion products in the near-burner zone, compensating for the low inlet temperature of the reactants. This finding offers the potential to reduce the time and/or costs associated with start-up. It may also offer the potential to reduce the capital and maintenance costs involved with high temperature ceramic regenerators/recuperators in some applications.

Most practical combustion devices are controlled to their own optimum range of equivalence ratio (ϕ) to keep emissions to a minimum while also minimizing excess air. It is clear from Figure 5.9 that the optimal equivalence ratio needed to avoid significant CO, depends on the position of the cooling loop. The differences in the CO formation profiles indicate that this effect is complex.

One possible cause for CO emission from this furnace maybe reaction quenching due to the presence of a cold surface. However, the predicted thermal field (§7.3) indicates that the cooling effect is restricted to the region in the vicinity of the heat exchanger and does not contribute significantly to the formation of CO (Figures F.7 and F.8). Measurements of a case with and without heat extraction for the same position of the heat exchanger at higher equivalence ratios also did not support this hypothesis. Those tests revealed that CO levels either remained unchanged or even increased slightly because of the higher furnace temperatures.

The mixing patterns inside the furnace can also influence CO emissions and temperature distribution. For the data presented in Figure 5.9, there was an 18% reduction in air jet momentum from $\phi = 0.89$ to $\phi = 0.97$, while the furnace temperature increased by about $2-4\%$ resulting in a sharp rise in CO emissions for all heat exchanger positions. For the CFD data presented in Figures F.7 and F.8, and Table 7.2, the high concentrations of CO were caused by the short penetration distance of fuel jet B. Both the experimental results and the numerical calculations suggests that the increase in CO emissions is related to changes to the flow field and turbulence levels.

The results from the PSR model (Figure 5.9), which assumes perfect mixing, demonstrate that chemical kinetics does not have a controlling influence on CO emissions. This is consistent with the fact that the levels of CO emissions are significantly higher in the experiments than the equilibrium values for in-furnace conditions.

Because furnace temperatures are well below 1800°C, only negligible amounts of CO would be formed through the dissociation pathway of carbon dioxide, $CO_2 \rightarrow CO + 1/2\ O_2$.

A simple analysis of the chemical effects on the rate controlling reaction in the CO oxidation mechanism is instructive. Considering equation 2.16, $CO + OH \rightarrow CO_2 + H$, as the principal reaction of carbon monoxide oxidation, it is noted that the concentration of hydroxyl (OH) radicals controls the conversion step of CO

into CO_2. The recent measurements of Medwell et al. [130, 131] in turbulent jet flames issuing into a heated and diluted coflow show that low oxygen concentrations lead to the suppression of OH radicals as a result of reduced temperatures in the reaction zone. This suggests that the highly diluted conditions of the MILD regime are more prone to CO emissions than are conventional flames. This is consistent with the high levels of excess air required to keep combustion below the CO threshold, as previously reported in §5.4.7. Since the OH radicals are much more uniformly distributed inside the furnace than in a conventional flame (Figures F.11 and F.12), their local concentration is also much lower. This means that effective mixing is required to increase the probability of reactions going to completion.

8.2 Furnace Aerodynamics and Stability Criterion

The detailed analysis of the flow field presented earlier in §7.3 revealed that there is a significant influence of the furnace aerodynamics on the fuel jet trajectory. However, it is difficult to identify the key flow patterns from the complex three-dimensional representation. Figure 8.1 shows a simplified, axisymmetric representation of the flow field inside the furnace. This two-dimensional representation was obtained by combining the experimental data and the modelling calculations. It seeks to further examine the effect of mixing on the stability of the MILD regime. The trajectories of the fuel jets, central air jet and the recirculation stream are shown beside the measured thermal field of Figure 7.10 with the velocity contours from Figure 7.17 overlaid. The temperature contour was generated using a Kriging-type interpolation algorithm [41] from the original measurement grid, which consisted of 3×4×6 points in each Cartesian direction. Since the temperature data contain measurements near to the fuel injection location, it provides insight into the structure of the reaction zone for the baseline case.

This diagram identifies three distinct regions: (1) burner nearfield, (2) mixing zone, and (3) recirculation zone. In this parallel jet burner arrangement, the reactants and exhaust ports are mounted on the same wall, and the incoming air stream is separated from the fuel streams by a relatively large distance ($d_{fa} = 110$
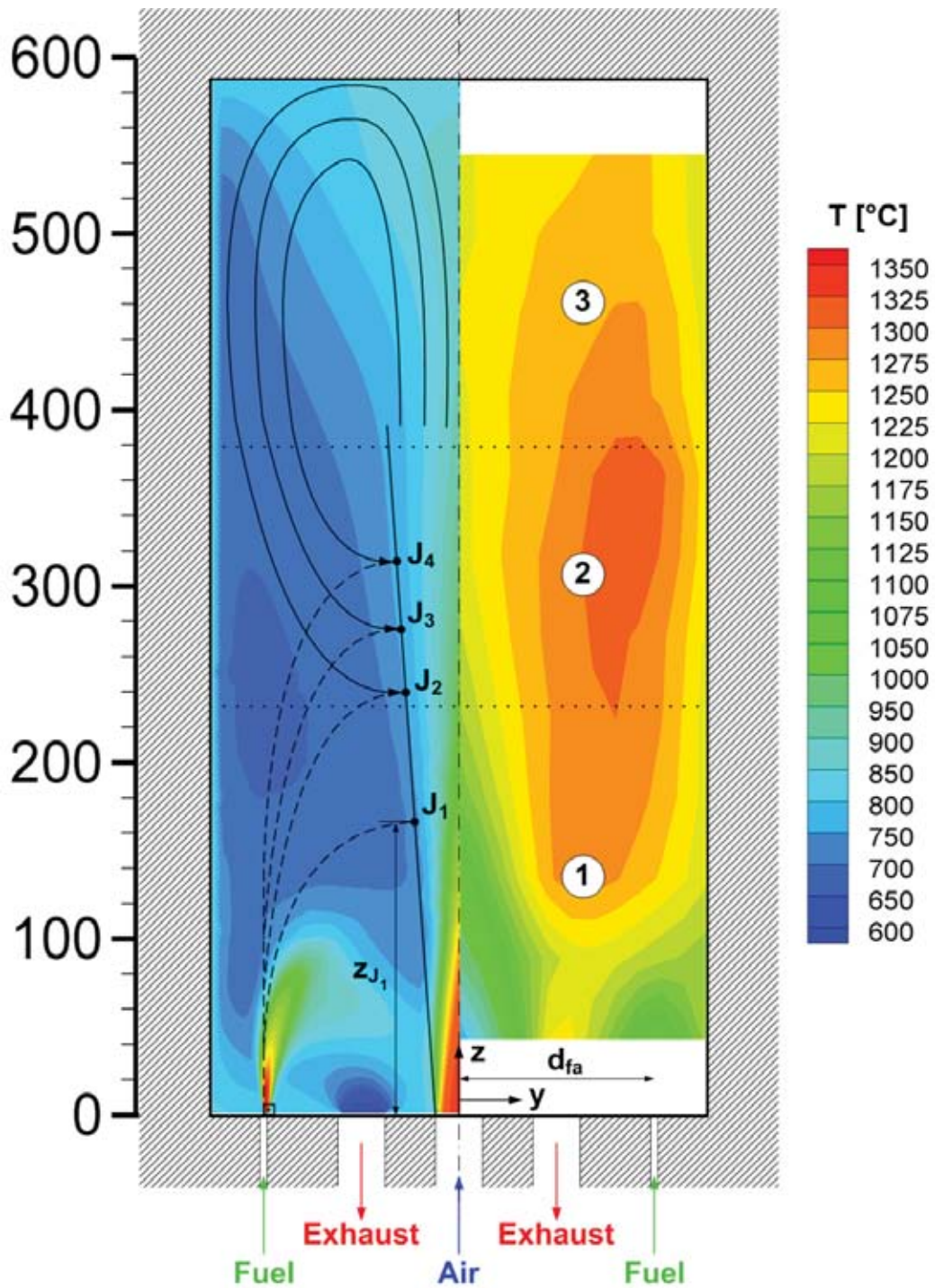
Figure 8.1: Simplified axisymmetric representation of the aerodynamics inside the combustion chamber with the velocity contours from Figure 7.17 overlaid, derived from §7.3, beside the measured temperature distribution from Figure 7.10.

mm), much like in the IFRF burner arrangement [194]. This implies that in Region 1, the air and the fuel jets entrain furnace gases before interacting with each other. The delayed mixing is evidenced by the thermal field and the build-up of CH_2O in a pre-ignition stage (Figures F.9 and F.10). Region 1 has also been denoted by Grandmaison et al. [79] as "pre-encounter" zone in the strong-jet/weak-jet (SJWJ) model, and more recently by Mancini et al. [122] as a "preconditioning" zone.

The central air jet has momentum flux (G_{air}) of $50-200$ times higher than the fuel jet momentum (G_{fuel}). Hence it behaves as a weakly confined jet. However, the fuel jets exhibit curved trajectories (dashed lines) as they are entrained into the central jet, which has a much higher momentum. The fuel and the recirculating products' streams merge at a location defined by the intersection of the fuel jet trajectory and the mean boundary of the air jet, $J_2 - J_4$ in Figure 8.1. This then defines the lower boundary of Region 2, where the diluted reactants mix and heat release occurs. The high temperatures and the formation of O and H radicals (Figures F.11 through F.16) found in this region support this deduction.

Region 3 is defined as the recirculation zone. The basic feature of this zone is the change in the flow direction. The air jet expands through the furnace and constantly induces recirculation due to interaction with the walls. This recirculating flow structure mainly contains a mixture of hot combustion products (e.g. CO_2, H_2O, N_2), which ensures high dilution rates and temperatures above autoignition for the establishment of the MILD regime. Although some reactive species are still present in Region 3, because of the relatively slow reactions caused by low oxygen concentrations and moderate temperature levels typical of MILD conditions, the temperature distribution is quite uniform and there are virtually no reactions taking place (Figures 7.19 and 7.20).

The existence of an unstable MILD regime has alternatively been attributed to heat losses and fuel inlet jet velocities in gas turbine systems [153, 188], and to low internal exhaust gas recirculation rates in furnaces [199]. However, Figure 5.14 from §5.5.2 clearly shows that fuel jet momentum controls the stability of this system. This is consistent with both the aerodynamic analysis shown above and the visual observations presented earlier in §5.5.1. A lower fuel jet momentum will lead to a change in the jet trajectory, and hence to a decrease in the penetration distance or junction point, z_J (Figure 8.1). This reduces the amount of dilution

with hot combustion products prior to mixing with the oxidant stream. Hence it controls the local species concentrations and temperatures in the reaction zone, and thus CO oxidation (Figures F.7 and F.8) and NO_x formation (§7.5). This deduction is strongly supported by the LDA data and CFD results obtained around fuel jet B, which were represented in Figure 8.1.

The measurements of Dally et al. [38, 39] extended by Medwell et al. [130, 131] in open jet flames issuing into a heated and diluted coflow give further evidence of the influence of local species concentrations. They found that reducing the oxygen levels in the coflow, which is analogous to increasing the amount of dilution or jet penetration distance in furnace conditions, leads to less luminous flames and reduced temperatures in the reaction zone. In recent studies, Domingo et al. [49] and Gordon [73] analyzed autoignition and partially premixed flame propagation of a lifted methane jet flame in a vitiated coflow. Their results similarly highlighted the influence of dilution levels on the stabilization and development of the reaction zone.

Importantly, the present data show that the K_V stability criterion defined by Wünning and Wünning [199] only holds for a fixed furnace/burner arrangement. That is, the critical values of K_V depend on the burner diameter here, and hence on the momentum ratio. This implies that, to estimate these values, a priori knowledge of the flow field is required, either through experiments or numerical modeling, along with other assumptions [25]. However, as previously discussed in 7.2.1, the mass flow rate of recirculating combustion products is often difficult to accurately determine in complex combustion chambers. On the other hand, jet momentum is a straightforward global parameter to determine, and can be used to characterize these processes for a given geometric configuration.

Although the particular stability threshold of $G_{fuel}/G_{air} \approx 0.006$ is unlikely to be universal, the role of jet momentum in characterising the stability criterion can be extended to other MILD combustion systems. Because MILD burners operate with flame stabilisation by burned gases, the same three regions described in Figure 8.1 are expected to occur irrespective of the furnace/burner arrangement. Evidently the boundaries of the main three zones will be modified, and also affected by heat extraction and air preheat temperature, as seen in Figures 7.19 and 7.20. To test this hypothesis, the burner configuration has been switched in the MCF, so that air is injected from the $\varnothing_{id} = 3$ mm outer jets and fuel from a

$\varnothing_{id} = 4.6$ mm central nozzle. A momentum threshold for stable MILD operation of $G_{fuel} \approx 0.004$ N, which corresponds to $G_{fuel}/G_{air} \approx 0.03$ and $z_J \approx 430$ mm was obtained for the baseline conditions without external air preheat. The preliminary results for the new burner configuration have encouraged further investigation of the performance and stability limits using biomass fuels [166].

8.3 NO$_x$ Formation / Destruction and Scaling

The Zel'dovich thermal mechanism is usually the major contributor to NO$_x$ formation in most high temperature ($T > 1500°$C) combustion systems. As already seen in Figures 6.1, 7.9 and 7.10, the temperatures in the present furnace are considerably lower than this ($T < 1360°$C) and its distribution is quite uniform. Because of the low fluctuations of MILD combustion [143], it is unlikely that instantaneous temperatures will significantly exceed the measured mean values. Hence, consistent with the well-established understanding of the operation of MILD combustion systems, NO$_x$ formation via the thermal-NO mechanism is inhibited relative to conventional combustion [199]. Thermal NO$_x$ is not only suppressed, but also does not control NO$_x$ emissions, as was previously noted in Figure 6.6. The results presented in Figure 6.2 and Table 7.2 reinforces the fact that the thermal-NO route is not dominant. Therefore, Fenimore's prompt-NO and/or N$_2$O-intermediate mechanisms are also expected to be important.

The fuel dilution results from Figure 5.8 suggest that NO$_x$ formation may be dependent on the ratio of carbon to hydrogen atoms (C/H) in the fuel molecule. Since the temperatures are so similar for the dilution cases, the difference cannot be attributed to the thermal-NO route. Rather, the fuel type dependence is further evidence that the prompt-NO mechanism might be significant. The dependence on fuel type has also been observed in Figure 6.4. The relevance of the prompt-NO pathway in the MILD regime has been speculated by a few researchers [65, 98, 123, 171, 194]. In the predictions of Mancini et al. [123], only 5% of global NO$_x$ emissions were calculated to be of prompt-NO origin.

On the other hand, it has been observed that the N$_2$O-intermediate mechanism can represent up to 65% of the total NO$_x$ formation in lean-premixed methane combustion in a jet-stirred reactor at atmospheric pressure in a temperature

range from 1140 to 1570°C [173]. Very few studies have considered the role of the N_2O-intermediate mechanism in NO_x formation in MILD combustion systems [180, 201].

The quantitative analysis of NO_x emissions discussed in §7.5 provides original insight into NO_x formation in MILD combustion systems. It is clear from those calculations that NO_x formation via the prompt-NO mechanism is negligible, and that the thermal-NO pathway is not dominant. The contribution of the N_2O-intermediate pathway to the overall NO_x emissions are as high as 83%.

There was evidence of NO reburning for this parallel jet burner configuration. According to the numerical predictions, the potential for reduction via the reburn destruction route is calculated to be 14% and 28%, respectively for the baseline case with and without air preheat. Further investigation of the NO-reburning mechanism is beyond the scope of this thesis.

Several parameters seem to alter NO_x formation in MILD combustion conditions and hence add to the complexity of the scaling problem. Chapter 6 have outlined the influence of heat extraction, air preheat, oxygen concentration, dilution and fuel type on global NO_x emissions. While all these parameters are not independent from each other, the combined effect can be ultimately associated with a characteristic non-adiabatic temperature and residence time, as shown in Figure 6.6. However, the fairly poor fit found in the regression analysis presented in Figure 6.7, demonstrates that temperature and residence time influence, but do not control, the scaling of NO_x. It is not possible to isolate one or two controlling parameters, because many parameters seem to have an influence of comparable magnitude.

Although the Froude number has been used as a scaling parameter in furnace conditions with conventional flames [191], Figure 6.4 suggests that it is not the most relevant parameter to scale NO_x emissions from furnaces operating in the MILD regime. This is because buoyancy forces are particularly weak in an environment with low temperature gradients. Nevertheless, some dependence on Fr_e is evident, which implies that fuel jet momentum is still an important parameter. The data for the two different burner sizes shown in Figure 5.8 give further evidence of the influence of momentum. A lower fuel jet momentum leads to a change in the jet trajectory, much like in the strong-jet/weak-jet model of Grandmaison et al. [79], and hence reduce the amount of dilution with hot

combustion products prior to mixing with the oxidant stream. This behaviour has been observed in §7.3 and is well illustrated in the previous section. These changes affect local species concentrations and temperatures in the reaction zone, altering the ratio between mixing and reaction times, i.e., the local Damköhler number ($Da = \tau_{mix}/\tau_{chem}$). A low local Damköhler number can favour nonequilibrium effects, such as superequilibrium O atoms [51]. Both entrainment levels of hot combustion products and nonequilibrium chemistry may account for the differences between CO_2 and N_2 dilution. However, the results from Figure 6.5 demonstrate that, although mixing has some influence, it does not control global NO_x yields. Therefore other effects, such as chemical kinetics, also influence the NO_x formation in this furnace.

The PSR calculations from Figure 5.8 indicate that the assumption of a well-stirred reactor ($Da \ll 1$) used by some researchers [42, 45] does not appear to be reasonable in the present MCF system. This is consistent with the recent modelling study of Mancini et al. [122]. They also found that the combustion chamber cannot be simply considered as a well-stirred reactor. They proposed a reactor network model, which consisted of 22 PSRs, to predict NO_x emissions from a semi-industrial scale furnace. Their results emphasized the importance of the mixing characteristics close to the burner exit. This implies that the NO_x formation process is not controlled by chemical kinetics.

In summary, the NO_x scaling analysis described above highlights the fact that neither momentum nor kinetics has a controlling influence on NO_x emissions, but that rather both are important. This suggests that NO_x formation in the present furnace may be within the regime where mixing time scales are comparable to chemical time scales, and hence Damköhler numbers are of the order of unity, $Da = O(1)$. Therefore, in order to accurately predict NO_x emissions from MILD combustion systems, any model will need to include the effects of both mixing and chemistry.

8.4 Application / Implementation

Commercial application of the MILD combustion technology has been "traditionally" limited to heat treatment processes, such as annealing and hot forging [133].

The relatively low modulation ratio and dependence on high levels of air preheating ($>1000°C$) has hindered the widespread implementation of MILD burners in other energy conversion devices to a large extent.

The current research have demonstrated that stable MILD combustion can be sustained for various thermal input, heat extraction and air preheating conditions. An important outcome of the performance tests (§5.4) was the fact that the MILD regime was reliably established without external air preheat, maintaining low NO_x emissions under no penalty of increased CO emissions. The fuel dilution results showed that even low calorific value (CV) gaseous fuels, such as biogas or landfill and digester gases, can be used. The analysis of the furnace aerodynamics revealed that there is strong coupling between the flow patterns and reaction zone structure. This shows that effective mixing is essential to increase dilution before reaction in order to ensure flame stability. Since the incoming air jet is separated from the fuel jets by a relatively large distance, it was found that the momentum ratio between the air and fuel jets controls the stability of this multiple jet system.

The implication of these findings is that by carefully controlling jet momentum, the temperature, composition of the reactants, and ignition delay can be tailored, so that heat release matches the requirements of a particular application. Hence MILD burners offer great potential not only for retrofitting old combustion systems, but also as a short-term solution for increasing the efficiency of new heat and power systems, resulting in fuel savings and decreased emissions of pollutants and greenhouse gases.

MILD burners are particularly attractive in systems that require heat recovery and/or use flue gas recirculation. Cogeneration or combined heat and power (CHP) plants that use stationary gas turbines as prime movers is an example. The most basic cogeneration system uses the gas turbine to generate electricity and the exhaust gases to produce steam in a water-tube boiler called heat recovery steam generator (HRSG). The HRSG system is usually equipped with duct burners that use external combustion air for supplementary firing to produce the total steam required by the process. The gas turbine exhaust gas contains O_2 concentrations typically lower than 15% at temperatures around $500-600°C$, depending on the thermal load [13]. The strongly depleted O_2 concentrations present combustion stability problems for conventional burners. Because of the low oxygen environment and a temperature range around autoignition levels,

MILD burners could be an interesting alternative to traditional duct burners.

The results of a techno-economic analysis showed that MILD type burners could be employed for substantially reducing NO_x emissions in open cycle gas turbine power plants with minimal increases in the investment and electricity selling price, when compared to conventional low NO_x burners [190]. MILD conditions can potentially be satisfied in recuperated gas turbines, such as Solar's Mercury™ 50 [181], that recover some of the exhaust heat otherwise lost to the ambient to preheat the air. Since the MILD regime operates with dilution rates well beyond the critical limits for conventional flame stabilisation, combustors with high levels of internal recirculation may improve efficiencies even further in a recuperated cycle gas turbine. A research and development programme funded by the European Commission to investigate the use MILD combustion under gas turbine conditions is in progress [60].

Another potential application for the MILD combustion technology are industrial boilers. A possible problem for the development of MILD burners for boilers is the typical temperature level for air preheat, which is around 200°C [102]. However, as previously demonstrated in §8.1 stable MILD combustion can be established without the need for external air preheating. The structure of a boiler consists of a radiative and a convective section. The latter usually being much larger than the former. The volumetric characteristics of MILD combustion with lower peak temperatures enhance the radiative heat flux, thereby allowing a more compact boiler design with a reduced convective section. Although the location of the heat exchanger proved to have little effect on global temperature and NO_x emissions (refer to §5.4) for this laboratory-scale furnace, reaction quenching due to the presence of a cold surface needs to be carefully considered in industrial scale boilers.

Chapter 9 Conclusions and Recommendations

This thesis undertook to advance the understanding of the MILD combustion regime through a numerical and experimental investigation of a parallel jet MILD combustion burner system in a laboratory-scale furnace burning gaseous fuels. The key findings from this investigation are outlined hereafter.

1. The performance results proved that the present furnace/burner configuration can operate with a high degree of temperature uniformity without the need for external air preheating. Overall NO_x emission values as low as 5 ppmv dry at 3% O_2 and as high as 66 ppmv dry at 3% O_2 were recorded in the MILD regime for furnace temperatures of up to 1370°C, while CO levels were kept below 100 ppm for operating conditions with excess air levels higher than 10% ($\phi \leq 0.90$).

2. In stark contrast to conventional flames, a strong decrease in NO_x emissions with flue O_2 levels did not lead to a significant increase in CO emissions. Although the presence of a water-cooled heat exchanger caused temperature differentials across the furnace, the increase in CO emissions is related to the mixing patterns rather than the quenching by the cold surface. The discrepancies found in the predictions of CO emissions from a PSR model, the significant departure from equilibrium chemistry, and the CO concentration plots from the CFD data support this deduction.

3. Despite the complexity of the recirculating flow inside the furnace, the CFD model agrees reasonably well with the experimental data. The main

discrepancies were observed in the prediction of the structure of fuel jet B, which are likely related to the ability of the turbulence-chemistry interaction model to predict the delayed ignition. Therefore, it is deduced that finite-rate chemistry must be included for more accurate predictions of the diluted and distributed conditions of MILD combustion.

4. It was found that the mixing patterns inside the furnace have a strong influence on the trajectory of the fuel jets, and consequently on the structure of the reaction zone. The analysis of the furnace aerodynamics and qualitative observations of the burner exit region have shown that effective mixing is essential in order to increase dilution before reaction to ensure stability of this multiple jet system. Since the incoming air stream is separated from the fuel streams by a relatively large distance, the momentum ratio between the air and fuel jets, G_{fuel}/G_{air}, control the fuel jet penetration, and hence flame stability. This finding is not explained by previous stability criteria, such as the Wünning and Wünning [199] recirculation rate parameter, K_V. While the actual value of the threshold for the present investigation is likely to depend on the particular geometric configuration, it is expected that the jet momentum ratio will be useful in characterizing the stability of many other MILD combustion systems.

5. It was found that, although heat extraction, air preheat, excess air, firing rate, dilution, and fuel type all influence NO_x emissions, they do not control NO_x scaling. Neither mixing nor chemistry effects were found to be dominant, suggesting that the characteristic Damköhler number spans, or is on the order of, unity. The failure of PSR and CFD calculations to predict the NO_x emissions further supports this hypothesis, as does the finding that the Froude number scaling revealed a limited dependence of NO_x emissions on jet momentum. A global NO_x production rate, calculated based on a global residence time and a characteristic furnace temperature, was found to give the best scaling of the data across all conditions assessed. However, the dependence on temperature was found to be much weaker than that expected based on the thermal-NO mechanism alone. This trend also applied to other MILD combustion systems, irrespective of the furnace/burner geometry. Furthermore, the regression analysis found that neither temper-

ature nor global residence time provides a sufficiently strong correlation to be considered dominant. The leading-order approach showed that, although the jet exit Froude number has been used in the past for enclosed conventional flames, it is not the appropriate parameter for NO_x scaling in the MILD regime. This is consistent with the weak role of buoyancy in a furnace with such low temperature gradients.

6. The nondominant role of the Zel'dovich thermal-NO mechanism, which is consistent with the moderate furnace temperatures ($800-1400°C$) was demonstrated. In the present MILD combustion conditions, the N_2O-intermediate mechanism was found to be the dominant NO_x formation mechanism, representing up to 83% of the the total NO_x emissions. The prompt-NO mechanism was found to be negligible and there was evidence of NO reburning for this furnace/burner configuration.

In summary, the fundamental aspects revealed by this study provide significant advancements in the understanding of MILD combustion that will assist in the effort to extend this technology to other heat and power systems.

Future work

Significant progress towards the fundamental understanding of MILD combustion have been revealed by the current research. As always, some issues remain and either warrant future investigation or further improvement. The following recommendations are made to advance this field beyond this thesis:

1. In-furnace sampling data of species concentrations would improve the database for the validation of the CFD results, and probably shed more light on the oxidation process.

2. Simultaneous imaging of temperature and key species, such as the hydroxyl radical (OH) and formaldehyde (CH_2O), like that of Medwell [129] would provide valuable information on the structure of the reaction zone at highly diluted furnace conditions. It is worth mentioning that this MILD combustion furnace has already been designed to allow advanced laser diagnostic techniques.

3. More measurements around the heat exchanger would be required to fully resolve the effects of quenching on the propagation of MILD combustion.

4. A counter-flow burner arrangement in which the air and fuel jets are positioned in opposite sides of the furnace could be used to further test the stability criterion.

5. A further study that would be of great interest for the design of industrial scale MILD combustion systems is to establish guidelines for scaling up the burners. An initial attempt to provide this kind of information has been reported by Kumar et al. [106].

6. The CFD model could be further simplified by also ensuring an axisymmetric air inlet profile and symmetry of the heat exchanger along the $y-$axis. This could be accomplished either by modifying the design of the cooling loop, or inserting an identical heat exchanger through the opposite wall. The position of the retractable bluff-body and possibly the air piping system would also need to be altered. Velocity measurements on a simple model of the burner block would be required to better characterise the air inlet boundary conditions and further improve the quality of the CFD results. Although computationally expensive, the more sophisticated transport PDF approach could be used to better understand the finite rate chemistry effects. The use of other chemical kinetic mechanism with the EDC model, such as the ARM mechanism [177], would be of significant interest to improve the combustion model validation and better understand the turbulence-chemistry interactions. Additionally, the predictions of NO_x emissions could be further analysed, since nitrogen-containing species are included in the mechanism, and are not calculated from the thermal and flow field in a post-processing step. Further investigation of the importance of the NO-reburning mechanism in conditions relevant to MILD combustion would be desirable.